ON EXTRACTING HADRON MULTIPLICITIES AND UNPOLARIZED NUCLEON STRUCTURE RATIOS FROM SIDIS DATA AT THE HERMES EXPERIMENT

BY

LOREN ALEXANDER LINDEN-LEVY

B.S., Oregon State University, 2001
M.S., University of Illinois at Urbana-Champaign, 2002

DISSERTATION

Submitted in partial fulfillment of the requirements
for the degree of Doctor of Philosophy in Physics
in the Graduate College of the
University of Illinois at Urbana-Champaign, 2008

Urbana, Illinois

Doctoral Commitee:

Professor Jen-Chieh Peng, Chair
Professor Naomi C.R. Makins
Professor Scott S. Willenbrock
Professor Russell W. Giannetta

Abstract

We present an analysis using the world's largest data set of semi-inclusive deep inelastic scattering (SIDIS) in the kinematic range $0.1 < x < 0.6$ at an average Q^2 of 2.5GeV^2. This data was collected at the HERMES experiment located in the east hall of the HERA accelerator between the years 2000 and 2006. The hadron multiplicity from these scattering events is extracted for identified charged pions, kaons and protons from two different gaseous targets (H & D). For the hydrogen (deuterium) target 12.5 (16.68) million events were recorded. Using these hadron multiplicities an attempt is made to extract unpolarized information about the parton momentum distribution functions (PDFs) inside the nucleon via the flavor tagging technique within the quark-parton model. In particular, one can exploit certain factorization assumptions and fragmentation symmetries to extract the valence quark ratio d_v/u_v and the light sea asymmetry $\bar{d} - \bar{u}/(u - d)$ from the measured pion multiplicities on hydrogen and deuterium targets. The excellent particle identification available in the HERMES spectrometer coupled with the overwhelming statistics that are available from the high density end-of-fill running (especially in 2002 and 2004) make the HERMES data invaluable for reinforcing the E866/NuSea Drell-Yan result on $\bar{d}/\bar{u}$ at a different $\langle Q^2 \rangle$ and from an entirely different physical process. These PDF extractions are also an important test of many typical assumptions made in SIDIS analyses and must be taken into consideration in light of the future facilities that propose to use this technique.

To Grandpa Ed

Acknowledgments

First and foremost I would like to thank my dearest and closest friend Erin. Without your steadfast piloting of the ship and your endless understanding none of this would have ever been possible. I am extremely lucky that I have so many additional people to thank for the help I have received throughout my graduate school experience, however, the finite space available here only allows me to point out certain specific persons. In general, I would like to thank all past and present HERMES members with whom I have had the privilege of interacting with and from whom I have learned, whether those interactions and lessons revolved around physics or life. I have grown emotionally as well as intellectually and I owe much of that growth to you. In particular I would like to thank Naomi Makins for teaching me how to put all of myself into my work and for always listening to even the craziest of my ideas, again whether those were concerning physics or life. I would also like to thank Marc Beckmann for helping me trust the quality of my own work. My colleague and close friend Joshua Rubin, whose levity and ability to think about problems from a very different perspective were invaluable assets to my own learning and sanity. During the cross check of this analysis Achim Hillebrand and I spent many days and nights searching for the differences in our results. This exercise contributed greatly to my understanding of the experimental apparatus and initiated many interesting discussions about the physics we were measuring. Last but certainly not least I would like to thank my parents Max and Tina Linden Levy for instilling in me an unbridled curiosity about the world and the courage and enthusiasm to tackle difficult problems.

Table of Contents

List of Tables

List of Figures

Chapter 1

Introduction

> *"To see a world in a grain of sand and heaven in a wild flower, hold infinity in the palm of your hand and eternity in an hour."* —William Blake

The previous passage, while beautiful in prose, also seems to imply that the natural world in which we live is much more complicated than it appears on the surface. The idea that a grain of sand represents an entire world is an (not so subtle) allusion to the inherent complexity of matter's substructure. Perhaps it was even the tiny grains of sand on a beach in Greece that led the early philosophers to think about the divisibility of the natural world. In the fifth century B.C. Democritus (while studying for his doctorate no doubt) and his teacher Leucippus proposed that matter was made up of indivisible "invisible units" called atoms [10]. While this is the most commonly referenced emergence of the atom concept it is not the earliest. The Nyaya and Vaisheshika schools in ancient India had developed elaborate theories of how atoms combine into more complex objects at least 150 years earlier [11]. These early incarnations of the atom were mainly philosophical ideas; in the modern era we have pushed these philosophical ideas into the realm of physical measurements of the truly indivisible structures in nature.

Our modern story begins thousands of years later, in 1869 (perhaps an arbitrary starting point), with the organization of the elements into a periodic chart by Mendeleev [12]. The presentation of this table to the Russian Chemical Society, which included empty entries for yet un-discovered elements (scandium for example), was a clear hint that the elements could be constructed from some underlying set of more fundamental "atoms". The discovery of the missing entries for Ge, Ga and Sc down the line (though with slightly different atomic number) was a true *tour de force* for Mendeleev's periodic tables of the elements. While

this was the first hint that there was some underlying building blocks of nature it was not a direct measurement.

The first direct measurement of one of the building blocks of the atom was made by Thompson in 1897. He discovered the electron using cathode ray tubes when he observed that beams emitted from a hot element could be deflected by a magnetic field and thus carried charge [13] [14]. The amount of deflection in magnetic and electric fields allowed one to determine the velocity and charge-to-mass ratio. Perhaps to his surprise, these quantities were independent of the type of gas used in the tube, suggesting a fundamental particle with fixed properties. This discovery marks what many refer to as the *birth of particle physics.*

If we take the liberty of selectively remembering history and ignoring the many blind alleys and dead ends that are so important to the advancement of science we come upon our next hero: Ernest Rutherford, the so called "father" of nuclear theory. His pioneering scattering experiment in 1914 on gold foil was the first direct measurement of the structure of matter within a gold atom. In the scattering experiment he observed that most of the α particle beam passed through a sheet of gold foil un-deflected except for a few which were wildly scattered [15]. The realization that almost all of the matter was contained within a tightly bound nucleus led directly to the orbital model for the atom proposed by Bohr [14]. This discovery of the proton, as Rutherford named the nucleus of the lightest atom H, approximately 2,600 years after the birth of a philosophical idea marked the second unequivocal measurement of *atomos.* The idea of neutrons, protons and electrons as the fundamental building blocks of nature became very common place. It wasn't until the early 1960s that the physics community would enter another new paradigm in our understanding of the truly indivisible units of nature. In the meantime, however, particle physics would be inundated with confusion and chaos.

During the period between the early 1900s and the late 1940s a few more particles were discovered. The neutron, discovered by Chadwick in 1932 [14], solved the puzzle concerning the mass scaling of atoms, where one expected to see the atomic number times the mass of the hydrogen atom. In addition, the Yukawa particle (also called the pion) was discovered.

It was posited to be the strong force exchange particle between the protons in the nucleus, which prevented the electromagnetic repulsion between like charges from tearing atoms apart. The particle nature of the photon was predicted by Einstein and the photo-electric effect he predicted was thoroughly tested experimentally. In addition, Fermi's prediction of the neutrino, though not measured experimentally, fit very well into the picture of the building blocks of nature around 1947. There were, however, a few hints that something might be amiss. For instance, the measurement of the mu meson (now called the muon and known to be a lepton) in 1936 prompted Rabi to ask, "Who ordered that?"

In scattering experiments conducted in the 1950s over a hundred new strongly interacting particles were observed. This vast collection of particles was often referred to as the *particle zoo*. Despite being able to classify the strongly interacting hadrons into the classes of heavy baryons and light mesons, overall there seemed no rhyme or reason to the situation [13]. In 1961, Gell-Mann suggested the *eight-fold way* as an explanation for the hadron akin to the periodic table. This scheme arranged the baryons and mesons into geometrical patterns according to their charge and strangeness. The modern version of this scheme [1] can be seen in Figure 1.1 where the hadrons are arranged according to charge, iso-spin and hyper-charge.

The understanding of nucleon substructure has proved an elusive goal since the scaling behavior predicted by Bjorken [16] was observed in deep inelastic scattering (DIS) experiments at SLAC in the late 1960s [17, 18]. In these experiments it was discovered that the photon momentum transfer (Q^2) dependence of the cross section decreased at larger values of the invariant mass (W) of the photon-nucleon system [18]. The loss of the nucleon size as a scale in DIS suggested that rather than a diffuse solid target, the nucleon was made up of point-like "partons," as they were termed by Feynman and Bjorken. However, it was soon realized that these partons were nothing more than the constituent quarks proposed by Gellman and Zweig in the (valence) constituent quark model of hadron spectroscopy [13]. In this parton model, one must "*...think of the incoming proton as a box of partons sharing the [total] momentum and practically free*" [19]. Despite some initial success, it was soon realized that the valence quark model could not account for the total cross-section at low

Figure 1.1: The modern versions of the *eight fold way* organization of the (a) mesons and (b) baryons according to charge (C), hyper-charge (Y) and iso-spin (I).

4

Bjorken-x and thus the modern quark-parton model (QPM) was constructed [17], wherein the nucleon is composed of the valence quarks immersed in a sea of quark and anti-quark pairs.

Our current understanding of the basic building blocks of matter is encapsulated in the standard model (SM) of particle physics. In this model there are six flavors of quarks and six leptons, which both come in three mass generations and have anti-particles [20, 13, 14]. These 24 fundamental particles interact through the exchange of four different gauge bosons: the electro-magnetic force, transmitted via photon (γ) exchange; the weak force transmitted through the exchange of charged-current (W) or neutral-current (Z) bosons; and the strong force transmitted by the exchange of gluons (g). More details about the SM, including the properties of the fundamental particles and the gauge bosons, can be found in the next chapter.

The goal of the experiments running at HERA was to systematically map out the distribution of partons inside the nucleon [21]. The two large experiments, H1 and ZUES, were able to detect inclusive deep inelastic scattering (DIS) events. This data could then be used to infer the momentum distribution of the different flavors of quarks and the gluons inside the nucleon. HERMES was designed to try and answer the question of how the quark spins in the nucleon conspire to give the overall spin of 1/2. Unlike the two larger experiments, HERMES had the ability to distinguish different hadronic final states in semi-inclusive DIS (SIDIS). This feature made it an excellent tool to study even the unpolarized quark distributions inside the nucleon through a technique often called *flavor tagging*. The analysis presented in the following chapters of this work will demonstrate the extraction of interesting unpolarized features of the nucleon from SIDIS data. In the second chapter we present the theoretical foundations that are assumed in order to interpret the data. In the third chapter we present the HERA accelerator and the HERMES detector with special attention paid to the detector features that set it apart from the large collider experiments. In the fourth chapter we discuss the data-taking periods, cuts and corrections used in the analysis and present the measured data in the form of multiplicities concluding with the model dependent partonic structure information that can be extracted from them.

Chapter 2

Theory

2.1 Standard Model of Particle Physics

The four different forces that govern our world cannot, as of yet, be united into a single overarching theory. The problem of integrating general relativity into the subatomic and sub-nuclear realms may be one of the greatest physics puzzles of our time. While this issue does not play a major role in the work presented it is clear that there is still some rather large holes in our understanding of our universe.

We do, however, have at our disposal an overarching description of three of the four forces in the form of the "standard model." In this model the subatomic world is composed of 12 point-like fermions, all of which have been experimentally confirmed, and five gauge bosons, four of which have been experimentally confirmed. The properties of the leptons [1] are listed in Table 2.1. One can see that the leptons come in three mass generations and that the nuetrinos have non-zero mass, which was discovered in neutrino oscillation experiments [22, 1]. The properties of the quarks are also listed in Table 2.1. Again we have the appearance of generations in the quark sector. Finally, Table 2.2, shows the properties of the gauge bosons including the Higgs (H), which has not been experimentally confirmed yet.

In the language of quantum field theory (QFT), the fundamental interactions between the particles and the equations of motion for the fields are represented by the Lagrangian. One can see from Eq. 2.1 that the total Lagrangian is constructed from the respective Lagrangians from electro-weak (Glashow-Salam and Weinberg) theory and quantum chromo dynamics (QCD). In a general sense the system can be completely described in terms of the action arising from the Lagrangian using a path-integral formalism [23]. In practice it

	leptons				quarks		
	mass	charge (e)	spin		mass	charge (e)	spin
e	0.510 MeV	1	1/2	up (u)	1.5-3 MeV	2/3	1/2
μ	105.6 MeV	1	1/2	down (d)	3-7 MeV	-1/3	1/2
τ	1776.9 MeV	1	1/2	strange (s)	95 MeV	-1/3	1/2
ν_e	< 2 eV	0	1/2	charm (c)	1.25 GeV	2/3	1/2
ν_μ	< 2 eV	0	1/2	bottom (b)	4.2-4.7 GeV	-1/3	1/2
ν_τ	< 2 eV	0	1/2	top (t)	172.3-174.2GeV	2/3	1/2

Table 2.1: Empirically determined properties of the leptons and quarks. All values presented in this table are the central values from the particle data book [1] in particular the masses of the light quarks have large error bars. The charge is presented in terms of the charge of the electron ($e = 1.602 \times 10^{-19}$C) .

bosons	mass	charge	spin
γ	$<6\times10^{-17}$eV	1	1
Z^0	91.18GeV	1	1
$W^{+,-}$	80.4GeV	1	1/2
g	0	0	1/2
$H^{\pm,0}$	$>114.4(>79.3)$GeV	$0(\pm1)$	0

Table 2.2: Empirically determined properties of the gauge bosons.

is rarely an easy task to do this, especially for the standard model Lagrangian.

$$\mathcal{L}_{SM} = \mathcal{L}_{EW} + \mathcal{L}_{QCD} \tag{2.1}$$

The standard model requires no less than 19 input parameters: three charged lepton masses, six quark masses, three gauge couplings, three quark mixing angles, one complex phase, a Higgs mass, a quartic coupling constant, and the QCD vacuum angle [20]. This "fine tuning" is often cited as some cause for alarm about the parsimoniousness of the theory.

In addition to this fine tuning we have measured conclusively that neutrinos have mass, which allows for both left and right-handed chirality. This is not a feature that is included in the theory, as only the left-handed neutrinos are put into the weak portion of the standard model Lagrangian.

The Higgs boson, which is required to break the symmetry in the EW theory thus giving the particles mass, has never been measured and at least the standard model Higgs

is very near to being ruled out by recent measurements of the top quark mass at the Tevatron [24, 1, 25].

Despite these less-than-paletteable features of the standard model, it has had remarkable success in predicting the particle interaction cross sections and no strong signal for physics beyond the standard model (PBSM) has been detected. Due to these successes, and the lack of firm experimental proof for PBSM, we assume firm theoretical footing for the following discussion of nucleon structure using the standard model, or more precisely QCD.

2.1.1 Quantum Chromo Dynamics

Quantum chromo dynamics (QCD) is the SU(3) non-abelian gauge theory that describes the interaction of quarks and gluons. It is a field-theoretic description which encapsulates the color charge (red, blue, green) carrying fermions called quarks and the strong force mediating gauge bosons called gluons [20]. The free Lagrangian for a particular flavor (up, down, charm, strange bottom or top) of quark is shown in Eq. 2.2.

$$\mathcal{L}_{free} = i\bar{\psi}\slashed{\partial}_\mu\psi - m\bar{\psi}\psi \tag{2.2}$$

Here, ψ is a vector with one four-component Dirac spinor entry for each of the three color charges. If one requires local SU(3) invariance of the Lagrangian, it must be stationary under transformations of the form:

$$\psi \rightarrow S\psi = \psi \rightarrow e^{iq\lambda\cdot\phi(x)}\psi \tag{2.3}$$

where λ are the eight Gell-Man matrices and the $\phi(x)$ are eight real numbers defined at each space-time point x. This expectation of local gauge invariance is motivated by the successful description of other theories (i.e. QED) in terms of local gauge invariance. We see that we must follow the usual prescription and introduce the *covariant derivative* $\mathcal{D}_\mu = \partial_\mu + iq\lambda \cdot A_\mu$. In this case, unlike QED, we see that there are actually eight vector

fields required. The modified Lagrangian is:

$$\mathcal{L}_{QCD} = -\frac{1}{4} F^{\mu\nu} F_{\mu\nu} + \bar{\psi} \left(i \slashed{D} - m \right) \psi \tag{2.4}$$

Where we have also added the gauge invariant kinetic energy term that is the free gluon Lagrangian. There is a very interesting feature buried in this equation that is very different from QED which comes from the fact that the Gell-Man matrices (on representation of the infinitesimal representation of SU(3)) are non-abelian and have the commutation relation $[\lambda_a, \lambda_b] = f_{abc} \lambda_c$ where f_{abc} are the structure constants of the group. This fact tells us that inside $F_{\mu\nu}$ a very different beast is lurking.

$$F_{\mu\nu} = \partial_\mu A_\nu - \partial_\nu A_\mu - q f_{abc} A_\mu^b A_\nu^c \tag{2.5}$$

We see immediately from the last term in Eq. 2.5 that the gauge symmetry we imposed causes the gauge field to have a self-interaction term. In layman's terms this means that the gluons couple not only to the quarks but to each other. A very nice way to see this effect is to write the Lagrangian in the symbolic form:

$$\mathcal{L} = \text{``}\bar{q}q\text{''} + \text{``}A^2\text{''} + \text{``}\bar{q}qA\text{''} + \text{``}A^3\text{''} + \text{``}A^4\text{''} \tag{2.6}$$

from this we infer several things: The first term represents the propagation of free quarks; the second represents free gluons; the third is the gluon-quark interaction vertex; the fourth is a three-gluon interaction; and the last a four-gluon interaction. In fact it is these internal gluon bubble lines, a consequence of the fact that gluons can couple to each other, that lead to asymptotic freedom [13, 26]. The running coupling constant of QCD to first order is given by:

$$\alpha_s(\mu) = \frac{4\pi}{\beta_0 \ln \mu^2 / \Lambda^2} \tag{2.7}$$

While the derivation of this is left to authors much more expert on the subject, one can list the steps that are required to derive this result in a schematic fashion. The loops that

appear on the internal lines of the Feynman diagram lead to corrections in the coupling constant. In QED we only have loops where, for instance, a photon splits into a positron electron pair. In fact, if one truly wishes to calculate a quantity that corresponds to what is measured experimentally, all of these loops must somehow be included in the sum of diagrams (and there are an infinite number). Mathematically this is achieved through renormalization by summing up all of these internal loops and hiding them inside the coupling constant, which leads to the famous running coupling in QED. In QCD the effect is slightly different because the gluon loops send the coupling in the opposite direction such that the coupling constant runs the other way. In other words, as we look closer in QCD (higher energy) things tend to behave as if they were free, that is, the coupling decreases and perturbative techniques become applicable [13, 27, 28].

2.1.2   pQCD and DIS

One can attempt to proceed with the formal technique of perturbation for QCD interactions. This amounts to solving for the full Green's function (propogator) for a point-like potential. Once this propogator is calculated, as we know from the usual application of Green's functions, the solution can be found by integrating the potential with the Green's function as the kernel [27]. Using this technique Feynman invented a diagrammatic technique that allows us to write down (almost effortlessly) the matrix elements that correspond to a given scattering interaction.

For QCD, due to the non-abelian nature of the theory, the perturbative regime is that of large energies that correspond to small distance scales and short times, i.e. large energy transfer in the probe. In this limit, the interaction between the quarks in the nucleon is small and one can express the cross section for DIS at lowest order in QCD as the interaction of a virtual photon with the nucleon. This feature allows us to use QED, known to be in excellent agreement with theoretical calculations as our probe of the QCD structure inside the nucleon.

The DIS process is depicted in Fig. 2.1. Using the Feynman rules of pQCD it is straightforward to write the amplitude ($\mathcal{M}$) for the interaction of a virtual photon, emitted by an

10
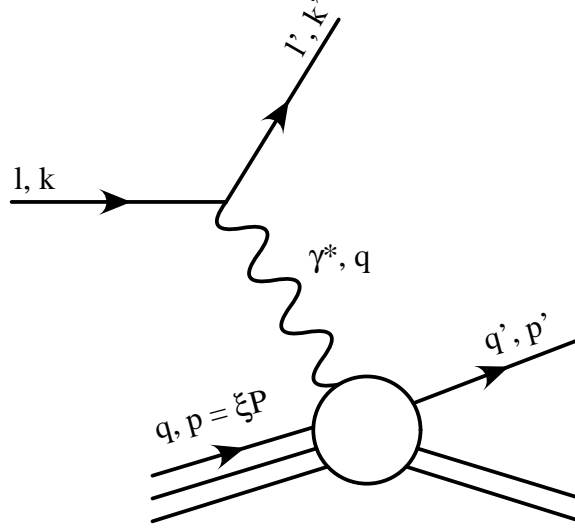
Figure 2.1: Here the DIS process is depicted where the virtual proton probes the internal structure of the nucleon and only the scattered lepton is measured in the final state. The measurement is termed inclusive as all final states of the scattered quark is included.

electron, that interacts with a proton with polarization σ:

$$\mathcal{M}_n = e^2 \bar{u}(k', s') \slashed{\psi}(k, s) \left(\frac{1}{q^2} \right) \langle n | J_\mu | p, \sigma \rangle \tag{2.8}$$

where the state n is some unknown final state and the matrix element represents the unknown interaction of the electromagnetic current J_μ with the proton. The incoming and outgoing four momentum of the lepton are given by k and k' respectively. Additionally, if the electron is polarized one must keep track of the initial (s) and final (s') polarization, though in practice the spin states are often summed over. Here we also see the familiar photon propagator $1/q^2$ and by momentum conservation at the lepton vertex it is obvious that:

$$q^2 = (k - k')^2 \tag{2.9}$$

We pause the derivation of the DIS cross section here for a moment to introduce a few more commonly used kinematic variables (Eq. 2.11) in the description of the DIS scattering process.

11

$$Q^2 = -q^\mu q_\mu \overset{lab}{=} -4k^0 k^{0\prime} \sin^2(\theta/2) \tag{2.10}$$

$$W^2 = (P^\mu + q^\mu)^2 \overset{lab}{=} M^2 + 2M\nu - Q^2 \tag{2.11}$$

$$x = Q^2/(2P_\mu q^\mu) \overset{lab}{=} Q^2/(2M\nu)$$

$$y = P^\mu q^\mu / P_\mu k^\mu \overset{lab}{=} \nu//k^0$$

$$\nu = (k^0 - k^{0\prime}) = q^0$$

Here, Q^2 is the squared invariant mass of the off-shell virtual photon and large Q^2 ($\rightarrow \infty$), as pointed out above, represents small length scales where the perturbative QCD expansion is valid. W^2 is the squared invariant mass of the final state and is used to ensure that the proton was broken up in the DIS process. Large W^2 enforces the requirement that we are in the continuum rather than just exciting the proton into some resonant state which then decays. This will be particularly important when we turn our attention to semi-inclusive deep inelastic scattering (SIDIS).

Using Fermi's golden rule [29, 30] which tells us that the transition from state a to state b is given by the product of the amplitude and the density of final states available ($T_{a\rightarrow b} = \frac{2\pi}{\hbar} |\mathcal{M}_{ab}|^2 \rho$), we can express the differential cross section for the lepton to scatter into a solid angle Ω with energy $k^{\prime 0}$ as [27]:

$$\frac{d^2\sigma}{d\Omega dk^{\prime 0}} = \frac{\alpha^2}{q^4} \frac{k^{\prime 0}}{k^0} l^{\mu\nu} W_{\mu\nu} \tag{2.12}$$

Here, the leptonic tensor (Eq. 2.13) represents the well known QED vertex and can be written as a sum of its symmetric and anti-symmetric parts $L_{\mu\nu} = L_{\mu\nu}^{(S)} + L_{\mu\nu}^{(A)}$. However, the anti-symmetric portion of the leptonic tensor cancels when the beam and target spins are averaged, as is the case of unpolarized deep inelastic scattering.

$$l_{\mu\nu} = (\bar{u}\gamma_\mu u)(\bar{u}\gamma_\nu u) = \frac{1}{2} Tr(\slashed{k}'\gamma_\mu \slashed{k}\gamma_\nu) = 2(k'_\mu k_\nu + k_\mu k'_\nu + \frac{q^2}{2} g_{\mu\nu}) \tag{2.13}$$

The hadronic tensor $W_{\mu\nu}$ must therefore be symmetric as well (to preserve the parity-

conserving nature of the electromagnetic interaction), and will allow us to characterize our lack of knowledge concerning the hadronic vertex [28]. The hadronic tensor is given by:

$$W_{\mu\nu} = \frac{1}{4M} \sum_{\sigma} \int \frac{d^4\epsilon}{2\pi} e^{iq\cdot x} \langle P, \sigma| \left[J_\mu(0), J^\nu(\epsilon) \right] |P, \sigma\rangle \tag{2.14}$$

Where we have removed a *well chosen one*, that is the sum over all the unknown states n ($\sum_n |n\rangle \langle n| \equiv 1$), from the hadronic tensor. Additionally, the product of the two currents can be written as a commutator because the $J_\nu(x)J_\mu(0)$ term is forbidden by energy conservation. When the most general form of $W_{\mu\nu}$ is constructed, using only the Lorentz invariant momentum vectors and the Minkowski metric, four unknown parameters are required. However, we know from Noether's theorem and the fact that the action is stationary under internal symmetry that the current is conserved $\partial_\mu J_\mu = 0$ at the hadron vertex, which implies $q^\mu W_{\mu\nu} = 0$ [13, 27, 28]. As a result the most general form of the hadronic tensor, which can only depend on q and P, is given by only two free parameters:

$$W_{\mu\nu} = W_1 \left(-g_{\mu\nu} + \frac{q^\mu q^\nu}{q^2} \right) + \frac{W_2}{M^2} \left(P_\nu - q_\nu \frac{P \cdot q}{q^2} \right) \left(P_\nu - q_\nu \frac{P \cdot q}{q^2} \right) \tag{2.15}$$

Experimentally the scaling predicted by Bjorken [16] has been measured in DIS [18, 1]. In the limit of large momentum transfer the dependence on $Q^2 = -q^2$, in the DIS regime, for the structure functions is replaced by a dependence on x. This allows us to translate from $W_n(q^2, \nu)$ to $F_n(x)$ in the final inclusive cross section, which as a function of the dimensionless variable y is given by:

$$\frac{d^2\sigma_q}{dx dQ^2} = \frac{4\pi\alpha^2}{xQ^4} \left[(1 + (1-y)^2)F_2 - y^2 F_L \right] \tag{2.16}$$

Here, we have introduced the function F_L motivated by the Callan-Gross relation:

$$F_L = F_2 + 2xF_1 = 0 \tag{2.17}$$

This relation is motivated by the result of helicity conservation at the vertex of a massless parton [1, 31]. It is important to note that this relationship must hold in the limit of real

on shell photons which are only allowed to have transverse polarization. These features motivate one to introduce the quark-parton model in order to understand why, in the Bjorken limit, the Callan-Gross relation gives:

$$\frac{d^2\sigma}{dx dQ^2} = \frac{4\pi\alpha^2}{xQ^4} \left[(1 + (1-y)^2)F_2 \right] \tag{2.18}$$

2.1.3 Quark Parton Model

One simple explanation for the scaling behavior observed in DIS is that the nucleon is composed of point like constituents called partons. In this case once the probe reaches a short enough wavelength ($\sim 1/Q^2$) to resolve these constituents the measured structure functions will no longer have a dependence on the scale Q^2. This interpretation of the nucleon's internal structure is called the quark parton model.

In the quark parton model one assumes that the nucleon is made up of some momentum-dependant number-density distribution of partons ($q(p_q)$) each with charge (e_q), then the structure function is just the incoherent sum of the hard scattering from these point-like constituents. For the sum to be incoherent we invoke the impulse approximation which requires the photon-parton interaction to take place on short enough time scales that the partons cannot interact with each other and are essentially free. If we further assume that the parton has negligible primordial transverse momentum we can express its momentum as some fraction ξ of the proton's momentum $p_q = \xi P$. From this simple picture and the enforcement of momentum conservation at our newly posited photon parton vertex in the scaling limit $Q^2 >> \xi^2 P^2, p'$ we have [27]:

$$\lim_{Q^2 \gg \xi P, p'} \left[p'^2 = \xi^2 P^2 + q^2 + 2M\nu\xi \right] \tag{2.19}$$

$$\xi = Q^2/2M\nu \equiv x$$

where p' is the momentum of the outgoing parton. We see that the essence of scaling arises from a very simple picture that the momentum of the proton is carried by point-like

constituents. In this picture, the structure functions are given by the incoherent sum of the parton momentum distribution functions (PDFs) $q(x)$ weighted by the square of their electromagnetic charge e_q.

$$F_2 = x \sum_q e_q^2 (q(x) + \bar{q}(x)) \tag{2.20}$$

One immediately see in Eq. 2.20 that from an experimental point of view inclusive DIS is only sensitive to the sum of quark and anti-quark distributions. However it turns out that Bjorken scaling is only approximately obeyed in nature. This has led to the so called *QCD improved parton model* that reintroduces some slight scale variation and thus reintroduces some explicitly calculable dependence on Q^2 into the structure functions (PDFs). This scale-breaking and its interpretation is discussed in the following section.

With the parton model in hand, we can attempt to construct sum rules that give us a meter stick to test our assumptions of the nucleon's substructure. First off, we know that certain properties (charge, spin) of the nucleon are described well in the valence parton model. For the proton this should give us two up quarks and one down quark. In this model the proton, for instance, is described as a bound state of two up quarks and one down quark. We can therefore integrate over all the possible momentum fractions (x) of the valence quarks to derive the following sum rule.

$$\frac{d_v}{u_v} = \frac{\int_0^1 dx d_v(x, Q^2)}{\int_0^1 dx u_v(x, Q^2)} = \frac{1}{2} \tag{2.21}$$

Another interesting sum rule, called the Gottfried sum rule (GSR) Eq. 2.22, is the result of the assumption of a flavor-symmetric light sea, as one might expect from perturbative gluon splitting. If this is the case then the integral over the sea quark distributions cancels and only the valence quark distributions contribute. In this study, we will report data from past and present experiments that seem to violate the GSR, thus demonstrating a noticeable $\bar{u}$, $\bar{d}$ asymmetry which rules out the assumption of a purely perturbative light

15

sea.

$$S_G \equiv \bar{d} - \bar{u} = \int_0^1 \frac{dx}{x} \left[F_2^p(x, Q^2) - F_2^n(x, Q^2) \right] = \frac{1}{3} + \frac{2}{3} \int_0^1 dx \left[\bar{d}(x, Q^2) - \bar{u}(x, Q^2) \right] \neq \frac{1}{3}$$

(2.22)

2.1.4 DGLAP and PDF Fits

The fact that the parton distribution functions do not follow Bjorken scaling perfectly is due to the existence of gluon radiation. The Alterelli-Parisi equations encode this fact in a set of splitting functions (P_{ij}) which describe the probability of a quark emitting a gluon that then converts to a quark at lower momentum [28].

$$Q^2 \frac{\partial}{\partial Q^2} q_i(x, Q^2) = \sum_j \int_x^1 \frac{dx'}{x'} \frac{\alpha_s}{2\pi} P_{ij}(x, \alpha_s) q_j(x/x', Q^2)$$

(2.23)

Here, we have used the subscripts on the PDFs to represent the PDF at two different scales. We see that when referring to PDFs we must include the variation with Q^2 in any expression of the cross section or PDFs ($q(x) \to q(x, Q^2)$). In practice this dependence can be corrected out of measured quantities using the DGLAP formalism [32].

This slight scale-breaking itself provides a rather useful tool for parameterizing parton distribution functions. A set of parameterized PDFs can be evolved from the input scale (μ_0) to any other scale (μ) via Eq. 2.23. Using the expansive data set collected on inclusive DIS (Fig. 2.2) one can minimize a χ^2 statistic and extract fits of the parton distributions (Fig. 2.3) [9, 8, 2]. However, these global next to leading order (NLO) and next to next to leading order (NNLO) fits still suffer from the inherent lack of separation of quark and anti-quark degrees of freedom.

2.1.5 Semi-Inclusive DIS in pQCD

There is another readily available technique for exploring the structure of the partons inside the nucleon that can separate quark and anti-quark distributions. The technique is based on *flavor tagging* in semi-inclusive DIS (SIDIS). Flavor tagging posits that by measuring a
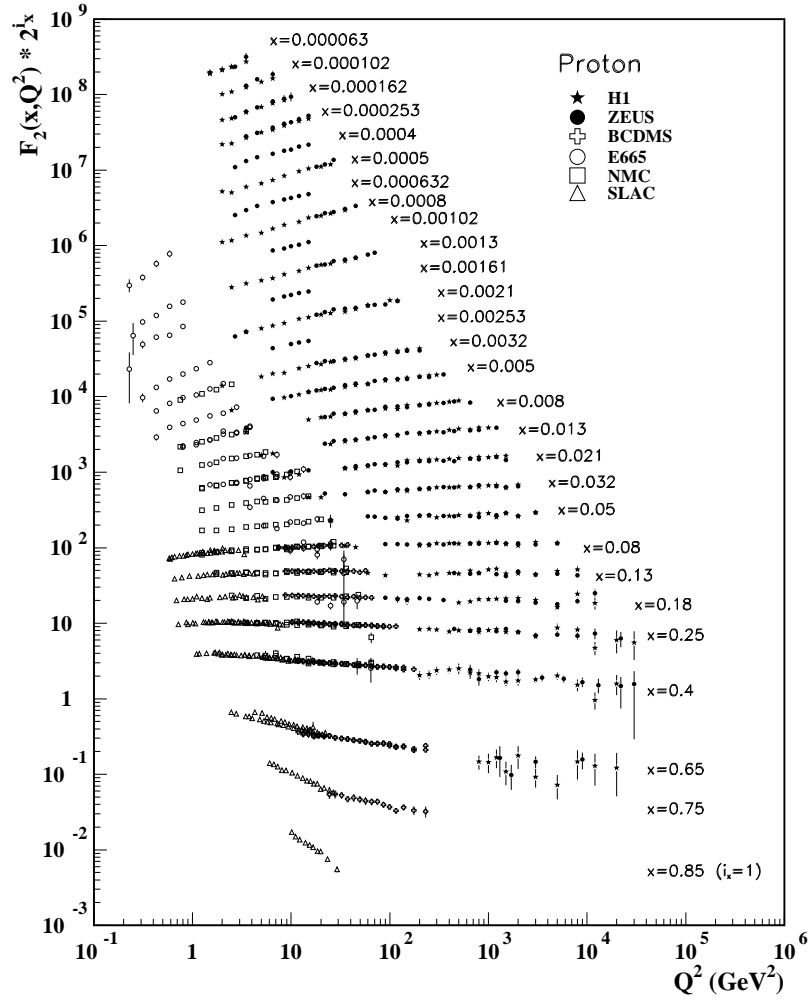
Figure 2.2: Inclusive structure function data collected at HERA, SLAC, CERN, FNAL and other collider experiments.
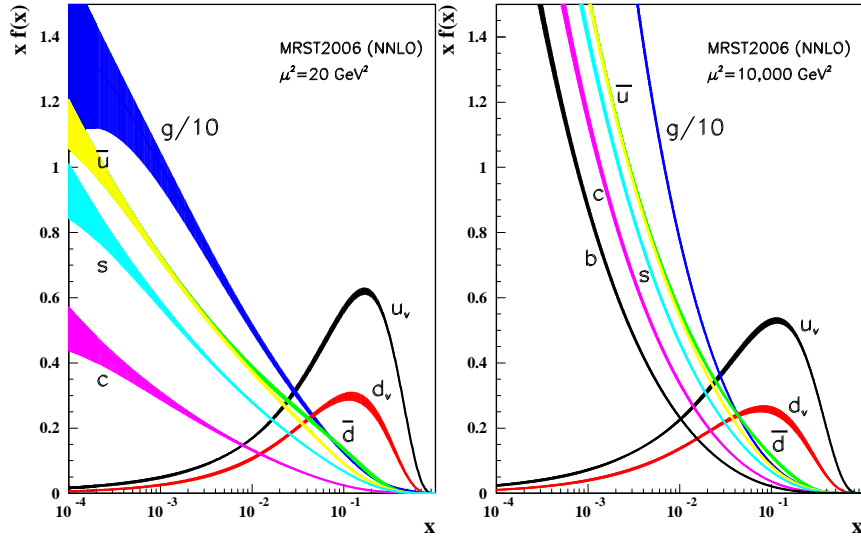
Figure 2.3:   Parton distribution fits extracted from inclusive data using NNLO DGLAP evolution formalism. The resulting fits and errors are shown at two different scales, 20 and 10000 GeV^2. The fits shown here are from the MRST2006 group [2, 1].
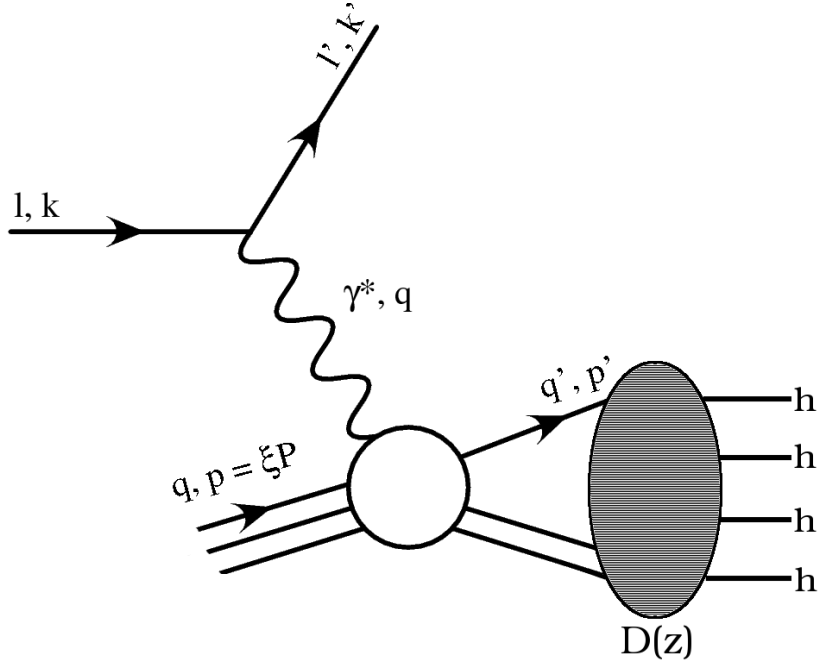
Figure 2.4:   Here the SIDIS process is depicted where the fragmentation function $D(z)$ describes the soft process by which the scattered quarks recombine to form colorless hadrons.

specific hadron in the final state having a well known valence quark content one can establish a correlation to the flavor of the struck quark. We will return to this idea momentarily, but we must first introduce the scattering cross section for SIDIS. The cross section for this interaction needs to be fixed up to include a term that describes how we get from a scattered parton to the final state hadron. If we assume that this soft hadronization process is well separated from the hard interaction, we can factorize the two effects. With the assumption of the parton model and the assumption of factorization we can write a similar expression for the semi-inclusive DIS cross section:

$$\frac{d^3\sigma^h}{dxdzdQ^2} = \frac{4\pi\alpha^2}{Q^4}\left[(1 + (1-y)^2)\sum_q e_q^2(q(x,Q^2) + \bar{q}(x,Q^2))D_q^h(z,Q^2)\right] \qquad (2.24)$$

Here, we have introduced a new quantity $z = E_h/\nu$, which is a measure of the fractional energy available from the virtual photon (ν) that the final state hadron carries. We have also introduced the fragmentation function D_q^h to describe the soft process, we will discuss these in more detail in the following section. The measured yield of hadrons in a SIDIS event is related to the cross section via:

$$N^h(x, Q^2, z) = A\mathcal{L}d^3\sigma^h(x, z, Q^2) \qquad (2.25)$$

Where $\mathcal{L}$ is the luminosity rate and A is a function describing the detector acceptance. As mentioned above, the important feature of SIDIS is that it has the ability to separate quarks from anti-quarks due to the possibility of differing values of the fragmentation function. These functions allow one to correlate the flavor of the struck quark with the final state hadronic distributions using the fragmentation functions a technique that is called "flavor tagging."

2.1.6 Fragmentation Functions

The fragmentation functions (FFs) are tools that parameterize our ignorance about the soft process that turns the scattered quark and the nucleon remnant back into natural colorless
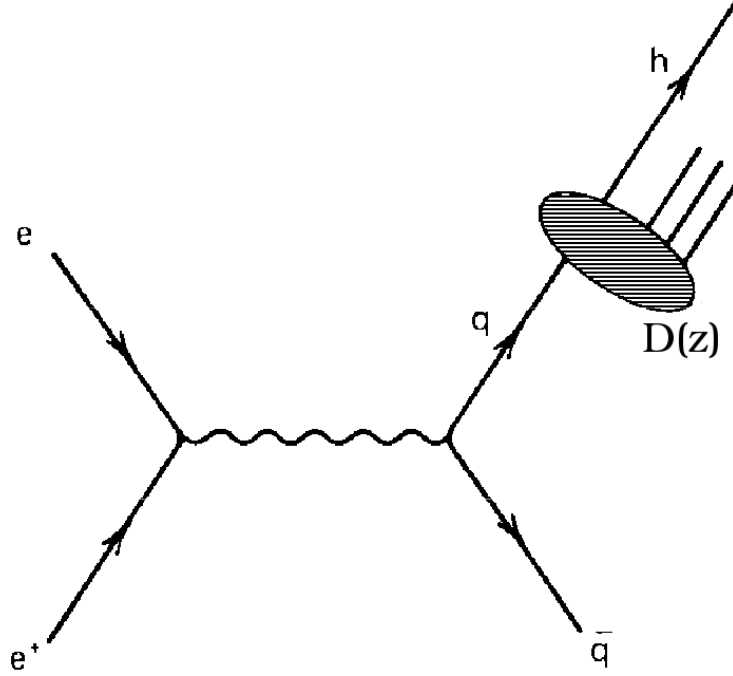
Figure 2.5: The typical process used to determine fragmentation is pair annihilation at electron positron colliders (e.g. LEP).

objects. This is very similar to the structure functions that we used to parameterize our ignorance about the nucleon structure but represents the soft process illustrated by the hatching in Fig. 2.4. These functions have the conservation law in $e^+e^- \to hX$:

$$n_h = \sum_{f=q,\bar{q}} \int_0^1 dz e_f^2 \int D_f^h(z) \tag{2.26}$$

where n_h is the number of hadrons of type h observed in one scattering event. Which is to say that the fragmentation function represents, in a statistical sense, the number of hadrons of type h that will be produced in one scattering event when the fragmenting quark is of flavor q. The typical technique for measuring FFs is hadron production at electron positron colliders, where the electron and positron annihilate and produce a hadronic jet in the final state, see Fig. 2.5.

The fragmentation functions are also subject to a DGLAP evolution with the scale of

the interaction.

$$\frac{\partial}{\partial logQ^2} D_i^h(z, Q^2) = \sum_j \int_x^1 \frac{dz'}{z'} \frac{\alpha_s}{2\pi} P_{ji}(z, \alpha_s) D_j^h(x/z', Q^2) \tag{2.27}$$

While this is very similar to the DGLAP evolution equation for parton distribution functions, there is a subtle difference. Namely, the splitting function has the order of the indexes reversed. This is because it is the final-state parton that changes from type i to type j since D_j^h represents the fragmentation of the final-state parton [1]. The available $e^+ + e^- \to q\bar{q} \to Xh$ data can be parameterized by exploiting this scaling. There are a few well known groups that attempt to do this [3, 4, 33, 5]. One major weakness of this technique is that the data does not allow one to specifically separate the quark flavor dependencies. In these fits, they assume iso-spin and charge conjugation symmetry in order to fit these quantities. This symmetry is often referred to as the (dis) favored fragmentation where the fragmentation function for a final state hadron that (does not) contains a valence quark of the same flavor is called (D_2) D_1.

$$D_1 \equiv D_u^{\pi^+} = D_{\bar{u}}^{\pi^-} = D_{\bar{d}}^{\pi^+} = D_d^{\pi^-} \tag{2.28}$$

$$D_2 \equiv D_{\bar{u}}^{\pi^+} = D_u^{\pi^-} = D_{\bar{d}}^{\pi^-} = D_d^{\pi^+}$$

Recently the FF parameterizations from [34, 5] have also used HERA SIDIS data as inputs and does not assume the symmetry above. It is not unexpected that the fDSS fits match the HERMES MC prediction more closely. Unfortunately, at the time of this writing the AKK [34] parameterization code was not available for inclusion in the comparison.

Parallel to the fitting attempts of the fragmentation functions, many authors have tried to develop QCD-inspired phenomenological models. The FF can not be calculated from QCD because they represent an inherently non-perturbative process. These include string models, recombination, and cluster fragmentation to name a few [1]. Recombination is the idea that partons need only to be near each other in phase space and have the correct quantum numbers for a hadron to recombine. It has found particular success in describing

hadronization in cold and hot nuclear environments where the vacuum state is modified [35]. Cluster fragmentation non-perturbatively splits the remaining gluons at the end of the perturbative parton shower into $q\bar{q}$ pairs [36]. These color clusters with energy on the order of one GeV are then decayed directly into hadrons.

String models represent the fragmentation process in terms of the energy stored up the gluon color field between to partons moving apart. When the energy in the string reaches a some critical value the string may *break* and pull a $q\bar{q}$ pair out of the vacuum. This process continues creating a cascade of partons which, using the cutoff in energy for producing more pairs, can be grouped into hadrons. The most commonly used model in most SIDIS Monte Carlo simulations (i.e. JETSET) of hadron production (excluding hadronization in modified *vacuo*), is called the LUND string model [37, 38]. This model represents the energy stored in the color field between the scattered parton and remaining quarks (remnant) in terms of a Hooke's law potential. The pair creation occurs according to a tunneling process $e^{-\pi m_{q,\perp}^2/k}$ where $m_{q,\perp}^2 = m_q^2 + p_{q,\perp}^2$ is the transverse mass and k is the string tension (1GeV). The dependence on the quark mass effectively suppresses heavy quark and thus heavy hadron production. The string fragmentation function takes the form:

$$f(z) \propto \frac{1}{z}^a e^{-bm_{h,\perp}^2/z} \tag{2.29}$$

where a and b are free parameters that must be tuned to make the model agree with experimental data. These models can provide excellent simulation tools to study effects such as the breaking of the favored symmetries as they do not *a priori* include this assumption.

2.1.7 Fragmentation Symmetries and Factorization

The formalism used to extract PDF information from multiplicities, which will be discussed in Section 2.4, depends heavily on assumed fragmentation symmetries. First, fragmentation universality is assumed so that the ^{3}He fragmentation function can be used in the ratio. This was shown in the analysis to be reasonable, because the fragmentation functions for all three targets were not significantly different. Additionally, one has to apply the idea of favored versus dis-favored fragmentation (Eq. 2.28), assuming that all hadrons which

22
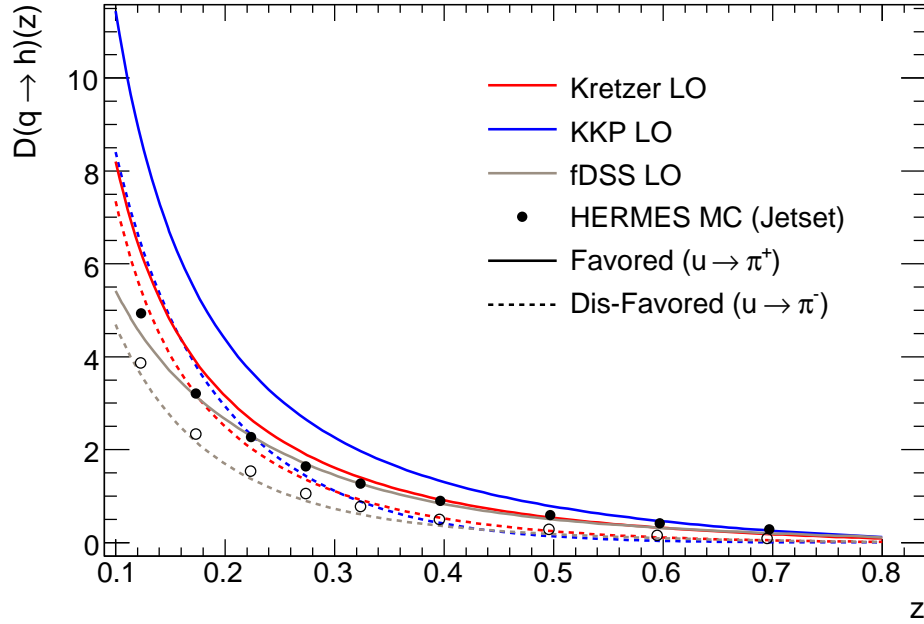
Figure 2.6: Examples of fragmentation function parameterizations [3, 4, 5] from fits to primarily e^+e^- data at LEP. Also shown are the results for favored (filled circles) and dis-favored (open circles) resulting from the HERMES MC using the LUND string model.

contain the struck quark have the same fragmentation function and *vice versa*.

In the previous analysis, the fragmentation functions were extracted from an independent data set on the ^{3}He target. However, if the universality of fragmentation functions holds, we should be able to use the world parameterizations (Kretzer or KKP) [4] [3] of fragmentation functions from e^+e^- colliders. These fragmentation functions can be Q^2 de-evolved to the HERMES kinematics, using the DGLAP equations. Fig. 2.6 demonstrates that the fDSS and Kretzer, to a lesser extent at low z, e^+e^- FF parameterizations agree well with the HERMES MC LUND model based prediction.

In contrast to these world parameterizations, data from the BELLE collaboration can be used to produce fragmentation functions at energies closer to the center of mass energy of HERMES. These data would be very useful in this analysis because they could provide e^+e^- fragmentation functions without the errors and uncertainties that result from a large Q^2 evolution. Further study is needed as to which parameterization or data set is best suited for this analysis. Exploring this issue may uncover better methods for describing the

fragmentation process at HERMES.

The second check is to verify that, within reasonable error, the HERMES fragmentation functions display the favored/dis-favored fragmentation symmetry, for $0.2 < z < 0.8$, which is assumed in the formalism. The testing ground for this question is the phenomenological Monte Carlo based on the Lund string model of fragmentation. A major effort has been made at HERMES to tune the Monte Carlo to reproduce unpolarized multiplicities. The most recent (current) tune is the result of a genetic algorithm which minimizes the variation from the unpolarized multiplicities. Having the simulation is invaluable in cases like this, where quantities that are not recoverable from actual data can be simulated and checked. Using the HERMES Monte Carlo, fragmentation functions have been extracted and their symmetries have been studied extensively by the author. Fig. 5.3 shows the favored fragmentation function comparisons for different quark flavors. Different targets have also been investigated. These tests have revealed that the favored/dis-favored fragmentation symmetries are broken at $\approx$ the 5-10% level, which will contribute to the total systematic error.

2.2 Experimental Status

2.2.1 DIS Experiments

After the discovery of the "EMC Effect" at CERN, the EMC detector was modified to reach the low-x region for the New Muon Collaboration (NMC) to study the effect in detail [17]. NMC used muon-induced DIS to measure the structure function F_2^d and the ratio F_2^n/F_2^p at $< Q^2 >= 4\,\mathrm{GeV}^2$ over a large range in x. Combining these quantities gives the non-singlet structure function

$$F_2^p - F_2^n = 2F_2^d(1 - F_2^n/F_2^p)(1 + F_2^n/F_2^p) \qquad (2.30)$$

and allowed NMC to evaluate the GSR in the $0.004 < x < 0.800$ range. When the value is extrapolated to the unmeasured region using the latest world parameterization for F_2^d, the value $S_G = 0.235 \pm 0.026$ is found, which violates the GSR at the 4σ level. This was a compelling result, suggesting that the iso-spin symmetry of the light sea ($\bar{u} = \bar{d}$), which

follows from a completely perturbative sea, is an incorrect assumption.

The HERMES experiment at DESY has also published results on the light sea asymmetry in the proton from SIDIS data, which is presented later in some detail.

2.2.2 Drell-Yan Experiments

The NA51 experiment at CERN was specifically designed to explore the apparent violation of the GSR seen by NMC. The spectrometer measured dilepton production near zero rapidity where, neglecting the sea-sea contributions, the Drell-Yan target asymmetry takes the following form [17] [39]:

$$A_{DY}(x) = \frac{\sigma^{pp} - \sigma^{pn}}{\sigma^{pp} + \sigma^{pn}} = \frac{(4\lambda_v - 1)(\lambda_s - 1) + (\lambda_v - 1)(4\lambda_s - 1)}{(4\lambda_v + 1)(\lambda_s + 1) + (\lambda_v + 1)(4\lambda_s + 1)} \qquad (2.31)$$

Here $\lambda_v(x) = u_v(x)/d_v(x)$ and $\lambda_s(x) = u_s(x)/d_s(x)$. To measure this asymmetry, NA51 had to make the common assumption that the deuteron cross section is the sum of the proton and neutron cross sections. Experimentally, a 450 GeV proton beam was scattered from liquid hydrogen and deuterium targets to study the asymmetric dilepton production from neutrons and protons. The data consisted of approximately 2763(3007) muon pairs, with $M_{\mu\mu} >$ 4.3 GeV to ensure Drell-Yan production, from $H_2(D_2)$ using the NA10 spectrometer. This zero rapidity measurement ensured that the momentum fractions of the interacting partons was the same, thus validating the simple x dependence of the asymmetry, $(x_1 = x_2 = x)$, but limited the measurement to one x value of $M/\sqrt{(s)} = 0.18$. If one assumes the standard valence distribution ($\lambda_v \approx 2$) and a completely symmetric light anti-quark sea ($\lambda_s = 1$) then an asymmetry of $A_{DY} = 0.09$ would be expected. In contrast to these simple assumptions, NA51 measured A_{DY} to be $-0.09 \pm 0.02(stat) \pm 0.025(syst)$, which established the light anti-quark asymmetry at one value of x. When the measured asymmetry is combined with the valence assumption, one finds $\lambda_s = \bar{u}/\bar{d} = 0.51 \pm 0.04(stat) \pm 0.05(syst)$ [17, 39].

After NA51 verified the light anti-quark asymmetry suggested by NMC, the E866/NuSea collaboration at Fermilab systematically mapped out its x dependence in the range $0.02 < x < 0.345$. This experiment used an 800 GeV proton beam and also scattered off liquid hydrogen and deuterium targets to measure Drell-Yan dimuon production. Using the E605

detector, with large acceptance for $x_F > 0$, gave E866 sensitivity to the anti-quarks in the target. One can derive the ratio of hydrogen and deuterium cross sections in this limit, assuming $x_1 \gg x_2$ and $d(x) \ll 4u(x)$ to be [7]

$$\frac{\sigma^{pd}}{2\sigma^{pp}}_{x_1 \gg x_2} \approx \frac{1}{2}\left[1 + \frac{\bar{d}(x_2)}{\bar{u}(x_2)}\right] \tag{2.32}$$

Here, x_1 refers to the Bjorken-x of a parton in the beam while x_2 is for the target parton. Using this experimental setup and dimuon mass cuts to exclude known J/Ψ and Υ resonances the E866 collaboration was able to measure the data shown in Fig. 2.7. If the data is extrapolated to the unmeasured $0 < x < 0.015$ region using the CTEQ5M distributions, E866 finds a GSR value of 0.118 ± 0.012. This is still in violation of the symmetric anti-quark sea assumption ($1/3$) and is $4/5$ of the NMC result.
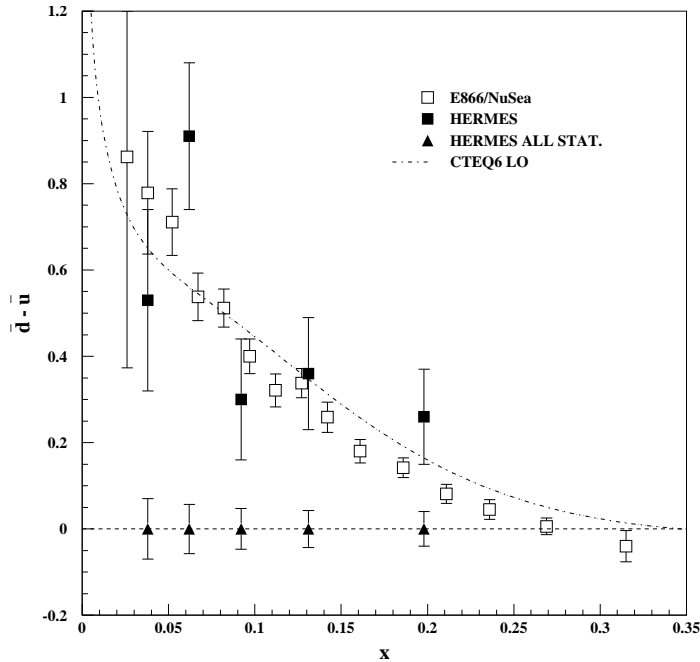
Figure 2.7: The closed squares represent the previous HERMES publication [6] of the light sea asymmetry as compared to the E866/NuSea collaborations data [7] in open squares. For both the HERMES data and the E866 data, only statistical errors are represented for comparison to the closed triangles, which are the projection for the statistical precision HERMES should obtain. Also, shown on the plot as a dash-dotted line is the CTEQ6 [8] parameterization of the world data at $\langle Q^2 \rangle = 2.5$.

There is currently a proposal for a measurement of the larger $x > 0.2$ region using the

main injector at Fermilab by the P906 collaboration. Using proton-induced Drell-Yan from liquid hydrogen and deuterium targets, the ratio in Eq. 2.32 will be measured. The large x contribution to the GSR is thought to be small, however the P906 measurement will continue to enhance our understanding of the light sea quark asymmetry over the entire kinematic range.

2.3   SIDIS Multiplicities

One can measure the average number of hadrons produced per DIS scattering event. This quantity is called the hadron multiplicity m^h and is related to the PDFs and FFs through the equation:

$$m_t^h(x,z) = \frac{1}{\sigma_t(x)}\frac{d^2\sigma_t^h}{dxdz} = \frac{1}{N_t^{DIS}(x)}\frac{N_t^h(x,z)}{\Delta z} \tag{2.33}$$

where t represents the scattering target and h is the final state observed hadron type. This quantity is a physical observable and does not require any assumption about factorization or fragmentation symmetries. One can measure this quantity in SIDIS experiments, particularly those which have the ability to separate hadron types in the final state. It is of course necessary to correct the data in order to compare it to theoretical calculations which know nothing of the HERMES acceptance, this point will be discussed later in detail. The multiplicities can also be used in the parameterization of fragmentation functions though there are few groups who use SIDIS data at this point. We will demonstrate in the following work the measurement of these quantities and the subsequent assumption dependent extraction of PDF properties.

2.4 Extracting PDF Quantities from Multiplicities

2.4.1 Extraction of the Valence PDF Ratio Asymmetry at HERMES

In the LO parton model the hadron yield from a nucleon can be described by the incoherent sum of the scattering from individual quarks weighted by the square of the quark charge.

$$\sigma_q^h(x,z) \propto \Sigma_q e_q^2 q(x) D_q^h(z) \tag{2.34}$$

Here, we have assumed that the factorization of the parton distribution and the fragmentation function holds in the DIS regime [40, 41]. Additionally we assume (since the pion yields give us no handle on them) that all the strange contributions to the pion yield take the following form.

$$s(x) = \bar{s}(x) \quad \& \quad D_s^h \equiv D_s \tag{2.35}$$

These can then be cancelled when we take the difference of any two pion yields. In fact, we can construct the ratio quantities below in order to cancel the strange contribution (difference) and ignore the Mott cross section and other kinematic pre-factors (ratio).

$$r^\pi = \frac{\sigma_n^{\pi^+}(x) - \sigma_n^{\pi^-}(x)}{\sigma_p^{\pi^+}(x) - \sigma_p^{\pi^-}(x)} \tag{2.36}$$

Due to the lack of a free neutron target we must leverage the deuteron and proton targets to extract the neutron cross section:

$$\sigma_n^h \equiv 2\sigma_d^h - \sigma_p^h \tag{2.37}$$

It should be stated that this relation only holds if the luminosity used to calculate the cross section is defined as "per nucleus." Applying Eq. 2.37 to find:

$$r^\pi = \frac{2(\sigma_d^{\pi^+}(x) - \sigma_d^{\pi^-}(x))}{\sigma_p^{\pi^+}(x) - \sigma_p^{\pi^-}(x)} - 1 \tag{2.38}$$

Expanding in the LO parton model (Eq. 2.34), and assuming the favored and dis-favored fragmentation function symmetries (2.28) we see that one can determine the valence quark distributions in the proton from the flavor tagged SIDIS production of pions.

$$\frac{d_v}{u_v} \approx \frac{4r^\pi + 1}{r^\pi + 4} \tag{2.39}$$

One could also choose a different normalization method, i.e. using the total inclusive DIS yield rather than the absolute luminosity. In this case r^π can be re-written in terms of the hadron multiplicities m_t^h.

$$r^\pi = \frac{m_d^{\pi^+} - m_d^{\pi^-}}{m_p^{\pi^+} - m_p^{\pi^-}} \left(1 + \frac{F_2^n}{F_2^p}\right) - 1 \tag{2.40}$$

This technique relies on the inclusive structure function ratio F_2^n/F_2^p and for this analysis we have used the parameterization from NMC [42] that is implemented in the HERMES MC, as it describes the inclusive measurements well for HERMES kinematics. The extraction of this quantity from HERMES SIDIS data is an important verification of factorization and the fragmentation symmetries assumed above. It can also provide much needed input to guide future experimental proposals that require the flavor tagging technique to extract this and similar quantities.

2.4.2 Extraction of the Light Sea Asymmetry at HERMES

In 2003, HERMES released the first light quark sea asymmetry of the nucleon from SIDIS. Unpolarized data for pion yields from hydrogen (1.2×10^6 events) and deuterium (2.1×10^6 events) gas targets, in the kinematic range $0.02 < x < 0.3$ and $1 \text{ GeV}^2 < Q^2 < 10 \text{ GeV}^2$, were combined in a ratio that allows the extraction of $(\bar{d} - \bar{u})/(u - d)$. In addition to the x and Q^2 cuts, a $W^2 > 4.0 \text{ GeV}^2$ cut was made to ensure that these events are far away from the resonance region. Finally, an x-Feynman cut of $x_F > 0.25$ was made to ensure that the final state hadrons originated from the current-fragmentation region [6]. This method provides access to the sea distributions while minimizing detector effects which cancel in

the ratio $r(x, z)$ [6].

$$\rho^\pi = \frac{\sigma_p^{\pi^-} - \sigma_n^{\pi^-}}{\sigma_p^{\pi^+} - \sigma_n^{\pi^+}} \quad (2.41)$$

Assuming that factorization [40, 41] holds in the QPM, the total yield of hadrons h from a target t is proportional to the charge-weighted sum over all of the quark flavors of the parton distribution functions (PDFs) coupled to the fragmentation functions (Eq. 2.34) [6]. Using Eq. 2.37 we can again recast this quantity in terms of the hadron multiplicities and the ratio of inclusive structure functions.

$$\rho^\pi = \frac{2m_p^{\pi^-} - \left(1 + \frac{F_2^p}{F_2^n}\right) m_d^{\pi^-}}{2m_p^{\pi^+} - \left(1 + \frac{F_2^p}{F_2^n}\right) m_d^{\pi^+}} \quad (2.42)$$

Assuming iso-spin symmetry for the parton distribution functions $u_p(x) = d_n(x)$ and favored/dis-favored fragmentation (Eq. 2.28), the ratio of charged pion yield differences for the two targets can be recast in the following form [6]:

$$\frac{1 + \rho^\pi}{1 - \rho^\pi} = \frac{u(x) - d(x) + \bar{u}(x) - \bar{d}(x)}{u(x) - \bar{u}(x) - d(x) + \bar{d}(x)} J(z) \quad (2.43)$$

In this equation, $J(z) = 3(1 + \eta(z))/(5(1 - \eta(z)))$ is independent of x and is constructed from $\eta(z) = D_2(z)/D_1(z)$, the ratio of the dis-favored to favored fragmentation functions. Rearranging Eq. 2.43, we can find an expression for the ratio of light anti-quark sea to the light quark distributions. It is this expression that can be exploited to extract the light anti-quark sea asymmetry in the proton.

$$\frac{\bar{d}(x) - \bar{u}(x)}{u(x) - d(x)} = \frac{J(z) \left[1 - \rho^\pi\right] - \left[1 + \rho^\pi\right]}{J(z) \left[1 - \rho^\pi\right] + \left[1 + \rho^\pi\right]} \quad (2.44)$$

In the previous HERMES analysis, the fragmentation functions D_1, D_2 were extracted for each of the three targets, H, D and ^{3}He, separately, using the GRV 94 LO PDF set, and showed no statistically significant difference [6]. However, only $\eta(z)$ from the ^{3}He target was used in the analysis to remove statistical correlations with the pion ratios from H_2 and D_2 [6]. The final result is shown in Fig. 2.8 where the data is binned in five bins of x over the range $0.2 - 0.8$ in z.
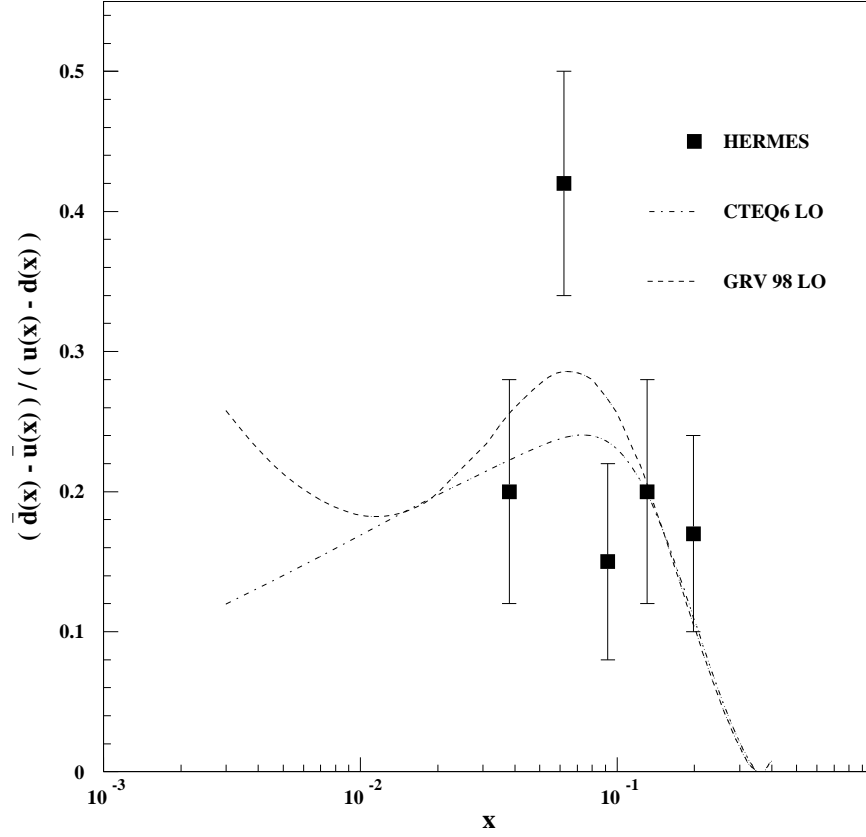
Figure 2.8: HERMES result for the light sea asymmetry $(\bar{d}(x) - \bar{u}(x))/(u(x) - d(x))$ as a function of x in the range $0.2 < z < 0.8$. Also shown is the more modern CTEQ6 [8] and GRV98 [9] parameterizations of this quantity.

The GSR result for the measured region at HERMES is given as $\int_{0.02}^{0.03}(\bar{d}(x) - \bar{u}(x))dx = 0.107 \pm 0.021(stat) \pm 0.017(syst)$ [6]. When the data is extrapolated to the unmeasured region, the total integral gives 0.16 ± 0.03, which is consistent with the E866 measurements [17].

2.5 Models

In the following sections, a summary of some of the theoretical origins and predictions for the light sea asymmetry is made. This is not meant to be an exhaustive account, but rather to give the reader a flavor for the types of models that have had some success predicting this phenomenon. For a more complete survey, see references [17] and [43].

2.5.1 Pauli Blocking

The influence of the Pauli blocking mechanism is simply that $u\bar{u}$ pair creation in the nucleon may be slightly inhibited due to the existence of two u quarks in the ground state. When the simple spin and color degrees of freedom are considered, we see that there are $(3 \otimes 2)$ six available ground states for both u and d quarks. In this simple counting model we would expect the asymmetry to be as large as $\bar{d}/\bar{u} = 5/4$. However, a problem arises with this model when the anti-symmetrization between quarks is considered. The u_v excess actually produces extra diagrams involving $u\bar{u}$ creation and can lead to a $\bar{u}$ over $\bar{d}$ excess, which is in disagreement with the data [17, 43, 44].

2.5.2 Meson Cloud and Chiral Models

Meson cloud models [45] are perhaps the easiest models to understand from a conceptual point of view. The proton is considered to be a bare proton dressed with a pion cloud. In this picture the proton can be constructed of $\Delta^{++}\pi^-$, $\Delta^+\pi^0$, $p\pi^0$, $n\pi^+$ and $\Delta^0\pi^0$ combinations. For DIS this is simplest to understand as a fluctuation of the proton into, for instance, a positively charged pion and a neutron and the subsequent interaction of the virtual photon with the pion. The sea asymmetry then arises from the π^+ dominance in the virtual combinations leading to an excess in the $\bar{d}(x)$ distribution as a result of the pion valence

distributions. Additionally, it has been demonstrated that in order to reproduce the light sea asymmetry data the meson-baryon Fock state must also contain contributions from the σ and ω [46].

Despite reproducing many aspects of the data, these calculations are subject to two flaws. First, the fractions of each meson coupling given above can be calculated from the πNN, $\pi N \Delta$ couplings and experimental form factors, but the result depends strongly on the cutoff chosen for the integral over the form factor. Second, the size of the symmetric sea is unknown and calculation can be massaged to match the experimental results [17, 43].

Chiral models also employ virtual pions, or Goldstone bosons, as their degrees of freedom in chiral perturbation theory. In these models, the pion is emitted by constituent quarks rather than the proton itself. What is of particular interest is that these EHQ (Eichten, Hinchliffe and Quigg) calculations produce a similar probability of finding a pion in the nucleus as the meson cloud models. These models are found to be lacking because the virtual pion is emitted by a quark, thus only allowing one parameter α which is constrained by experimental data and appears to be too small [17, 47, 48]. However, such models have found some success in calculating a light see asymmetry that agrees with the experimentally measured values, see [47] and references therein.

2.5.3 Lattice QCD

GSR calculations from lattice QCD (LQCD) are not available at this time. However, there seems to be a reasonable explanation for the asymmetry from non-perturbative QCD. The difference arises from connected versus disconnected insertion diagrams in a Euclidean path integral formalism. In these diagrams the loops represent gluons and the disconnected diagrams can produce any flavor of quark. However, the connected diagrams only produce up and down sea quarks. In this theory the asymmetry must come from the disconnected diagrams. One particularly good prediction of this is that the strange sea should be symmetric ($s = \bar{s}$), which data seems to support. Studying the effects of these so-called "cloud" anti-quarks, lattice QCD has found some indication of a light sea asymmetry, but, as of yet, has no explicit comparison with the GSR [17, 43].

Despite the lack of firm predictions in this arena made by LQCD, modern techniques and advances in the field hold some promise. The extrapolation to lighter quark masses with three mass flavors is necessary. This has motivated new techniques such as multi-bosonic algorithms which hope to overcome the limitations of the hybrid Monte Carlo algorithms [49, 50]. More recently the Symanzik-improved staggered-quark discretization allows unquenched lattice-QCD simulations with much smaller (and more realistic) quark masses than previously possible [51]. These advancements suggest that in the near future LQCD may be able to describe the sea structure of the proton.

Chapter 3

Experimental Apparatus

The HERMES experiment is located in the east experimental hall of the HERA accelerator. It is a forward geometry spectrometer that is top-bottom symmetric about the lepton beam pipe. The detector acceptance covers approximately ± 170 mrad in the horizontal (x) direction and ± 40-140 mrad in the vertical (y) direction which allows particles with scattering angles in the range 40-220 mrad to be detected [52]. The major features of the detector are its tracking system, the ability to separate leptons from hadrons and hadron flavor separation for pions, kaons and protons. In the following sections the major aspects of the HERA beam, HERMES target and spectrometer are discussed in detail.

3.1   The HERA Beam

The HERA storage ring provides the HERMES experiment with transversely polarized electrons (positrons) with a nominal energy of 27.5 GeV. The beam is self-polarizing via the emission of synchrotron radiation, a process known as the Solokov-Ternov effect [53], with a time dependent polarization given by:

$$P_B(t) = P_{max}(1 - e^{-t/\tau}) \tag{3.1}$$

Here, P_{max} is a theoretical maximum polarization which is equal to 92.4% for a perfectly flat storage ring where the magnetic field is perpendicular to the lepton orbit [53]. The characteristic time τ in the ideal case would only depend on the beam energy and the radius of curvature in the magnets giving $\tau =$36.5 min. In practice, the HERA storage ring routinely achieved a maximum polarization of 60% in 20-24 [54] minutes during HERAI and 50% in 30 minutes during HERAII after the luminosity upgrade.
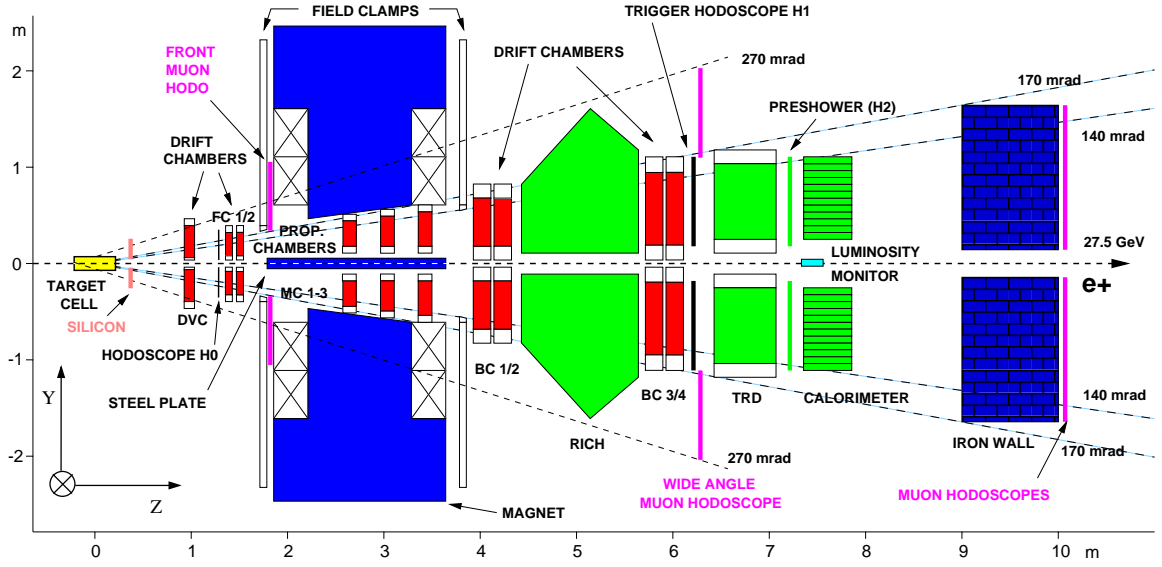
Figure 3.1: A two dimensional side view of the HERMES spectrometer. In the HERMES coordinate system, right is the positive z and up is the positive y direction
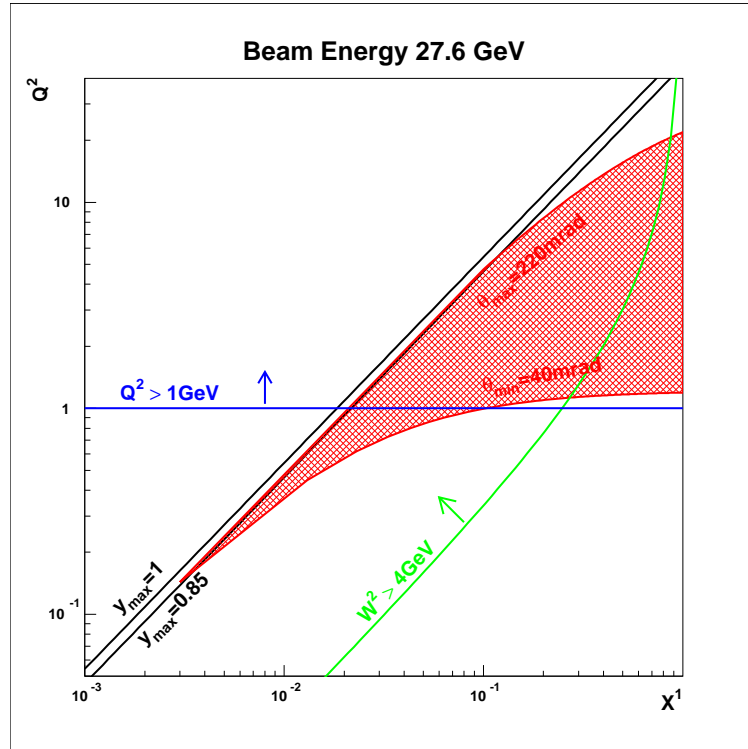
Figure 3.2: HERMES kinematic coverage in x and Q^2.

Spin rotators [55] before the experiment (spin rotator I) take the self-polarizing leptons and rotate them 90° to a longitudinal polarization and then back to transverse after the interaction region (spin rotator II). These rotators are the mini-rotator type proposed by Buon and Steffen [56], which consist of three interleaved vertical and horizontal bending magnets, and were designed for HERA to operate between beam energies from 27.5 to 35 GeV [55]. Over the course of the experiment, both longitudinal helicity states were provided by changing the field direction in the spin rotators. The lepton beam is optimized for collider operation, therefore the bunch structure consists of very short bunches with high peak currents [52]. The time structure allows for up to 200 bunches to be in the machine at one time. Each bunch has a full width half maximum (σ) length of 27ps and are separated by 96ns (10.4MHz).

3.1.1 HERMES Data Structure

The electron beam current degrades as a result of in-pipe gas interactions and inter-beam interactions, as well as interaction with the HERMES targets. Therefore, a typical fill will degrade from the injected current of approximately 40mA to something on the order of 14-16 mA in approximately eight hours. This unit of time is called a fill by the HERMES experiment. The data taken during a fill is broken up into smaller volumes called runs. Depending on the density of the target and current of the beam a run can take 10-30 minutes to record on disk and is approximately 500MB in size. The data written in each run are called events and correspond to reading out all the detector components when one or more of the trigger conditions is satisfied. In section 3.3 we discuss the main HERMES trigger in more detail. Slow control information such as pressure, temperature, voltages and thresholds for the different detector components follows its own data chain and is not added back into the detected information until the micro data summary tape (μDST) stage. The data path followed consists of three fundamental stages. First, raw data is written out in the 16-bit experimental physics input output (EPIO) [57] format which contains the actual detector responses and the triggers. Next, the HERMES decoder (HDC) is run over the EPIO format files to decode the data by translating the raw data (TDC, ADC) from the

EPIO files into position and energy entries in an aggregate datta model (ADAMO) [58] entity-relationship database using geometry and calibration information. Finally, in order to produce full tracks, the reconstruction code HRC [59] is run, which combines the decoded data from HDC and the slow control data stored in DAD [60] databases in order to create μDSTs. This is the final data format that is analyzed at HERMES, typically using the event-driven analysis framework HANNA [61].

3.1.2 Data Cops

Within HERMES there is a small but diligent group of individuals who attempts to ensure that the data quality is very high. This encompasses looking for high voltage trips in detectors, runs marked as bad in the electronic log book, particle identification failing and a variety of other situations which can affect analyses. This information is then encoded in a 31-bit hexadecimal burst-list, for each half of the detector, which analyzers can use to exclude bursts that do not meet the good data quality criteria. It is very convenient that the entire data set is delivered to the analyzer, as different analyses may require less severe data quality cuts and thus analyze larger statistical samples.

3.2 The HERMES Target

The HERMES target cell consists of two 75 μm thick pure aluminum sheets spot-welded together with an elliptical cross section shape of 21×8.9 mm^2 [62]. Gas is injected from above into the 400mm long elliptical cell that confines the target gas in a region around the lepton beam [52], increasing the areal target density by about two orders of magnitude from a free gas [62]. The entire apparatus is contained within a vacuum chamber that is pumped free of the gas atoms leaking from the ends of the target cell by high-speed differential pumps (Figure 3.3). Leptons enter the target region through the beam pipe which is aligned with the open end of the target cell. After interacting with the target gas, the lepton beam and the produced hadronic fragments within the spectrometer acceptance exit the target chamber through a thin 0.3 mm stainless steel exit window [62]. A fixed aperture collimator C2 is positioned upstream of the target to prevent synchrotron radiation
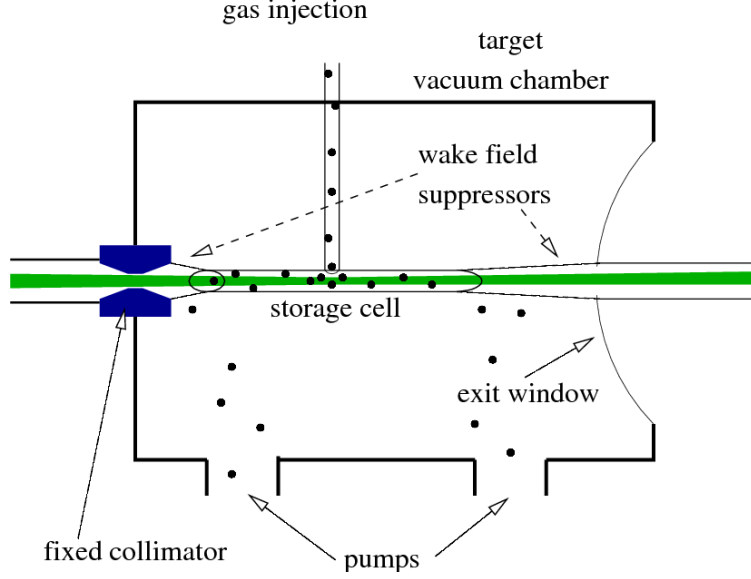
Figure 3.3: A schematic view of the HERMES target chamber where the lepton beam enters from the left and the scattered lepton and hadronic fragments are detected after exiting the thin window on the right. The fixed collimator depicted is referred to as C2 in the text.

produced in HERA before the HERMES interaction region from impinging directly on the target region as well as preventing the electron beam from striking the cell wall [52]. This collimator is itself protected from direct radiation from C1 which located two meters away and consists of two moveable collimators that are open during injection and closed during HERMES operation [62].

The HERMES target had two independent systems for delivering gas to the target cell. For polarized running between the years 1996 to 2005 the atomic beam source (ABS) was in place allowing the delivery of polarized hydrogen and deuterium to the target cell. For the years spanning 1997 to 2006 the unpolarized gas feed system (UGFS) was used for normal unpolarized running and for the high-density end-of-fill running. In the following sections, these two systems will be discussed in more detail.

3.2.1 ABS

The ABS is a Stern-Gerlok-based apparatus that can deliver atomically polarized hydrogen and deuterium beams to the target cell. The layout of the ABS is show in Figure 3.4.

In the ABS, hydrogen (H^2) and deuterium (D^2) molecules (H2) are disassociated by a radio frequency (RF) discharge of 13.56 MHz inside a Pyrex tube [63, 64]. The hydrogen atoms are then cooled into a 100K beam and passed through a skimmer and collimator, which remove remaining molecular hydrogen and focuses the beam. Next, the atoms pass through a sextupole magnet system in order to force the desired hyperfine population. This system consists of a total of five Hallbach [65] type segmented permanent magnets [62]. The electron spin is then transferred to the nucleon via weak field transition (WFT) and strong field transition (SF) radio transitions. These radio transitions exchange the occupation numbers of the hyperfine states $|1\rangle \leftrightarrow |3\rangle$ and $|2\rangle \leftrightarrow |4\rangle$ where the sates represent the spin projection of the electron (m_s) and the nucleon (m_N) (Eq. 3.2). By activating either one of the transitions, the orientation of the nucleon spin, with respect to the holding field, can on average, be reversed at 1.66×10^{-2}Hz. The degree of polarization of the atomic gas is measured by a Breit Rabbi Polarimeter (BRP) [66] which extracts a portion of the gas through a sampling tube on the opposite side of the target cell. With this system HERMES was able to inject 97% (88%) polarized atomic hydrogen (deuterium) into the target cell consistently over 10 years of operation.

$$|1\rangle = |m_s, m_N\rangle = \left|+\frac{1}{2}, +\frac{1}{2}\right\rangle \quad |2\rangle = \left|+\frac{1}{2}, -\frac{1}{2}\right\rangle \quad |3\rangle = \left|-\frac{1}{2}, -\frac{1}{2}\right\rangle \quad |4\rangle = \left|-\frac{1}{2}, +\frac{1}{2}\right\rangle$$

$$(3.2)$$

3.2.2 UGFS

The UGFS consisted of a set of gas bottles, connected to a dosing valve and a target inlet valve. Using this system, one could select from the available gasses (H, D, Ne, Kr, Xe) and also choose a dosing value setting allowing for a varied target thickness depending on the running state (normal or high density) or background conditions. HERMES was very fortunate to be allowed to use the internal gas target as a beam dump at the end of each HERA fill, which was known as high-density end-of-fill running (HDEOF) between 1997 and 2006. The target was increased to a thickness which shortened the lepton beam
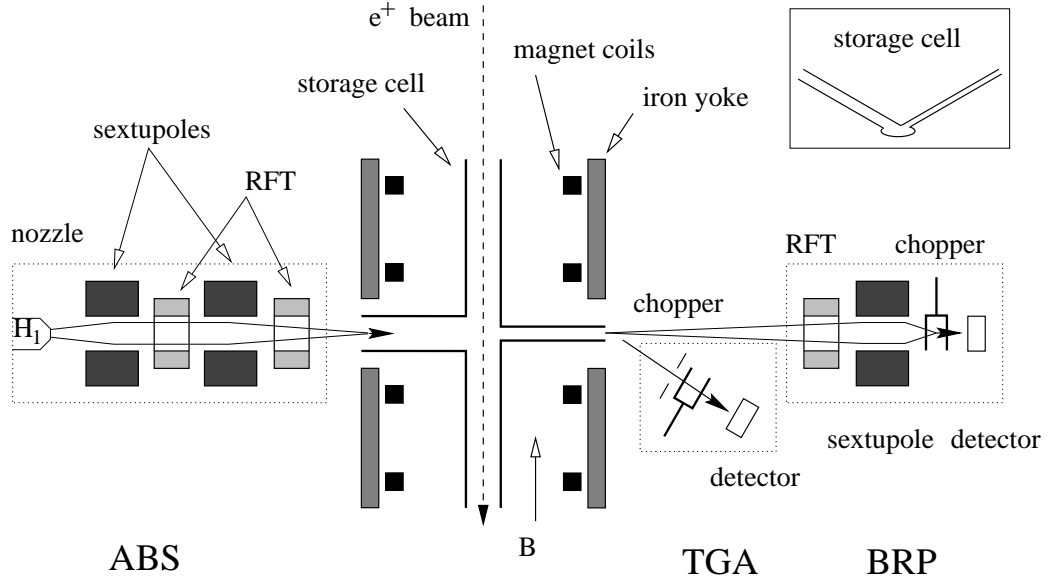
Figure 3.4: The schematic layout of the HERMES atomic beam source that was used to produce polarized hydrogen and deuterium for the target. In the center of the diagram is the HERMES target cell.

lifetime but did not saturate the dead time of the detector. This HDEOF running mode allowed HERMES to collect a large sample of unpolarized data on the available UGFS targets which in turn provided greater statistical leverage in unpolarized analyses. The typical target density for normal (high density) unpolarized running with hydrogen was 0.489×10^{15} nucl./cm^2 (0.313×10^{16} nucl./cm^2). For deuterium the values were typically 0.115×10^{16} nucl./cm^2 (0.594×10^{16} nucl./cm^2) [67].

3.3 Triggers

The HERMES data acquisition system is designed with certain triggers that when satisfied cause an event to be written to disk. These triggers are denoted by numbers within HERMES and consist of certain detector response requirements. During running, HERMES had the capability of defining 32 different triggers, of these 11 were typically physics triggers, the remainder were used for calibration and clock triggers. The main physics trigger for DIS is denoted trigger 21 and is satisfied if there is a hit registered in the trigger hodoscope H0 (upstream of the spectrometer magnet), the trigger hodoscope H1 (downstream of the

spectrometer magnet) and the calorimeter in the top or bottom of the detector. Physically, this trigger represents a charged track that registers in the calorimeter which is the typical experimental signature for the scattered lepton in a DIS event.

3.4 Tracking

The HERMES tracking system consists of the groups of wire chambers the front chambers (FCs) located in front of the spectrometer magnet, magnet chambers (MCs) within the spectrometer magnet and back chambers (BCs) located after the magnet. These detectors operate on the basic principle that high speed charged particles traversing the gas volume will knock off atomic electron thus ionizing the gas. The electrons and ions will then travel to the anode wires (electrons) and cathode plane (ions) of the chamber that are held at different voltages. While traversing the medium the electrons can knock out even more atomic electrons, creating an avalanche resulting in a large number of electrons arriving at the sense wire. In turn, this will cause a current in the sensor wires which can be measured at the readout electronics.

3.4.1 Front and Back Chambers

Both the FC and BC detector elements are conventional horizontal drift chambers which have the advantage of discerning the distance between the charged track and the anode wire using the electron drift velocity of the chamber gas. We begin our detailed discussion of the tracking system at the FCs which are situated upstream of the target magnet 1.53m and 1.68m from the target cell for FC1 and FC2 respectively. The two chambers have identical active areas of 660mm in the horizontal direction (x) and 160mm in the vertical direction (y) and have mirror images below the lepton beam pipe. Each chamber is filled with the gas mixture Ar(90%)/CO2(5%)/CF4(5%), which was chosen for its drift velocity (7cm/μs for E=800V/m) and non-flammable nature. The anode wires are held at ground potential and are 20μm thick W(Au). They are spaced 7mm apart, which defines the drift cell, giving a 3.5mm maximum drift length. Interspersed between anode wires are the potential wires which are made from Al(Au) and held at negative high voltage. The 6.4μm thick
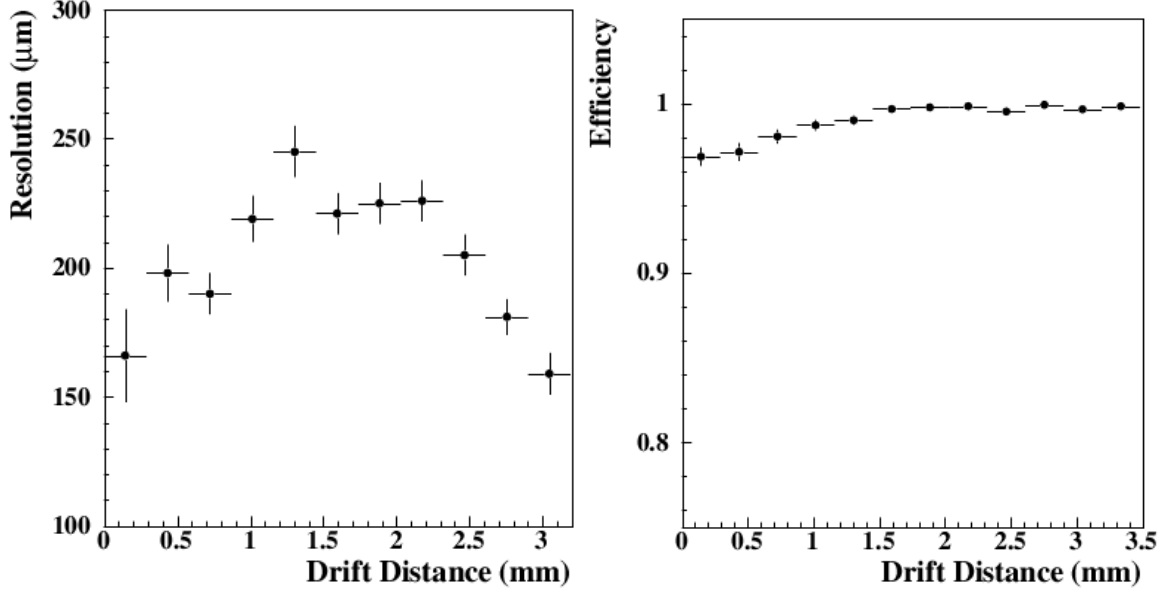
Figure 3.5: The resolution (left) and efficiency (right) of the front drift chambers (FC1-2) as a function of the drift distance.

cathode planes are made of aluminum on mylar and is separated from the wire plane by a 4mm gap. In each super-module there are two stereo planes in addition to the X plane and in each FC there are six modules for a total of six wire planes per chamber. The stereo planes U and V (U' and V') are oriented at $\pm 30^o$ to the X (X') plane which provides three space points per super-module (six space points total) and improves the resolution of the chamber. In the left panel of Figure 3.5 the resolution is shown to vary from 165-250μ as a function of the drift distance. The 2,304 channels (576 per module $\times$ two detector halves) are read out by an amplifier shaper discriminator (ASD) card mounted on board which sends emitter-coupled logic (ECL) signals to a LeCroy Multihit FastBus TDC in the electronic trailer [52].

The construction of the BCs is fundamentally very similar to the FCs. They are located downstream of the spectrometer magnet 4.033m and 5.8m for BC1 and BC2 respectively. An active area of 1.88m (2.890m) in the horizontal (x) and 0.520m (0.710m) in the vertical is covered by BC1(2). These chambers use the same gas and same anode wire material but have 127μm thick beryllium-copper potential wires and a25.4μm carbon on kapton cathode. The stereo angle layout is identical to the FCs and the drift cell is 15mm giving a resolution

per plane of $275(300)\mu$m for BC1(2) [52].

3.4.2 Magnet Chambers

The magnet chambers (MCs) are multi-wire proportional chambers (MWPC) located inside the spectrometer magnet at 2.725m (MC1), 3.047m (MC2) and 3.369m (MC3). By positioning the chambers inside a magnetic field, in this case $\int Bdl = 1.3$T, one can measure the bending radius of a charged particle and calculate its momentum. The MCs uses a different gas mixture, Ar(65%)/CO2(30%)/CF4(5%), from the other wire chambers which is optimized for MWPC operation. Each MC module consists of three stereo plane sub-modules (X, U, V), wherein there is an anode plane at ground potential and two cathode planes separated in the z-direction from the anodes by 4mm and held at negative high voltage, typically 2850V. The anode and cathode wires are constructed from the same materials as those used in the BCs. The centers of the submodules are 21mm apart and in sequential order the modules have active areas of 0.996×0.263m^2, 1.210×0.306m^2 and 1.424×0.347m^2.

3.4.3 Track Reconstruction HRC

The HERMES fast track reconstruction is based on the tree-search pattern recognition algorithm [68, 69]. The algorithm is based on a pattern database that contains all the possible tracks (126 million) for the each detector subsystem (FC, BC) and resolution [59]. The first step is to reconstruct the straight line front and back partial tracks independently in each of the X, U and V planes [70]. For each stereo plane, the algorithm begins by considering the entire plane and successively doubles the resolution by discarding the halves without a hit (Figure 3.6). This iterative search typically requires 10 to 11 steps to reach sufficient resolution find tracks. The front and back partial tracks are associated by matching pairs that intersect at the center of the magnet within a specified tolerance. The technique of forced bridging is used to force the front track to agree with the back track at the center of the magnet and the particle momentum is pulled from a lookup table (520k entries) using the front and back track parameters. Using an interpolation technique between the lattice point of the measured [71] spectrometer magnetic field a momentum resolution of less than
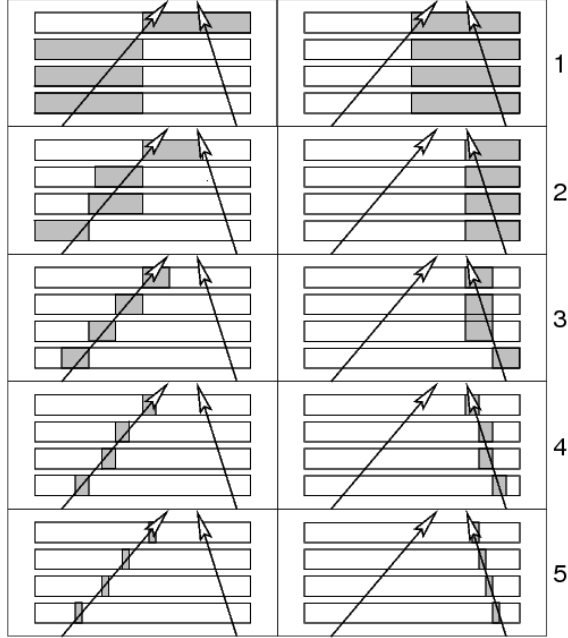
Figure 3.6: An example of the tree search algorithm for a tracking detector module. Vertically the panels represent the artificially reduced detector resolutions. The arrows are the possible tracks that are stored in the pattern database. In both cases the non physical track is rejected before the full detector resolution is exploited.

$\Delta p/p = 5 \times 10^{-3}$ can be achieved [70].

3.5 Particle Identification

3.5.1 Lepton Hadron Separation

In deep inelastic scattering it is crucial to identify candidates for the outgoing lepton in order to calculate the momentum transfer (and thus energy scale) of the virtual photon probe. For HERMES analyses, a Bayesian algorithm is used to separate these candidates from hadrons produced in the collision based on responses of the four particle identification (PID) detectors: an electro-magnetic lead glass calorimeter, two plastic scintillator hodoscopes (one of which is preceded by two radiation lengths of lead), a transition radiation detector (TRD) and a ring imaging Cerenkov detector (RICH) [52]. Each of these detectors will be described in slightly more detail in the following sections.

The quantity of interest for the PID algorithm is the probability $P(l(h)|E,p)$ that a

particle was a lepton (hadron) given the energy deposited, E, in a detector for a known track momentum, p. This quantity can be related through Bayes theorem [1] (Eq. 3.3) to the probability $P(E|l(h))$ that a lepton (hadron) with momentum p will deposit an energy E in a given detector, the probability $P(l(h)|p)$ that a track with momentum p is a lepton(hadron) and the probability $P(E|p)$ that a track with momentum p will deposit energy E in a given detector [70] [54].

$$P(l(h)|E,p) = \frac{P(l(h)|p) \ P(E|l(h),p)}{P(E|p)} \tag{3.3}$$

It is straightforward to see that the denominator $P(E|p)$ is just the sum over all the joint probability that the track was a lepton or hadron given the measured momentum and that a hadron or lepton with that momentum would deposit the measured energy (Eq. 3.4).

$$P(E|P) = \sum_{i=l,h} P(i|p) \ P(E|i,p) \tag{3.4}$$

The latter detector response distribution $P(E|l(h),p)$, termed the parent distribution, must be measured for each detector individually. These measurements could, for instance, be made at test beam facilities with appropriate lepton and hadron beams. However, for HERMES these parent distributions are extracted *in situ* by imposing cuts in the other PID detectors while excluding the detector under consideration. This is an iterative technique and has two major advantages over the test beam approach. First, the parent distributions are calculated for each year of data taking and thus take into effect aging and varying detector conditions [70] [54]. Secondly, the calibrations are extracted at the actual beam energy and hadron fluxes present in the data used in the analyses.

The remaining term $P(l(h)|p)$ is just the lepton (hadron) flux momentum distributions $\phi_{l(h)}(p)$ which are calculated by the iterative procedure described in [70] and [54]. The quantity PID' is formed for each detector by taking the base ten logarithm of the lepton probability over the hadron probability 3.5, such that negative PID' (Eq. 3.5) represents
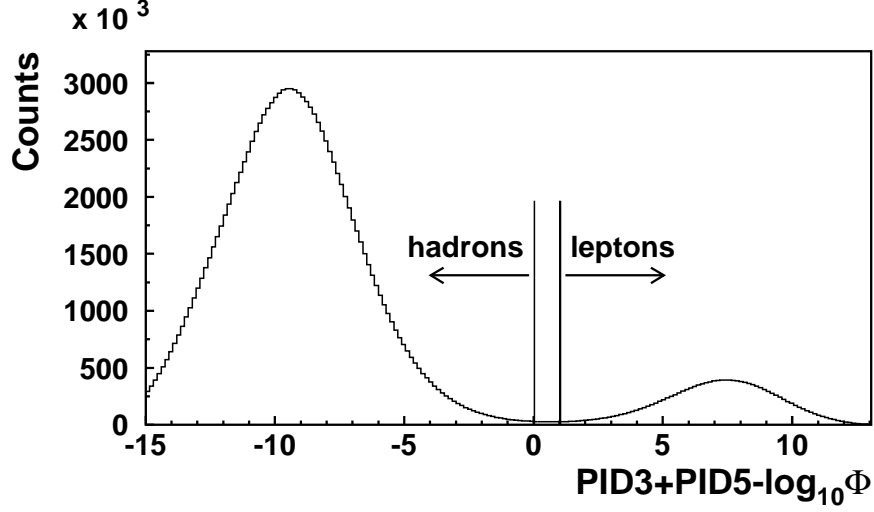
Figure 3.7: The PID3+PID5 - Φ distribution for a typical DIS data sample

larger hadron probability and positive PID' for higher hadron probability.

$$\text{PID'} = \log_{10} \frac{P(l|E,p)}{P(h|E,p)} = \text{PID} - \Phi \tag{3.5}$$

where in the right hand side of Eq. 3.5 the detector-independent ratio of hadron to lepton fluxes, $\Phi = \phi_h(p)/\phi_l(p)$, has been separated from the detector-dependant (via parent distributions) PID quantity. The individual detector PID values are combined into the quantities PID2, PID3 and PID5:

$$\text{PID2} \equiv \text{PID}_{cal} + \text{PID}_{pre}$$
$$\text{PID3} \equiv \text{PID}_{cal} + \text{PID}_{pre} + \text{PID}_{cer} \tag{3.6}$$
$$\text{PID5} \equiv \sum_{i=1}^{6} \text{PID}_{trd,i}$$

where the sum in PID5 is over the six TRD modules and the only difference between PID2 and PID3 is the inclusion of the ring imaging Cerenkov detector's response. For many analyses the equal probability situation, PID3+PID5=0, is used as the cut-off for lepton-hadron separation. Figure 3.7 shows the PID3+PID5 response for data used in this analysis.

Transition Radiation Detector

The TRD consists of six modules above and below the beam of dimension 325x75 cm^2. Each module contains the radiator and a Xe/Ch$_4$ (90:10) mixture-filled proportional chamber. The radiator is a 6.35cm thick pseudo-random matrix of polyethylene fibers with individual fiber diameters between 17 and 20μm (3.8). When a charged lepton traverses the radiator it produces transition X-rays as it moves across fiber gas interfaces. This radiation is detected in the proportional wire chamber after ionizing the chamber gas [52]. Each wire chamber has 256 vertical wires of 75 μm gold coated Be-Cu spaced 1.27cm apart and held at a bias voltage of 3100V. Each active detector volume is defined by the 50 μm thick mylar cathode foils along the edge of the detector.

The efficiency of the proportional chamber is dependant on the purity of the gas mixture. Due to the expense of Xe, the gas is recirculated and purified, using molecular sieves and activated copper, during detector operation [52]. The gas system is described in more detail here [72].

Both hadrons and leptons deposit energy in the TRD due to ionization of the chamber gas. The leptons however tend to deposit twice as much energy due to transition radiation and the relativistic rise in the dE/dx curve for the chamber gas. This allows for an excellent separation (i.e. unique parent distributions) for leptons and hadrons in the TRD.

Pre-shower Hodoscope

The pre-shower counter (H2) is located in front of the calorimeter. It is a plastic scintillator hodoscope that is preceded by an 11mm lead curtain which corresponds to approximately two radiation lengths for positrons. This lead causes light leptons to initiate a photon shower before entering the scintillator but not be absorbed. A large energy deposit in the photo tubes of the hodoscope from the shower is a strong indication that the track was a lepton. The difference in the response for positrons and hadrons can be seen in the left panel of Figure 3.9. In addition, the shower initiated in this detector often propagates back to the calorimeter.
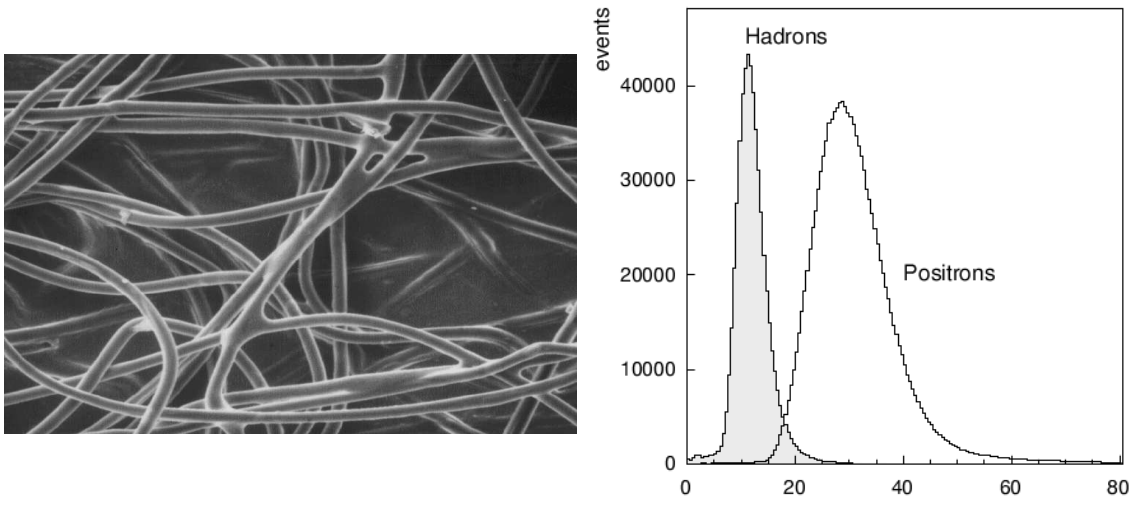
Figure 3.8: Microscopic image of the TRD radiator material (left). The momentum response of the TRD (right).
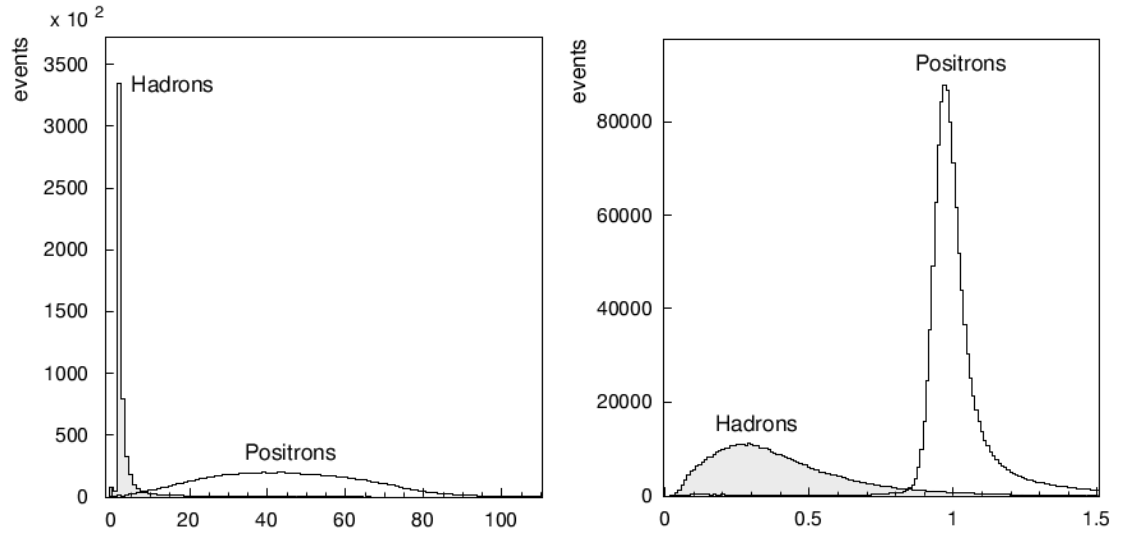
Figure 3.9: The energy responses of the pre-shower (left) and calorimeter (right) detectors for hadrons and leptons.

49

Calorimeter

The HERMES electromagnetic calorimeter consists of 840 radiation resistant F101 [52] lead-glass (LG) blocks arranged in two walls of 42×10 bricks above and below the lepton beam [73]. Each block measures 9×9×50 cm^3, such that the face of each calorimeter wall has a width of 378cm and a height of 90cm. The cross-section and length (18 radiation lengths) of the blocks was chosen such that 90% of the shower energy for a lepton injected perpendicular to the calorimeter face would remain in an individual block [73]. When the lepton enters the calorimeter it sees the strong magnetic field of the nucleus from the lead which causes it to change direction and emit a virtual photon [74]. For much heavier hadrons the probability of emitting such a photon is lower and they pass through the calorimeter only depositing a small portion of their energy unless they experience a nuclear collision. These two different signals are distinguishable (Figure 3.9) and the calorimeter coupled with the other lepton PID detectors provides a clean lepton signal with less than 1% hadron contamination. The scintillation light emitted is isolated within each block, due to a 50μm thick aluminized mylar foil wrapping and 125μm, and detected by a 7.5cm Phillips XP 3461 shielded PMT coupled to the LG block with silicon glue [73] [52]. To prevent radiation damage to the calorimeter caused by synchrotron light during injection and ramping of the HERA lepton beam both walls are only moved into the detector area after the collimators have been closed. The calorimeter movement apparatus is describe in more detail here [73] and here [52]. The calorimeter is also monitored for gain and ageing by a 500nm wavelength dye laser that sends light pulses to every PMT in the calorimeter as well as a reference photo-diode [52].

RICH

3.5.2 Hadron Flavor Separation

In order to distinguish between different hadron types HERMES installed a dual radiator ring imaging Cerenkov (RICH) detector in 1997. Prior to this HERMES used a threshold Cerenkov detector which could only differentiate pions from heavier hadrons. The detector utilizes the fact that particles traveling faster than the speed of light in a material $\beta c >$
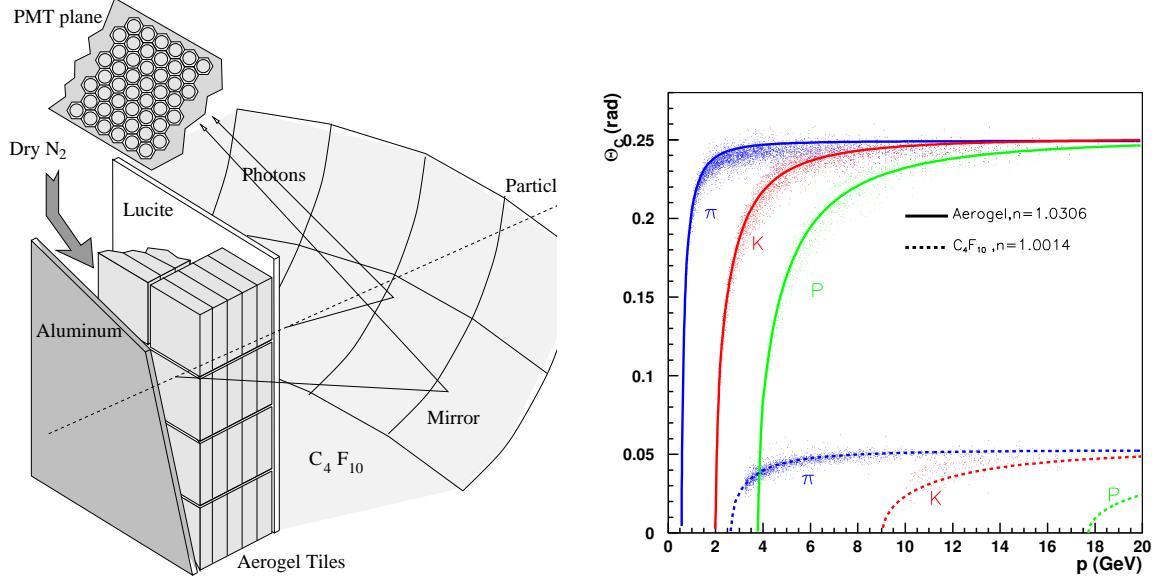
Figure 3.10: The HERMES RICH detector top geometry is schematically depicted in the diagram to the left. On the right, the Cerenkov angle (rad) versus hadron momentum (GeV) is shown for the theoretical prediction (solid and dashed lines) and the actual detector response from data is overlaid (points).

$c_n = c/n$, where n is the index of refraction, will produce a Cerenkov cone of light. This is essentially an electromagnetic shock-wave and is a result of the fact that the electromagnetic waves are forced to travel slower than the relativistic particle which causes the wave fronts to constructively interfere [75]. The opening angle, θ, of the cone is given by the relation:

$$\cos\theta = \frac{1}{n\beta} \tag{3.7}$$

The RICH was designed with two radiators, a set of aerogel tiles (n=1.0304) and a heavy fluorocarbon gas, C_4F_{10}, (n=1.00137) [76] such that each particle traversing the detector would produce two Cerenkov rings. The rings are recorded by imaging the Cerenkov cones off a mirror array onto 1,934 3/4-inch photo multiplier tubes (PMT) mounted above the detector in a soft steel frame, which provides shielding from the stray magnetic field of the main spectrometer magnet [76]. The top half of the RICH detector is depicted in Figure 3.10 and the bottom half is the symmetric mirror image mounted below the beam line.

When the momentum of the particle is known from the tracking system one can then decode the particle type via the angle. The Cerenkov opening angle versus momentum is

hadron	aerogel (GeV)	C_4F_{10} (GeV)
π	0.6	2.7
K	2.0	9.4
p	3.8	17.9

Table 3.1: The minimum momentum required for each hadron to produce a Cerenkov cone in the aerogel or gas portion of the RICH detector.

plotted in Figure 3.10 and the thresholds for Cerenkov cone production in both materials are given in Table 3.1. Below the threshold for the material a hadron will not produce a ring in the detector. The advantage of having two radiators is a greater momentum range of hadron separation. For instance, above hadron momentums of 12GeV the aerogel radiator rings for pions and kaons begin to be degenerate, however in just this region the gas rings are still well differentiated. This novel scheme allows excellent hadron separation in the momentum range 2 - 15 GeV which contains 95% of all the hadrons in the acceptance of the spectrometer [76].

In the case of HERMES there are two different algorithms used to decide the hadron type: indirect ray tracing (IRT) and direct ray tracing (DRT). The face of the PMT matrix is not located at the focal point of the mirror array, thus the detected "rings" are in general asymmetrically distorted ellipses. This makes a ring pattern matching algorithm unfeasible for accurate reconstruction of the Cerenkov angle. In this case one can geometrically calculate the angle that a photon would have to be emitted to fire a given PMT using the known track parameters and mirror geometry. The general problem can be described in terms of the geometry depicted in Figure 3.11.

Here, E is the likely emission point, D is the location of the detected photon and C represents the center of the spherical mirror which allows one to find the point S where the photon scattered [76]. The likelihood method compares the average $\langle \theta \rangle$ of the reconstructed angles to the theoretical Gaussian with a width that corresponds to the single photon resolution and is centered at the angle which a pion, kaon or proton, given the momentum which is known from the tracking system, would produce [77]. This reconstructed angle averaging is limited to a window within $\pm 2\sigma_\gamma$ of the theoretical Cerenkov angle in order to reduce dilution from background hits and hits from other tracks [77].
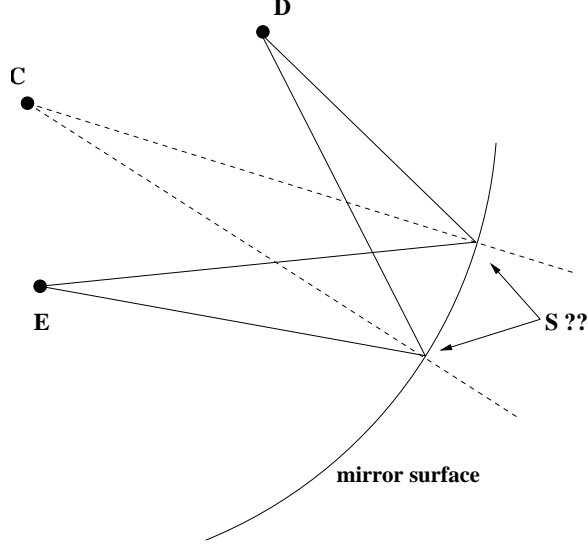
Figure 3.11: Geometric diagram of the inverse ray tracing problem

The DRT method is another approach to the same problem [78]. In this case, the hit probability for each PMT is calculated from the information about the track in the rest of the detector given a particular particle-type hypothesis. Comparing these calculated hit probability distributions with the actual observed distribution results in a probability that the particle hypothesis for the given track is correct. The bottleneck in this approach is the exorbitant number of simulations that must be run to produce the different hit patterns for different particle hypothesis. As an example, the direct approach requires simulating and tracing approximately 200 photons for a gas ring and 400 photons for an aerogel ring to accurately determine the hit probability for each PMT. It is obvious that this large CPU overhead makes the rather straight-forward DRT method less desirable than the IRT method during reconstruction.

In practice, both methods are used in the HERMES reconstruction and a table entry is set that points to the "best" result—that is the result that the RICH group considers to be the best of the computed methods. Typically in analysis, however, analyzers restrict themselves to the IRT method in order to use the collaboration-wide PID mis-identification efficiency correction matrix (P) that has been developed. For each of these methods the resulting hadron flavor hypothesis is accompanied by a quality parameter (rQP). This quality

parameter is used to determine how well the RICH was able to determine the particle type and is defined by:

$$\texttt{rQP} \equiv \frac{Prob^1}{Prob^2} \qquad (3.8)$$

Chapter 4

Data Analysis

In this section we report the data quality cuts and kinematic cuts made for the data. We also report the corrections applied to the data as well as the successful independent cross check of the analysis. The section concludes with the measured and extracted quantities of this analysis.

4.1 Data Quality and Gas Selection

The data quality mask `0x427E13DC` was used for both the bottom and top half of the detector for all targets and all years. Each bursts data quality entry is tested against this burst mask and rejected if any of the bits in the mask are set. This bit pattern requires that the HERMES detector, HERA accelerator and HERMES data acquisition system (DAQ) are all operating normally during the burst but makes no cut on the beam or target polarization. In particular for the detector we require the RICH, TRD, H2, luminosity monitor, FCs and BCs to be functioning and have no high voltage trips (or dead blocks where applicable) during the burst. The mask also excludes the first burst of a run, bursts that are marked as bad, missing PID or not analyzable in the log book, and those that have unreasonable dead time or burst length ($< 2s$ or > 11s). Finally we also require that HERA is delivering a reasonable beam current ($20 - 80$mA).

The definition of gas and polarization is controlled by the gas target type and the experimental mode is recorded in the slow control DAD database during the data taking and transfered to the μDST during the reconstruction. The definitions for polarized and unpolarized targets used throughout this document refer to the mode of target running when the data was recorded. The unpolarized modes were selected when the calorimeter

	H	$H_{pol.}$	D	$D_{pol.}$
98d0	10.60	N/A	36.64	28.06
99c0	0.30	N/A	6.30	40.25
00d0	127.43	N/A	36.64	163.04
02c0	9.63	14.74	8.81	N/A
03c0	1.36	8.66	N/A	N/A
04c0	N/A	31.32	24.54	N/A
05c0	5.51	121.10	146.42	N/A
Sum	330.65		490.70	

Table 4.1:   The total luminosity (pb^{-}1) categorized by target type and the data taking mode of the target. Where the sum is no longer separated by by polarization.

threshold was set to 3.5GeV in two adjacent columns, the target magnet was off and the values of the DST entries `g1Unpol.iGasType` and `g1Quality.iExpTarg` were set to 1(2) for hydrogen (deuterium). The polarized sample from each year contained all data where the target was in one of the ABS modes and the calorimeter threshold was set to 1.4GeV.

In Table 4.1 the luminosity measured using this burst mask is presented for all years and targets.

4.2   Kinematic Cuts

The kinematic and geometric cuts listed in Table 4.2 and 4.3 were applied to the data. In order to accept an event as SIDIS we first required that the kinematics of the scattered lepton were such that the virtual photon could resolve the partonic structure of the nucleon ($Q^2 > 1.0\text{GeV}^2$) and that the nucleon was broken apart in the final state ($W^2 > 10\text{GeV}^2$), i.e. that we avoid the resonance region. In addition to the kinematics, we required that the scattered lepton originated from the target cell and was within the standard fiducial volume cuts of the calorimeter. These geometric cuts minimize the likelihood that the electron has re-scattered from the frame of a detector element and ensure that the entire EM cluster can be contained in the calorimeter.

For the final state hadron we measured the energy fraction z in the range 0.2 to 0.8, while requiring the hadron to have momentum between 2 and 15 GeV/c to ensure proper hadron identification with the RICH. The forward z vertex cut was not enforced for the

Event Level Cuts	Track Level Cuts
$Q^2 > 1.0$ GeV^2	$0.8 > z > 0.2$
$W^2 > 10.0$ GeV^2	
$0.85 > y > 0.1$	$15 > p_h > 2$ GeV/c
$|z_{vert}| < 18cm$	$100 > z_{vert} > -18$cm
$|d_{vert}| < 0.75cm$	

Table 4.2: Kinematic cuts for yields from data

Lepton Cuts	Hadronic Cuts
$|caloX| <= 175.0$ cm	$|caloX| <= 175.0$ cm
$108.0 \geq |caloY| \geq 30.0$ cm	$108.0 \geq |caloY| \geq 30.0$ cm

Table 4.3: Fiducial calorimeter cuts for yields from data.

hadrons measured in this analysis so the probability of decaying particles (such as Λs) being included in the sample is large.

The final number of DIS events recorded after applying data quality, geometric and kinematic cuts are listed in Table 4.4.

4.3 Data corrections

4.3.1 Transverse Target Magnet Correction

In 2002, 2003, 2004 and 2005 the polarized data was taken with a transverse magnetic holding field. This caused a $\vec{v} \times \vec{B}$ bending of the charged particle tracks that passed through the field. In order to correct for this bending two different corrections were applied. The two methods are referred to as 1(2) and were created by W. Augustyniak and S. Yen [79].

	H	H$_{pol.}$	D	D$_{pol.}$
98d0	0.4964	N/A	0.9105	0.9945
99c0	0.0115	N/A	0.2174	1.3693
00d0	5.0967	N/A	1.3154	5.8244
02c0	0.3742	0.5469	0.3024	N/A
03c0	0.0394	0.3392	N/A	N/A
04c0	N/A	1.2394	0.8177	N/A
05c0	0.2174	4.1683	4.8374	N/A
Sum	12.5290		16.5890	

Table 4.4: The total DIS statistics (millions) after kinematic cuts categorized by year, target and polarization.

For the years 2002-2004 correction 1 is applied in 2005 only correction 2 is applied. In all cases a failure of the algorithm to correct for the magnet (i.e. -999 in the corrected value table entry) is not recorded for the analysis.

4.3.2 RICH Unfolding

In order to account for the identification efficiency of the ring imaging Cerenkov detector (RICH) a weighted unfolding technique is used. The weights are determined from a Monte Carlo simulation of the detector and depend on the momentum, topology and the determined particle type. The actual hadron yield detected ($\vec{I}$) is related to the true yields via the so called "P" matrix:

$$\vec{I} = P\vec{T} \tag{4.1}$$

In this case, P is a 3×4 matrix which takes into account not only the misidentification of known particles types, i.e. kaons being detected as pions, but also any other hadron "X" that is misidentified. To correct measured data we truncate the P-matrix to remove he unidentified X track row, as we do not record these unidentified tracks in the data. A demonstrative example of the truncated P-matrix (X row removed) for one track per detector half is shown in Fig. 4.1.

In order to apply the reverse transform as a weight in the data we must first truncate the P-matrix and then invert it. Event by event we can sum these weights to find our true hadronic yields.

$$N^h_{Tot} = \Sigma^{N_{DIS}}_{i=0} n^h_i = \sum_i \sum_{\alpha=\pi,K,p} (P^{-1})^h_\alpha n^\alpha \tag{4.2}$$

Then event by event each hadron identified contributes a weight corresponding to the inverse P matrix entry for each of the three possible hadron flavors.
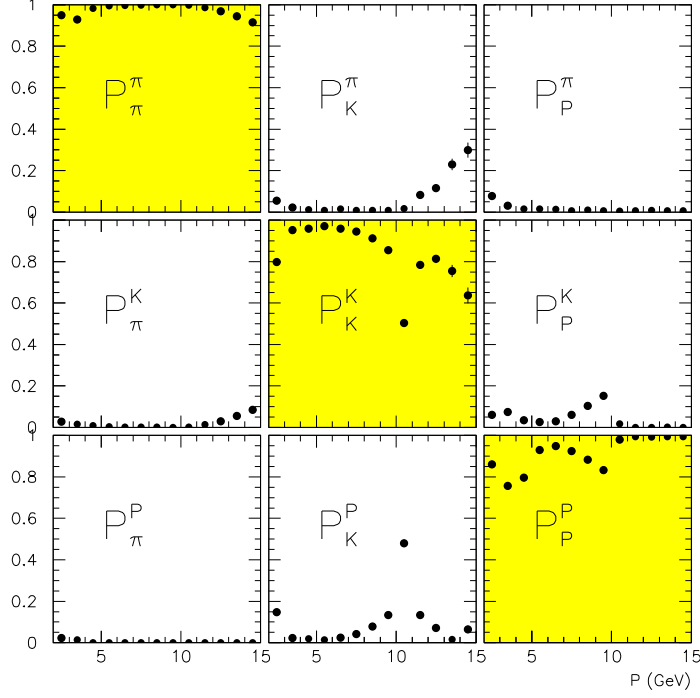
Figure 4.1: HERMES RICH P-Matrix for one track per detector half from the IRT method. The diagonal elements represent the efficiency for identifying a particle correctly.

RICH unfolding systematic error

The RICH unfolding attempts to correct for the inefficiency the RICH exhibits when determining different hadron flavors. This correction naturally depends on the method used to determine this inefficiency. Three different methods, the e-tune (which results from multidimensional tuning of the RICH MC to fit operating parameters), the h-tune (from experimental decay particle data) and the c-tune have been used to determine the P-matrices for the RICH. The c-tune provides a midway point between the other two tunes and is taken as the central value in this analysis. Using the maximum deviation of the e-tune and h-tune from the c-tune one can assign a systematic error due to the RICH unfolding.

$$\sigma_{RICH}^h = \text{MAX}\left(\left|N_c^h - N_e^h\right| ; \left|N_c^h - N_h^h\right|\right) \tag{4.3}$$

In this analysis we only assign this systematic error after the radiative unfolding has been applied to the corrected multiplicities for all three RICH tunes.

4.3.3 Charge Symmetric Background

It is also possible to misidentify a DIS event when there is a non-DIS lepton with high energy in the calorimeter. This can come from, for instance, pair production of photons and π^0 decays. Both of these production mechanisms have the advantage that they give the same number of correct sign leptons as wrong sign leptons (opposite sign from beam). The correction technique applied to the data gives a weight of $c_i = -1$ to any wrong sign lepton events. This modifies the RICH unfolding expression above slightly:

$$N_{Tot}^h = \Sigma_{i=0}^{N_{DIS}} c_i n_i^h \tag{4.4}$$

The statistical error after the RICH and charge symmetric background correction is given by the normal standard deviation for the sum of weighted measurements [1].

$$\delta^2 N_{Tot}^h = \sum_i (c_i n_i^h)^2 = \sum_i \left(c_i \sum_{\alpha=\pi,K,p} (P^-1)_\alpha^h n^\alpha \right)^2 \tag{4.5}$$

4.3.4 VMD correction

The virtual photon can fluctuate into a vector meson (VMD) which has the same quantum numbers (ρ^0, ϕ) before interacting with the target. The diffractive interaction of such a state with the target nucleon can produce a final state pion in the DIS kinematic regime. The major contribution to the pion sample is from elastic rho scattering from the proton which produces a pair of pions in the final state:

$$ep \rightarrow e\rho^0 p \rightarrow e2\pi p \tag{4.6}$$

In order to correct for this background we use the PYTHIA [80] MC generator which describes the HERMES data well and includes single and double diffractive VMD interactions. Using the process code from the MC, pions within the analysis cuts can be tagged as VMD or normal DIS products. The ratio of VMD pions to total pions (Fig. 4.2) in the final state gives the factor (ϵ_{VMD}) that can be used to correct the resulting pion yields for
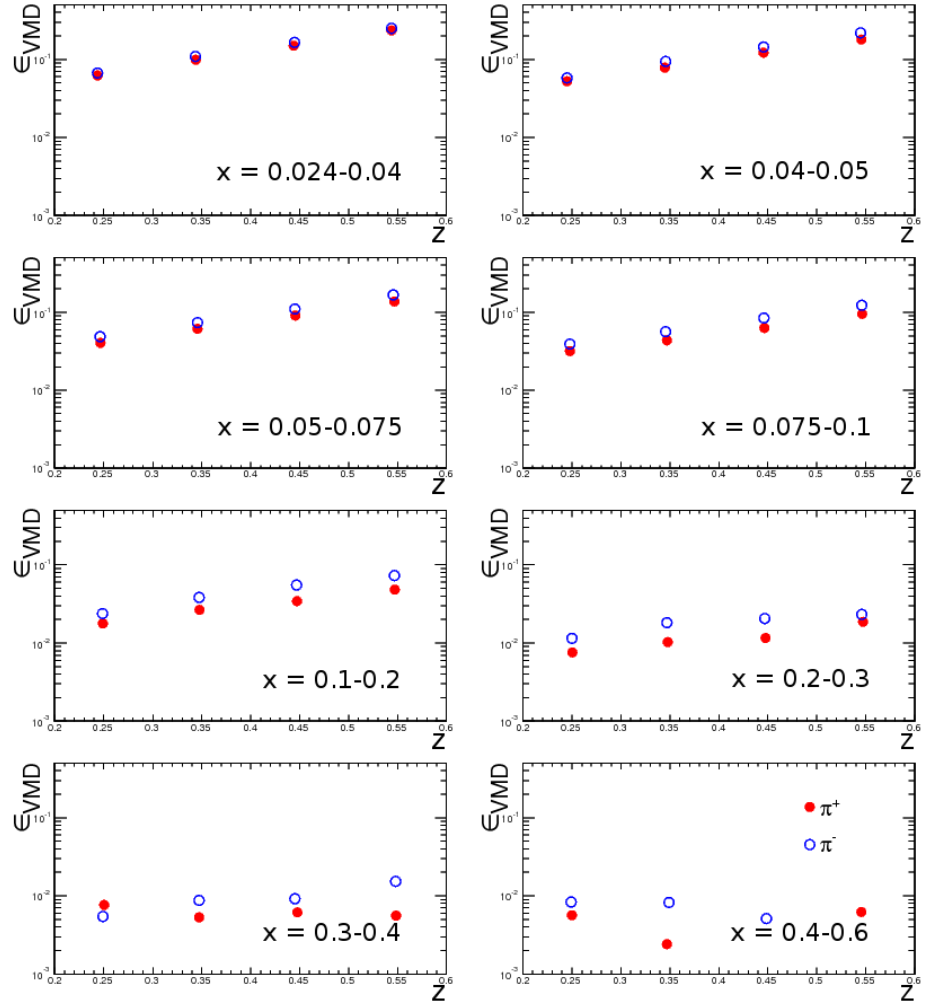
Figure 4.2: VMD fractions calculated for proton target using the PYTHIA MC simulation as a function of z in the different x bins.

this background.

$$N_{DIS}^h = (1 - \epsilon_{VMD})N_{Tot}^h \tag{4.7}$$

The quantities N_{VMD}^h and N_{DIS}^h are taken to be statistically independent quantities. With this assumption the error on the SIDIS yield after correcting for VMD pions is:

$$\delta^2 N_{DIS}^h = (1 + \epsilon_{VMD}^2)\delta^2 N_{Tot}^h + N_{Tot}^h \delta^2 \epsilon_{VMD} \tag{4.8}$$

from which it is obvious that this correction again causes the statistical error to inflate. It is also important to note that due to the event weight in PYTHIA always being equal to unity, the error on any PYTHIA count rate is equal to the square root of the number of counts.

4.3.5 Radiative and Acceptance Correction

In order to correct for QED initial and final state radiation (ISR and FSR) as well as smearing caused by the detector itself we apply a correction. This correction is made using two Monte Carlo (MC) simulations. In one case we use a MC chain consisting of: LEPTO [81] for the hard interaction; JETSET [38] to simulate the fragmentation process; HERMES smearing generator (HSG) [82] to simulate the detector volumes and acceptance; and RADGEN [83] to simulate ISR and FSR QED effects. The second MC is produced at the so called Born level. In this case, radiative and detector effects are turned off and the acceptance is also allowed to be the complete geometric volume allowed by the kinematic cuts made in the analysis. This technique is based on the HERMES internal note [84] by A. Miller. In the following subsections the construction of the smearing matrix and its application is discussed in further detail.

Unfolding Formalism

This technique attempts to unfold the bin migration caused by smearing of the kinematics. The technique requires two different physical process that are both subject to the same

un-simulated detector efficiencies (k). In this case the measured yield for each process can be described by:

$$X_{1(2)}(\alpha_t) = L_{1(2)}k(\alpha_t) \sum_{\alpha_b=0}^{N} S_{1(2)}(\alpha_t, \alpha_b)B_{1(2)}(\alpha_b) \qquad \alpha_t = 1...N \qquad (4.9)$$

Here, L represents the luminosity for each of the processes, X is the measured rate for each of the processes and B is the Born level rate which we would like to find. The smearing matrix is a non-square matrix that describes the inter-migration of either process between the kinematic bins. The extra dimension in the Born index, or "zero" bin, represents background that has been smeared into the geometric acceptance and kinematic cuts of the analysis. This matrix can be constructed from two MC productions (described in following section). In order to invert this equation to solve for B_2 we begin by first solving for and substituting k into the previous equations:

$$\sum_{\alpha_b=1}^{N} S_2'(\alpha_t, \alpha_b)B_2(\alpha_b) = \frac{X_2}{X_1} \sum_{\alpha_b=0}^{N} S_1(\alpha_t, \alpha_b)B_1(\alpha_b) - S_2(\alpha_t, 0)B_2(0) \qquad (4.10)$$

In this particular case our two processes, semi-inclusive DIS and inclusive DIS, are subject to the same luminosity measurement, therefore the pre-factors L_1 and L_2 naturally cancel. We also recognize that the quantity $\sum_{\alpha_b=0}^{N} S_1(\alpha_t, \alpha_b)B_1(\alpha_b)$ is merely the number of events of type 1 that appear in bin α_t of the "tracked" MC sample. Here, we have also separated out the zero bin background entry of S_2 leaving us with a truncated square matrix S_2'. In the case that this matrix is invertible we can solve directly for B_2:

$$B_2(\alpha_b) = \sum_{\alpha_t=1}^{N} [S_2']^{-1}(\alpha_b, \alpha_t)\frac{X_2(\alpha_t)n^1(\alpha_t)}{X_2(\alpha_t)} - n_0^2(\alpha_t) \qquad (4.11)$$

In our particular case we are using SIDIS and DIS to unfold the radiative effects and extract the Born level cross section. This requires us to take one last step of normalizing the Born level MC to the effective MC luminosity ($IEVGEN_b$) giving:

$$\sigma_b(\alpha_b) = \frac{B_2}{IEVGEN_b} = \sum_{\alpha_t=1}^{N} [S_h']^{-1}(\alpha_b, \alpha_t)\frac{X_h(\alpha_t)n^d(\alpha_t)}{X_d(\alpha_t)} - n_0^h(\alpha_t) \qquad (4.12)$$

	1	2	3	4	5	6	7	8	9
x	0.023	0.04	0.055	0.075	0.1	0.2	0.3	0.4	0.6
z	0.2	0.35	0.45	0.6	0.80				

Table 4.5: x and z bin edges used in this analysis.

Here, we have inserted SIDIS (h) and DIS (d) for the two processes as they will be used in this analysis and the subscript b is used for all Born level quantities. In addition, the special subscript 0 is used to represent hadrons from the MC sample that arrive in the kinematic bin α_t but originated in the zero bin.

Constructing Smearing Matrices

The hadronic smearing matrix is constructed from two Monte Carlo productions. The first includes the detector and radiative effects. The second is a Born level MC that uses the momentum lookup table to calculate the bending of a track in the spectrometer's magnetic field when the detector simulation is not present. The normalized ratio of the migration matrix ($n^h(\alpha_b, \alpha_t)$) and the Born level sums ($n_b^h(\alpha_b)$) gives the smearing matrix:

$$S(\alpha_b, \alpha_t) = \frac{n^h(\alpha_b, \alpha_t)}{n_b^h(\alpha_b)} \tag{4.13}$$

This migration matrix represents the kinematic migration of a track in hybrid binning space where $\alpha_{t,b} \equiv x_{t,b} * N_z + z_{t,b}$. In addition, the migration matrix contains a zero bin that is used to describe tracks that end up within our acceptance (kinematic and geometric) that were smeared in from outside the acceptance.

The migration matrix is normalized by the number of hadrons ($n_b^h(\alpha_b)$) observed in each bin that come from a Born level MC where no detector acceptance is enforced through tracking or geometric cuts. It is essential that the numerator and denominator of this ratio are normalized to the $IEVGEN$ of each MC sample so that differences due to generated MC sample sizes do not arise.

Fig. 4.3 charts the logic used to assign a hadron count to a specific migration matrix bin. The $x - z$ binning used in this analysis is given in Table 4.5.
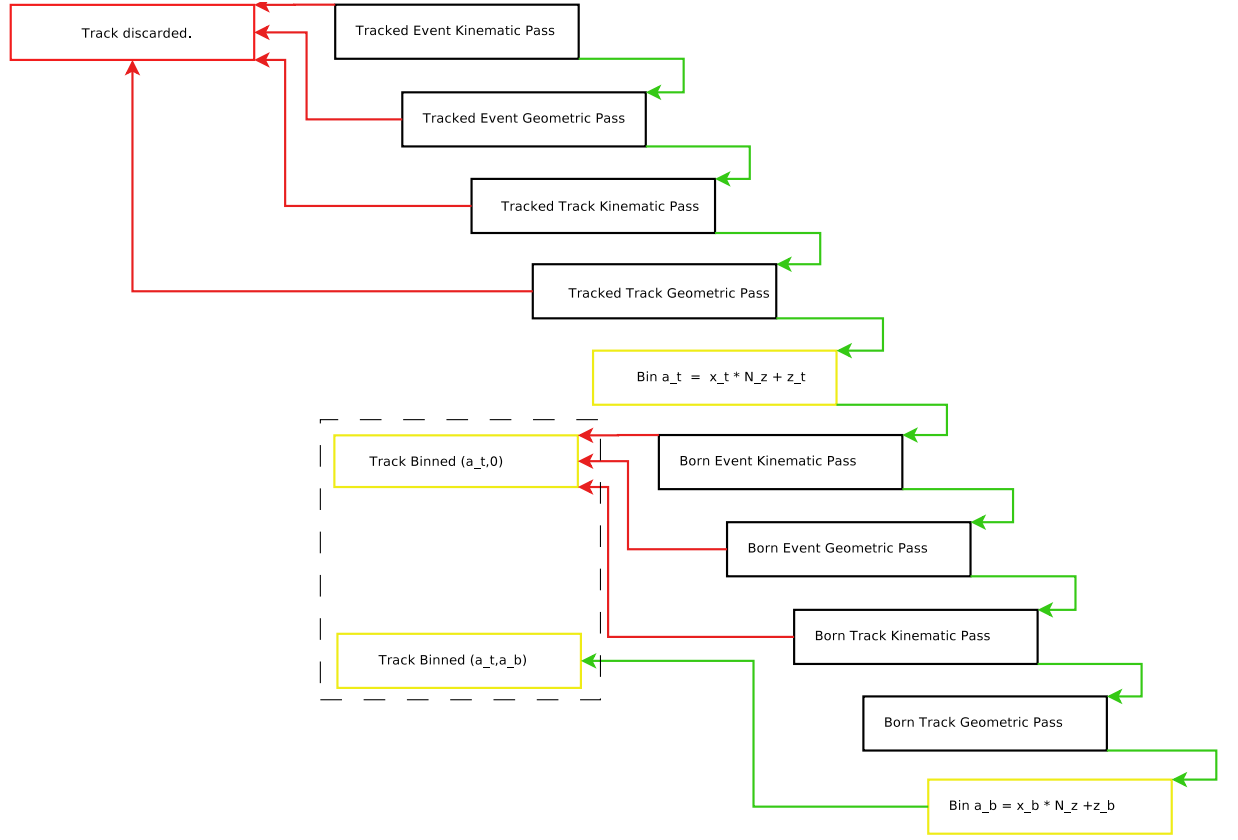
Figure 4.3: Logic flow chart for migration matrix $(n^h(\alpha_b, \alpha_t))$.

Migration matrix $n^h(\alpha_b, \alpha_t)$ cuts

For the tracked kinematics the cuts listed in Table 4.2 are made. Then the Born level (un-smeared MC table) kinematics for the same track are recorded to determine from which true bin the track migrated.

In addition to the kinematic cuts, we are using a tracked Monte Carlo so the track must be measured by the detector. While this places a certain geometric (and kinematic acceptance) on the tracks we also use a set of typical HERMES calorimeter fiducial cuts (the technique is used in order to mirror what we are correcting, which is real data). For all MC the *rcOffset.c* code is used to calculate the offset and slope change that a track suffers when it passes through the spectrometer magnet which allows us (even in non-tracked MC) to calculate the x and y positions of the hadron/electron on the calorimeter. The cuts required are shown in Table 4.3. It should also be noted that we generate the electron and tracks with the minimum generation level cuts so that particles are generated outside of the geometrical/kinematic acceptance and can smear into it. In the MC simulation the position of the track on the face of the calorimeter must be calculated according to:

$$caloX \equiv rXposMC + (rXslopeMC * 463.0) \tag{4.14}$$

$$caloY \equiv rYposMC + (rYslopeMC * 463.0)$$

where $rX(Y)posMC$ and $rX(Y)slopeMC$ are the $x(y)$ position and slope of the track after it has been stepped through the magnetic field map.

Smearing matrix denominator $n_b^h(\alpha_b)$

The basic difference in the cuts enforced for the Born level denominator is that all of the geometric cuts have been removed. In this way we can also unfold the data to a full kinematic acceptance distribution.
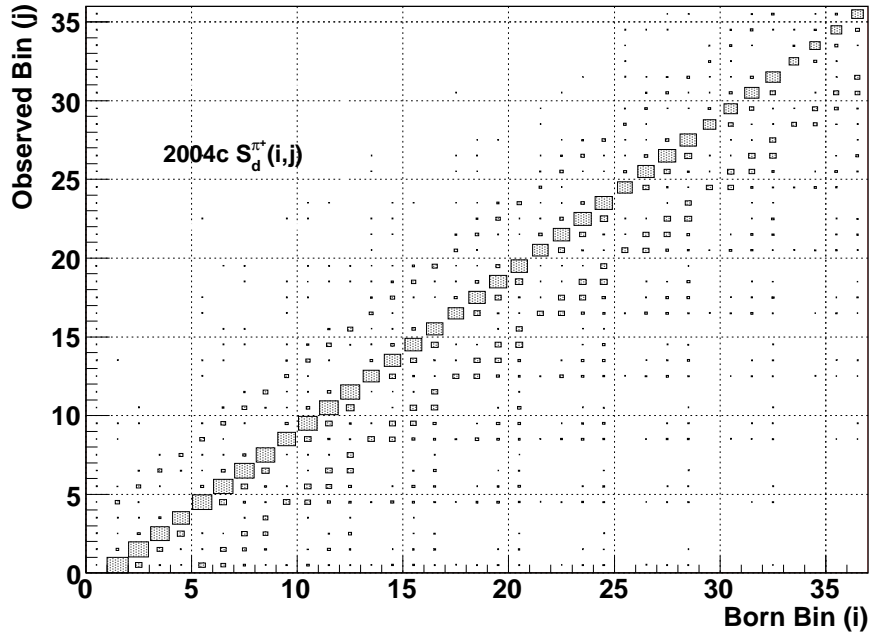
Figure 4.4: Smearing matrices for positive pions from deuteron target, the area of the boxes represent the number of pions smeared between the bins.

Born level zero bin

The zeroe bin is for events that ended up passing the kinematic cuts required for the tracked MC but at the Born level were not inside these cuts. For example, in the migration matrix case this will be any track that passes our cuts but whose Born level kinematic/geometric values do not pass. The cut tracks will be placed in $n^h(0, \alpha_t)$. For the Born denominator this will only be tracks that fail the kinematic cuts because we are using the smearing matrix to unfold the geometric acceptance as well.

Smearing matrix results

Error inflation

The unfolding technique also causes an inflation of the error on the resulting quantity. It is the result of shuffling counts between bins, which thus dilutes knowledge of the true values even further. It can be calculated, for the cross section, by neglecting the error on the MC

sample:

$$\delta\sigma_b^2(\alpha_b) = \sum_{\alpha_t=1}^{N} D_h^2(\alpha_t, \alpha_b) \frac{(X_d(\alpha_t)\delta X_h(\alpha_t))^2 + (X_h(\alpha_t)\delta X_d(\alpha_t))^2}{X_d(\alpha_t)^4} \qquad (4.15)$$

where D is traditionally called the radiative dilution matrix and is defined by:

$$D_h(\alpha_t, \alpha_b) = \frac{[S_h']^{-1}(\alpha_t, \alpha_b)n^d(\alpha_t)}{IEVGEN_b} \qquad (4.16)$$

Systematic error due to finite MC statistics

In order to estimate the systematic error that arises from a finite MC sample, a random variation technique was applied. One hundred random smearing matrices were generated using a Gaussian distribution around the central values of the migration sums and Born sums with a standard deviation corresponding to the MC statistics recorded in each hybrid bin. The data was then unfolded using each of these random smearing matrices and the systematic error assigned using the standard deviation of the unfolded results.

4.4 Cross Check

This analysis was cross checked by comparing multiplicities with A. Hillenbrand in a different hybrid binning that contained one more bin in z $(0.1 - 0.2)$. These two analyses were performed using completely independent codes. The remaining kinematic cuts and data quality cuts were identical for both the cross check and this analysis. For all years and all polarization states we found a disagreement of less than 1% in the central values and errors of the pion multiplicities after all corrections and unfolding. Fig. 4.6 shows an example (π^+) of the better than 2% agreement reached in the cross check.

4.5 Multiplicities

The resulting multiplicities for charged pions from the hydrogen (deuterium) target are shown in Fig. 4.7 (Fig. 4.8). As is expected from factorization the multiplicities are essentially independent from x in a given z bin. The statistical error shown includes the
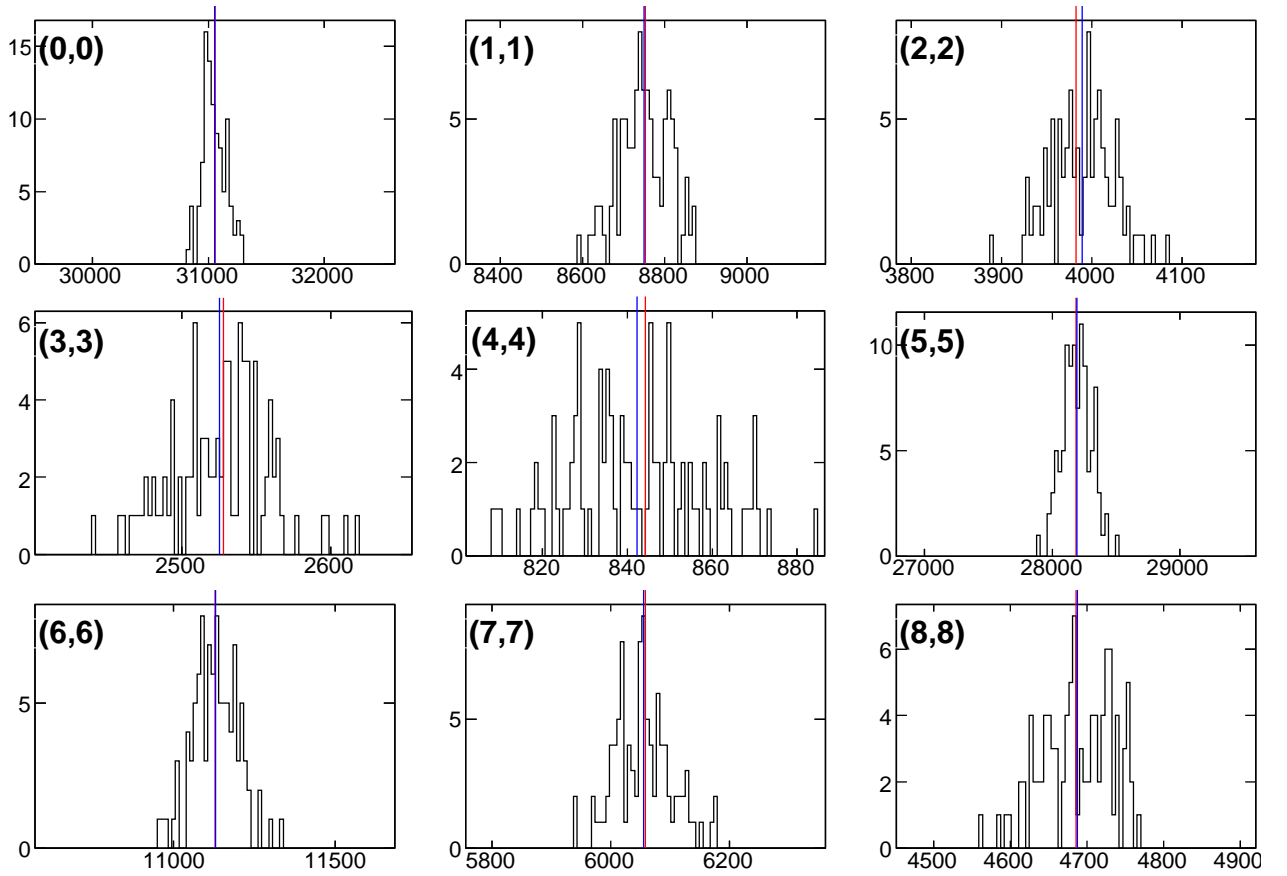
Figure 4.5: An example of the Gaussian distribution of diagonal elements in the hydrogen MC migration matrix for positive pions. The red line corresponds to the mean used in the Gaussian and the blue line corresponds to the calculated mean of the resulting distribution. Only the first nine diagonal elements are shown.
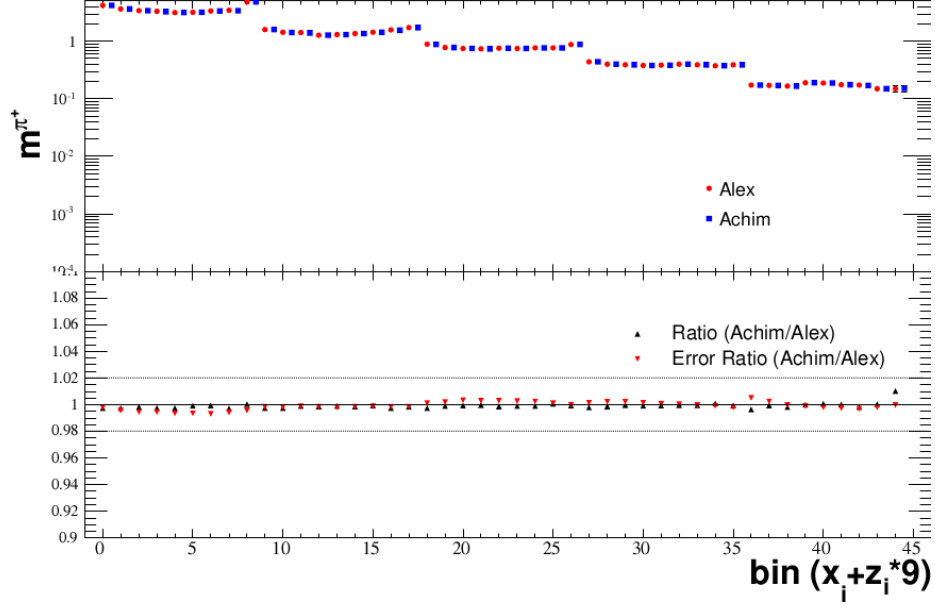
Figure 4.6: Representative example of precision reached in multiplicity cross check. Here the analysis results from an independent analyzer (blue) and this analysis (red) are compared for positive pions using the unpolarized hydrogen data in the 00d0 production.

inflation from the VMD correction, charge symmetric background correction and smearing unfolding. The systematic error boxes are the combination of the RICH efficiency and the smearing matrix systematic error.

We have also extracted the charged kaon multiplicities from the two different targets. These are shown in Fig. 4.9 and Fig. 4.10. For all the multiplicities the measured values are given in Appendix B.3.

4.6 Systematic Studies

4.6.1 Year Dependence

In order to ensure the validity of combining all years of available data together for this analysis a study of the year-to-year variation of the multiplicities was made. Two different statistics were calculated to determin the consistency between years. The first test was that $\sim 66\%$ of the data points should lie within $\pm$ one standard deviation of the errors added in quadrature. The second test was a calculation of the $\chi^2/D.O.F$ which should be ~ 1 if
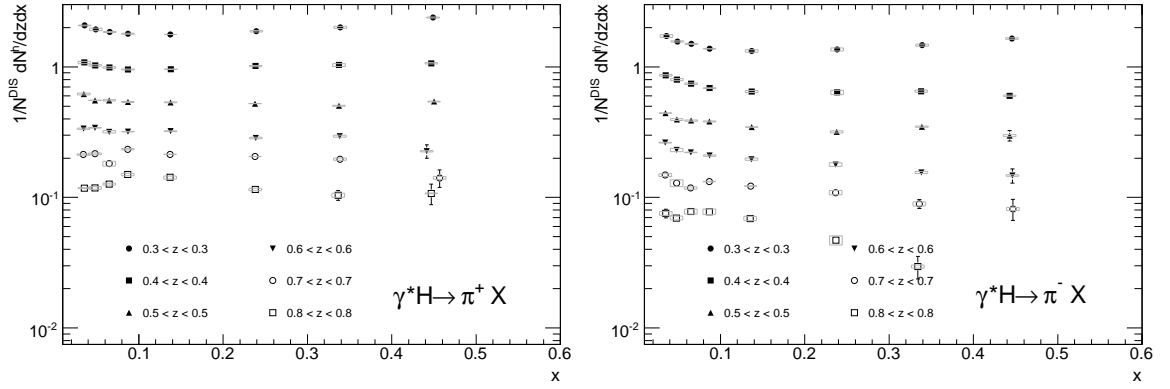
Figure 4.7: The charged pion multiplicities extracted from all of the data included in this analysis on the hydrogen target. The black lines represent the statistical error and the grey boxes are the systematic error.
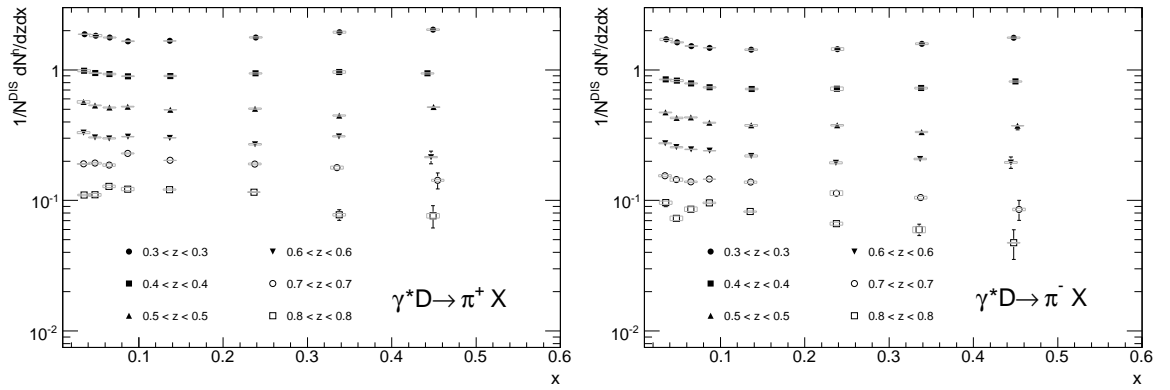
Figure 4.8: The charged pion multiplicities extracted from all of the data included in this analysis on the deuterium target. The black lines represent the statistical error and the grey boxes are the systematic error.
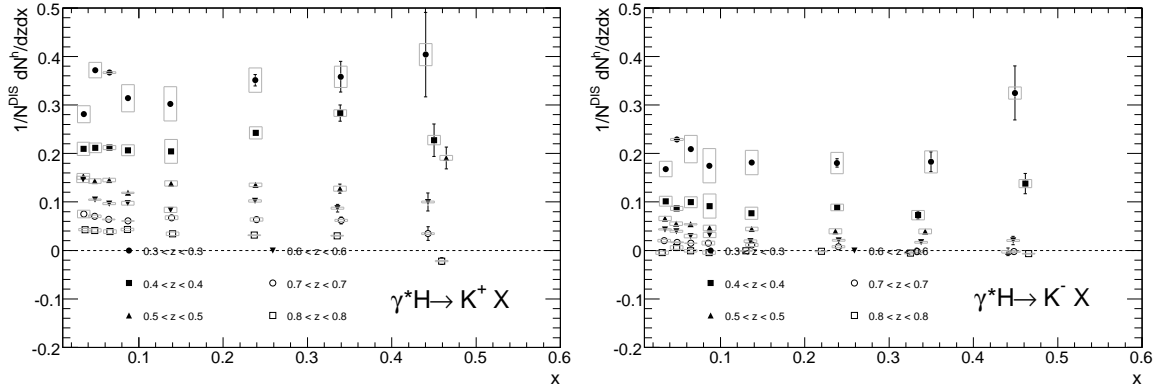
Figure 4.9: The charged kaon multiplicities extracted from all of the data included in this analysis on the hydrogen target. The black lines represent the statistical error and the grey boxes are the systematic error.

Figure 4.10: The charged kaon multiplicities extracted from all of the data included in this analysis on the deuterium target. The black lines represent the statistical error and the grey boxes are the systematic error.

72
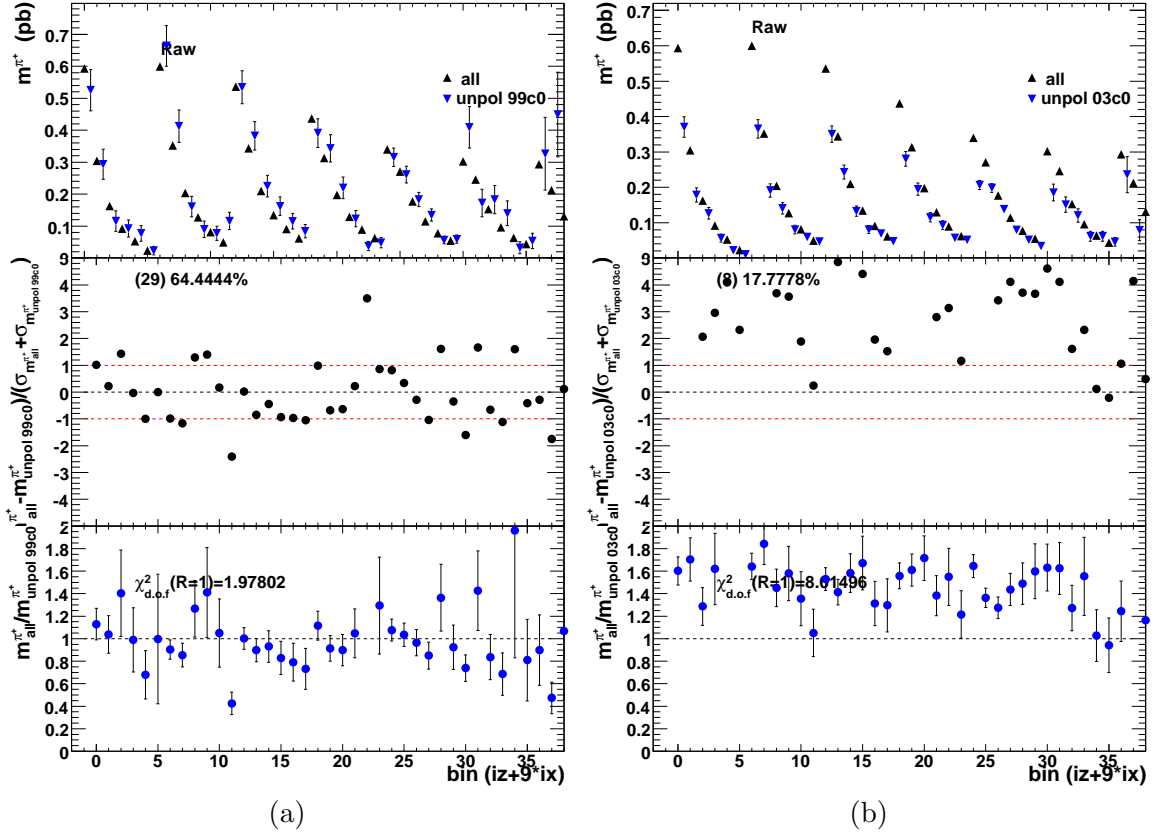
Figure 4.11: Two data sets (a) 99c0 and (b) 03c0 are shown to be in gross disagreement with the average multiplicity and have been discarded.

the data agree. The result was that two productions 03c0 and 99c0 that were in complete disagreement with the average which can be seen in Fig. 4.11. We have decided to discard these data sets due to the disagreement and lack of statistics they provide. Another target and polarization state that showed a non-zero systematic difference was 00d0 polarized data. This data represents one third of the deuterium data available for this analysis. It was hypothesized that this difference could be due to the pre-scaling of triggers for high density running, which was standard procedure before the DAQ upgrade, coupled with an inefficiency in trigger 21 (DIS trigger) due to H0 damage. This hypothesis was tested by checking the other RUN I data included in the analysis (1998, 1999) for the same inter-year inconsistency and by comparing the two data sets again when a trigger 21 cut was applied to both. In the 1998 and 1999 data sets the effect was not seen. The effect of applying the trigger 21 cut can be seen in the right panel of Fig. 4.12, and does not improve the

73
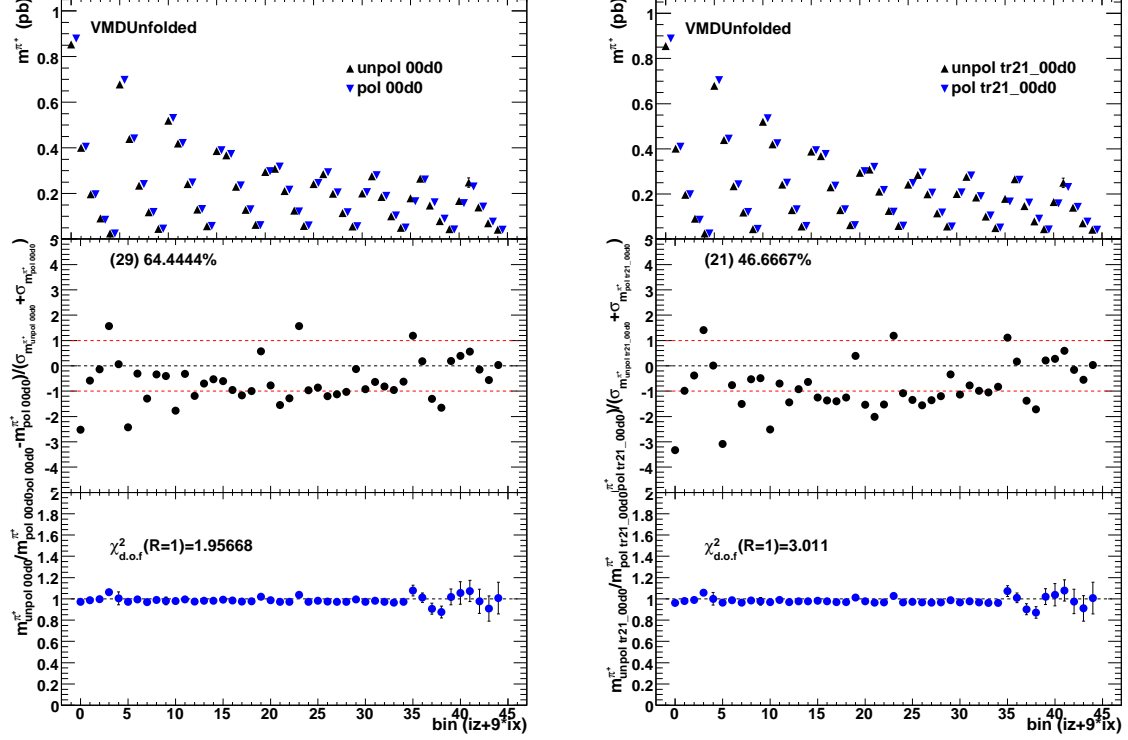
Figure 4.12: The inter-year multiplicity comparison of polarized and unpolarized data from 2000 (left). On the right, the same comparison is made when a trigger 21 cut is applied to the data.

discrepancy between the polarized and un-polarized data. Therefore, we have also made the difficult choice to exclude the 00d0 polarized deuterium data from the analysis due to this inconsistency. The loss of this data, while a large statistical sample may have little effect on the final statistical error due to the large asymmetry in the available data for hydrogen and deuterium.

Despite these few troublesome data sets, the typical agreement of the data from year to year was quite good. For example Fig. 4.13 shows the comparison for both charged pions from the 00d0 unpolarized hydrogen sample. It should be pointed out that the scale for the ratio panel (lower) between Fig. 4.11 and Fig. 4.13 is different. For all the years included the ratio has less than 5% deviation.
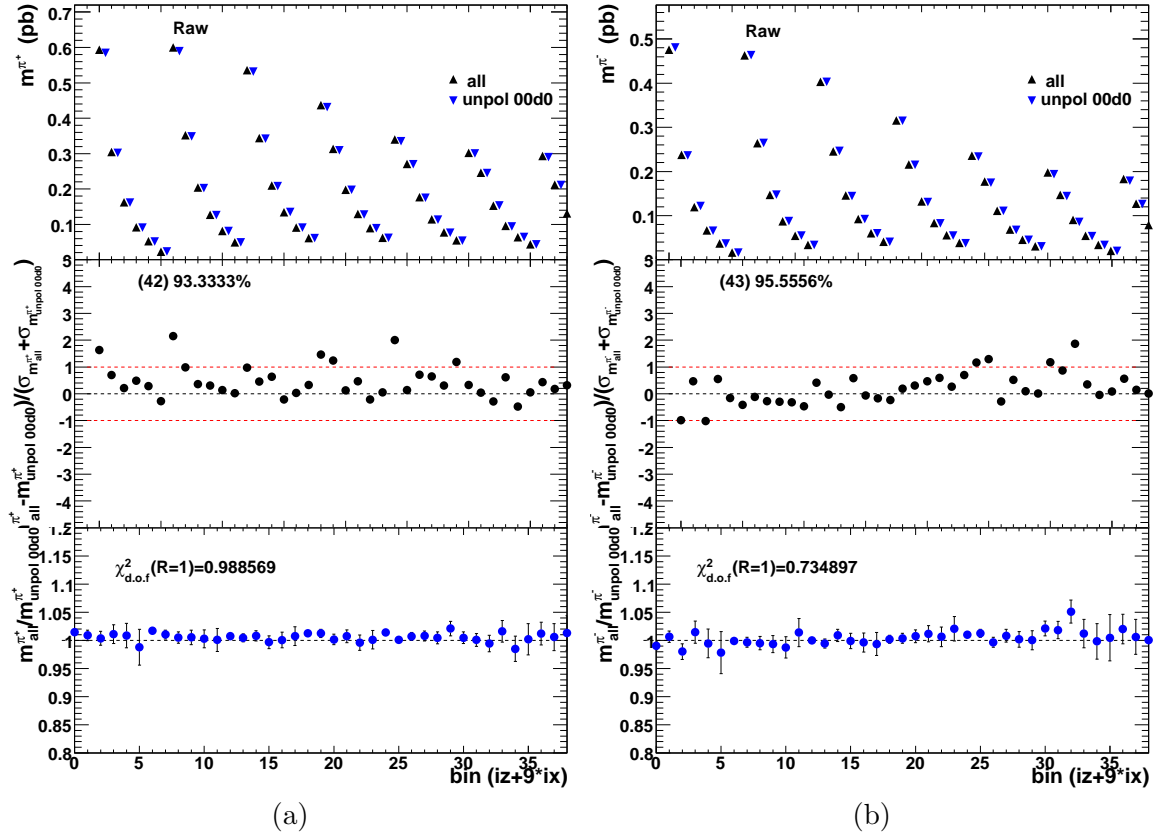
Figure 4.13: Two data set 00d0 (a) π^+ and (b) π^- are shown to be in good agreement with the average multiplicity.

4.7 Results of d_v/u_v Extraction

In this section we present the results of the analysis that we would like to release. We find that the ratio $d_v(x)/u_v(x)$ is consistently lower at low x than the predictions made from modern parton distribution fits (Fig. 4.14a). The highest x bin of the extraction suffers from a non-physical value of $d_v/u_v < 0$ and had thus been forced to the positivity limit and the difference in the value from zero has been added in quadrature with the systematic error. It is likely that the assumptions needed for the extraction method break down in the highest x bin. We also see a slight residual z dependence in the result (Fig. 4.14b) which is unexpected if the formalism is truly sound, and may be evidence for factorization breaking or the breakdown of the assumed fragmentation symmetries. These effects have been studied extensively by the author, in terms of kinematic and target dependences, these studies are catalogued in Appendix C. We would like to stress however that the cross-check is in excellent shape and therefore we believe that any shortcomings of the result are due to the method employed and not bugs in the analysis code. It may be that the flavor tagging LO arithmetic extraction of this quantity fails when such a high precision data set is available.

4.7.1 Q^2 Evolution

In order to address the possibility that the remaining slope seen in the unfolded valence ratio could be a Q^2 evolution artifact we performed a simple evolution of this quantity to $Q_0^2 = 2.5$ for all z bins. It is unexpected that this evolution will have much effect on the ratio due to the fact that the numerator and denominator of the ratio should follow a very similar Q^2 evolution. The correction was applied multiplicatively to the measured ratio and was calculated using the ratio of CTEQ6L [85] parton distribution fits at the average scale of the bin and the evolved scale.

$$\frac{d_v(x,Q_0^2)}{u_v(x,Q_0^2)}_{meas.} = \left(\frac{d_v(x,Q^2)}{u_v(x,Q^2)}\right)_{meas.} \left(\frac{d_v(x,Q^2)}{u_v(x,Q^2)}\right)^{-1}_{CTEQ6L} \left(\frac{d_v(x,Q_0^2)}{u_v(x,Q_0^2)}\right)_{CTEQ6L} \tag{4.17}$$

(a)

(b)
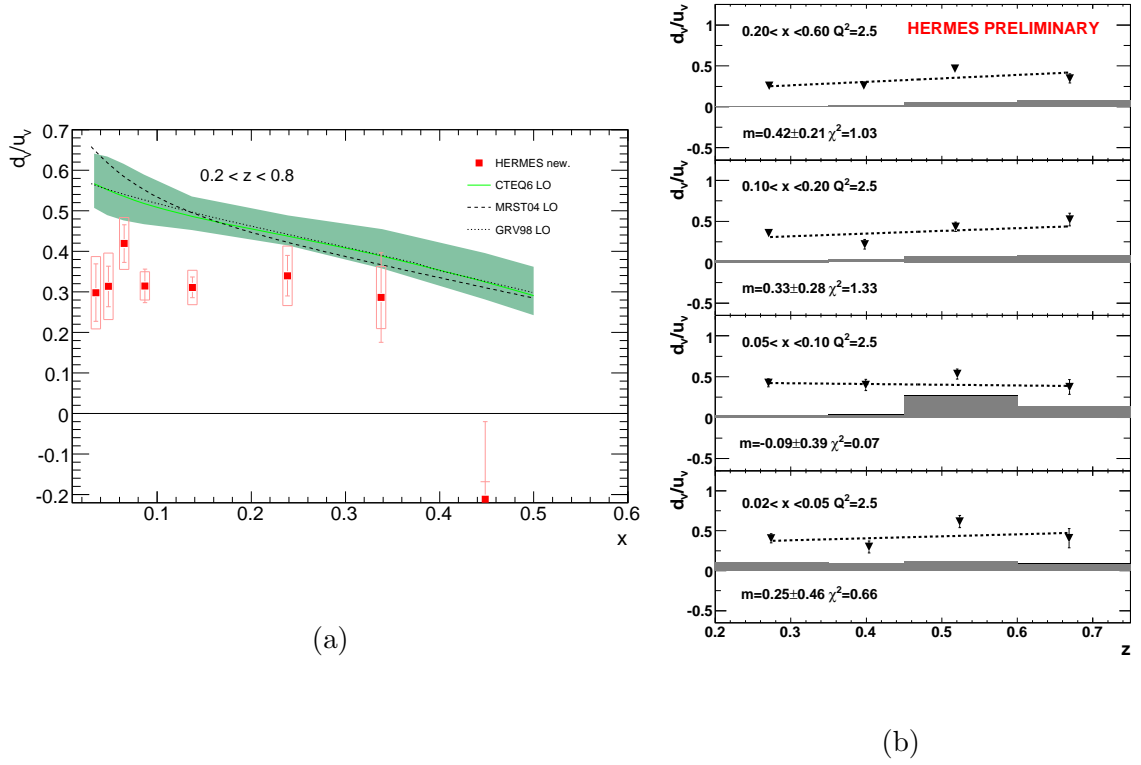
Figure 4.14: (a) The valence PDF ratio (d_v/u_v) as a function of x. (b) The valence PDF ratio (d_v/u_v) as a function of z, where all the points have been Q^2 evolved to 2.5GeV^2. Here, m gives the slope of the fit line and the fit χ^2 is also shown.

The correction is on the order of 1% for most bins with the largest being 3%, and it has a negligible effect on the remaining z dependence of the extracted unfolded valence ratio (Fig. 4.14b).

4.7.2 Results Without 4π and Radiative Unfolding.

In view of the large error inflation introduced by the final unfolding procedure, to account for the limited detector acceptance and bin-migration due to radiative and smearing effects, the valence ratio before these corrections is also included. Fig. 4.15 shows the results of extracting d_v/u_v without the final unfolding step, i.e. without correcting for radiative effects, detector smearing, or fiducial acceptance (only statistical errors). This plot demonstrates that the deviation from the parameterization becomes larger when the unfolding is performed. Additionally the last point that was forced to the positivity limit in the unfolded extraction no longer has a negative value. Due to the complicated nature of the smearing correction it is not clear what is causing the systematic movement in the result, but it is assumed that the final systematic error correctly accounts for this movement.

4.7.3 M_X Factorization Effects

Using the Monte Carlo one can extract the valence quark ratio knowing what the answer should be. The ability to invert the MC is a "proof of principle" that the chosen technique is correct. It also allows one to look for kinematic regimes where the extraction breaks down. We have performed a study demonstrating that the extraction of d_v/u_v works better when a missing mass cut (M_X) is made for the MC.

$$M_X = \sqrt{\nu^2(1-z)^2 + M_P^2 + 2\nu M_P(1-z) + |P_h|^2 - Q^2 + 2|P_h \cdot q|} \qquad (4.18)$$

The conclusion of this study was that the cut reduced the breaking of the fragmentation symmetries and thus the algebraic extraction of d_v/u_v could be improved by making a lower limit cut on the missing mass. By comparing the input PDF (CTEQ6LO) and the extracted result a χ^2 statistic can be calculated. Shown in Fig. 4.16a is the χ^2 agreement for the test which improves for the M_X cuts of 3 and 4 over the cut at 1.5. This is an inverse cut from
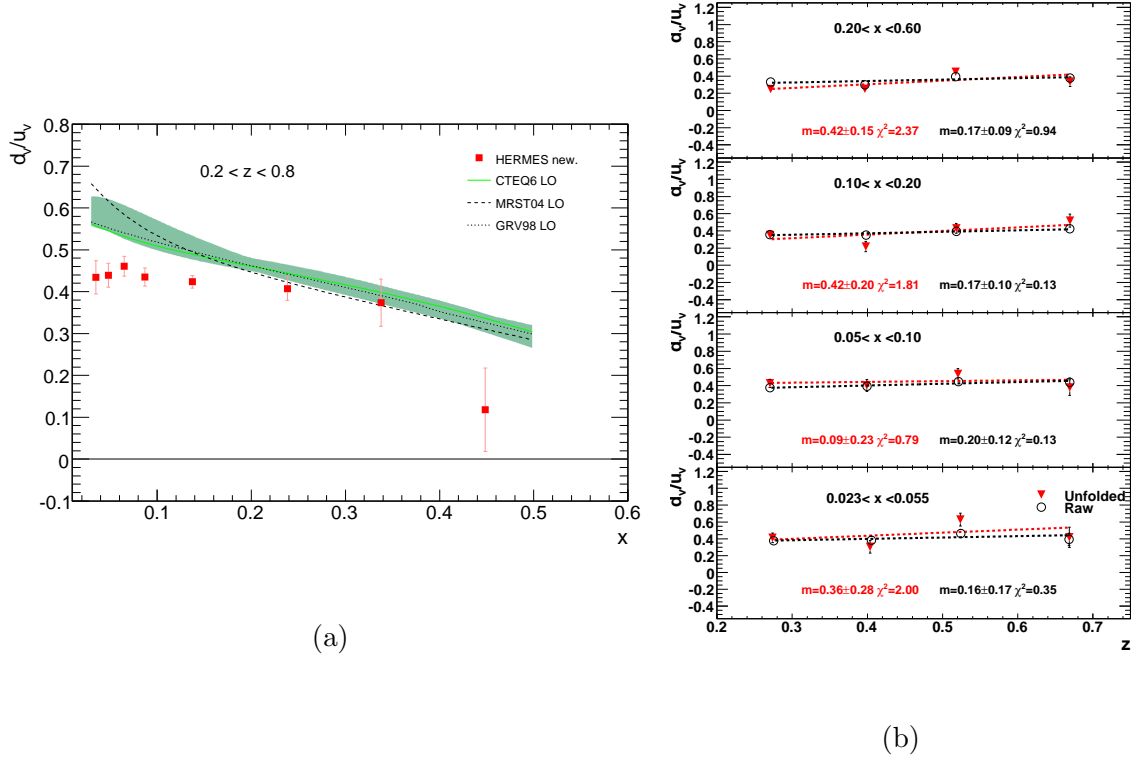
Figure 4.15: (a) Comparison of the effects of radiative unfolding on the residual z dependence. (b) Comparison of the effects of unfolding on the z dependence of the result.

what is typically used in exclusive physics analysis and is intended to further distance our analysis from a region where true deep inelastic scattering is not occurring.

The same study was performed with the data. However due to the strong correlation between z and M_X (Fig. 4.16b), the full smearing and acceptance unfolding proved problematic. Typically we would find un-populated diagonal bins in the smearing matrix which causes it to be non-invertible. We can thus only compare the effects of the M_X cut with the charge symmetric background and vector meson corrections. Fig. 4.17 shows the results of this M_X scan.

Unfortunately, the cut did not remove the slight z dependence in the final result and was abandoned for the final result.

4.7.4 Dependence on p_T

The parton distribution functions depend not only on the longitudinal momentum fraction x but also on the quarks' intrinsic transverse momentum k_T. Obtaining information on
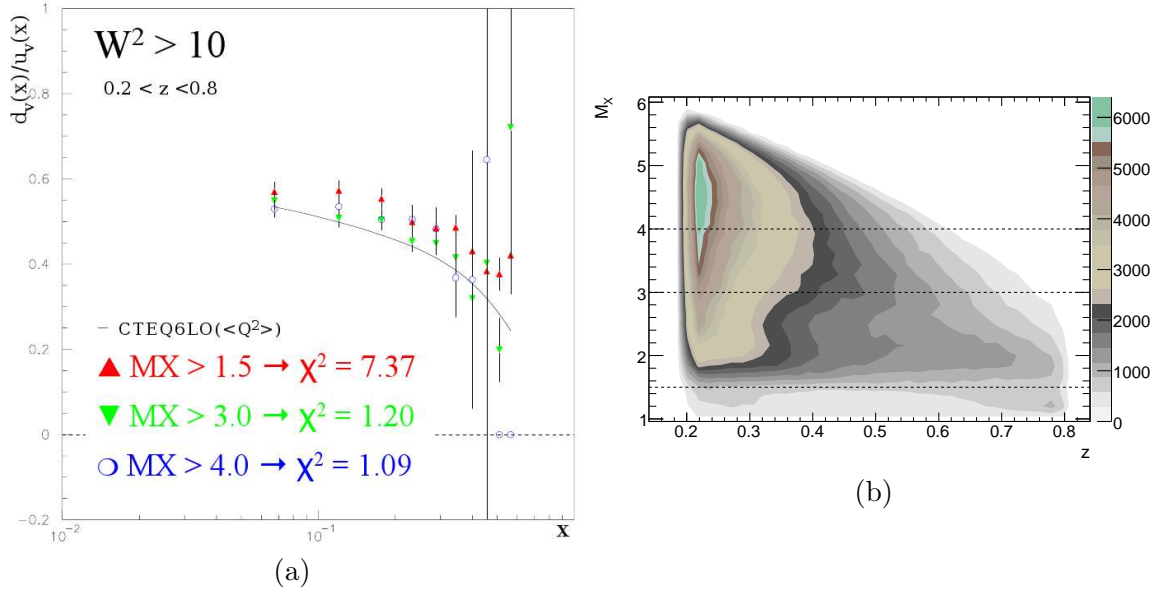
Figure 4.16: (a) Monte Carlo extraction of the valence ratio for different missing mass cuts and the resulting χ^2 calculated between the input and extracted values. (b) The correlation between missing mass and track energy fraction from MC data.

the k_T-dependence of the PDFs of different flavor is a much sought-after goal in hadronic physics: a measured difference between $u_v(x, k_T)$ and $d_v(x, k_T)$, for example, would be provide a powerful input to phenomenological pictures of the proton, such as the quark-diquark or meson cloud models.

At first sight, the use of final-state pions to "tag" the struck quark, as is done in the SIDIS analysis technique presented here, offers unique access to k_T: the detected pion's transverse momentum must reflect the struck quark's initial momentum to some extent. However the observed final-state hadron momentum p_T^h is inevitably a *convolution* over two sources of transverse momentum: the intrinsic k_T of the struck quark within the target nucleon, and the transverse momentum p_T which the hadron picks up from the fragmentation process. In the Lund model of fragmentation the latter comes from color-string breaking, as quarks and anti-quarks produced in pairs from the vacuum during fragmentation acquire a transverse momentum relative to the jet axis which is typically modelled by a Gaussian probability distribution. Including these transverse momentum degrees of freedom, the cross-section for semi-inclusive hadron production may be written as the following

80
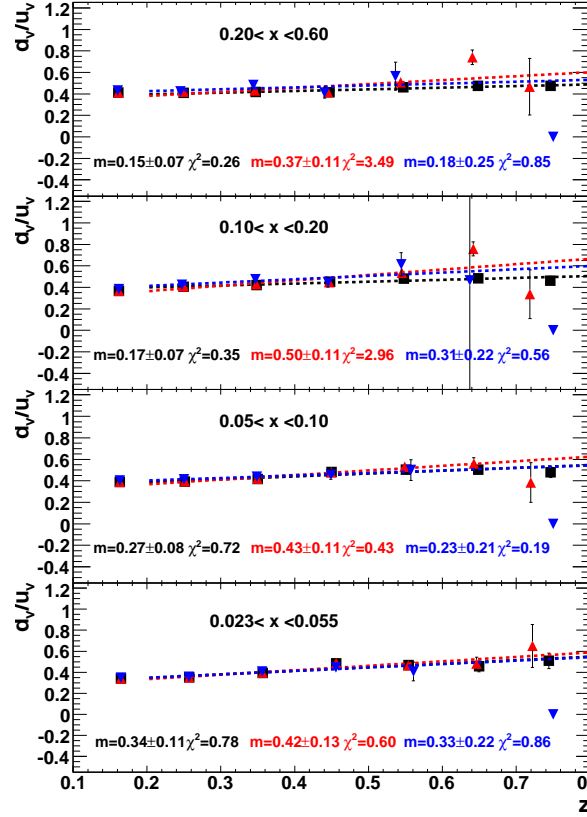
Figure 4.17: The z dependence of the data when an M_X cut is made. The black squares represent no M_X cut, red triangles are $M_X > 3.0$ and blue upside down triangles are $M_X > 4.0$

convolution integral:

$$\frac{d^3\sigma}{dp_T^h dz dx} \propto \int dp_T dk_T \; \delta(p_T^h - k_T - p_T) \; q(x, k_T) \; D_q^h(z, p_T) \qquad (4.19)$$

Despite the complications in interpretation engendered by the presence of these two sources of transverse momentum, it is instructive to look at the data's dependence on p_T^h. Fig. 4.19 and 4.18 shows the multiplicities for π^+ and π^- production from the proton and deuteron targets as a function of x in six slices of p_T^h. Here, p_T^h is defined as the component of the pion's momentum which is transverse to the virtual photon direction. As expected, the multiplicities are largest at intermediate values of p_T^h: at low values the phase space is restricted (by the usual differential factor $d^2\vec{p}_T^h = 2\pi p_T^h dp_T^h$), while large values come from the falling tails of the soft $q(x, k_T)$ and $D(z, p_T)$ distributions. We note that at the largest values of p_T, next-to-leading order hard-scattering processes become the dominant contributions to the cross-section, but Monte Carlo studies performed for other HERMES analysis have indicated that these processes (photon-gluon fusion and QDC Compton) become significant only at values of p_T^h above 1 GeV or so. Fig. 4.18 shows that the pion multiplicities peak in the $0.3 < p_T^h < 0.4$ GeV region. This corresponds well to the Gaussian widths of around 0.4 GeV typically used to model the k_T and p_T dependence of the distribution and fragmentation functions respectively.

Fig. 4.22 shows the result of using these p_T^h-binned multiplicities to extract the PDF ratio d_v/u_v. The dominant dependence of the quantity on x is removed as much as possible by plotting versus p_T^h in four slices of x. No clear p_T^h dependence is observed in the data within the uncertainties of the measurement. This is not unexpected, as the convolution of intrinsic-quark k_T and fragmentation p_T is likely to obscure a possible flavor dependence of intrinsic k_T in the nucleon. However, the precision of the data is encouraging. With the addition of the large HERMES 2006-2007 data set, it may be possible to explore the p_T^h, x and z dependences simultaneously and perhaps to isolate corners of this three-dimensional phase space where one or the other source of transverse momentum is dominant. A candidate is to look at the high z region where the detected pions carry almost all of the available energy. Very few string breaks are involved in this near-exclusive production regime; this
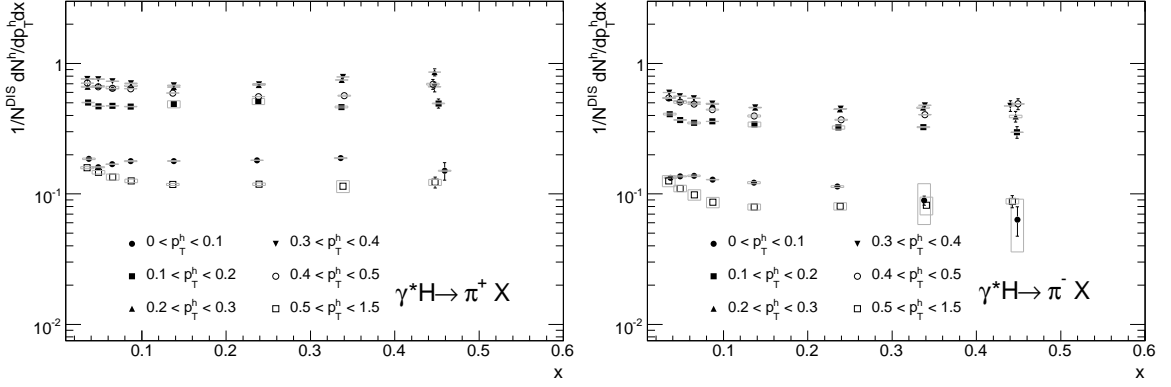
Figure 4.18: The charged pion multiplicities extracted from all of the data included in this analysis on the hydrogen target. The black lines represent the statistical error and the grey boxes are the systematic error.
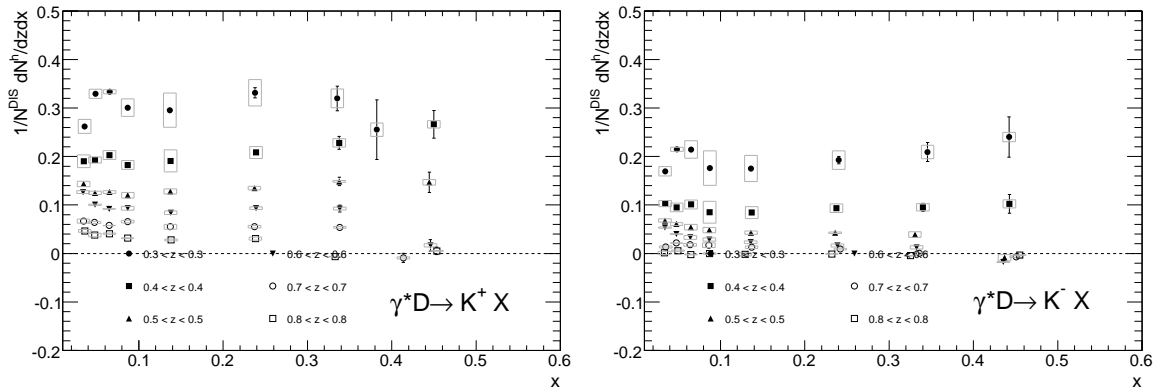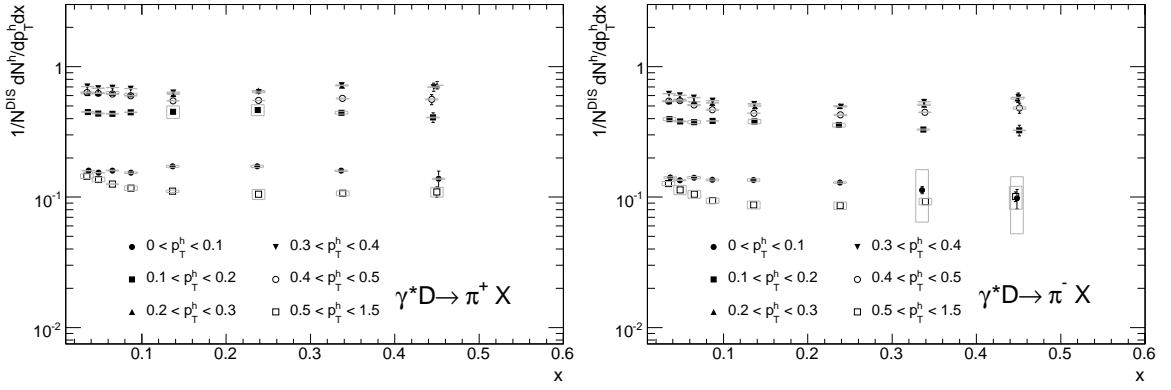

Figure 4.19: The charged pion multiplicities extracted from all of the data included in this analysis on the deuterium target. The black lines represent the statistical error and the grey boxes are the systematic error.

can be expected to reduce the amount of p_T arising from fragmentation and perhaps isolate the true k_T dependence of d_v/u_v.

4.8   Results of the Light Sea Asymmetry Extraction

In Fig. 4.23 we present the light sea asymmetry extracted from the measured multiplicities of charged pions on the hydrogen and deuterium targets. As described in Section 2.4.2 this extraction requires the fragmentation function ratio η as an input. We have chosen too use the FDSS [5] parameterization for this input. There is an inherent systematic
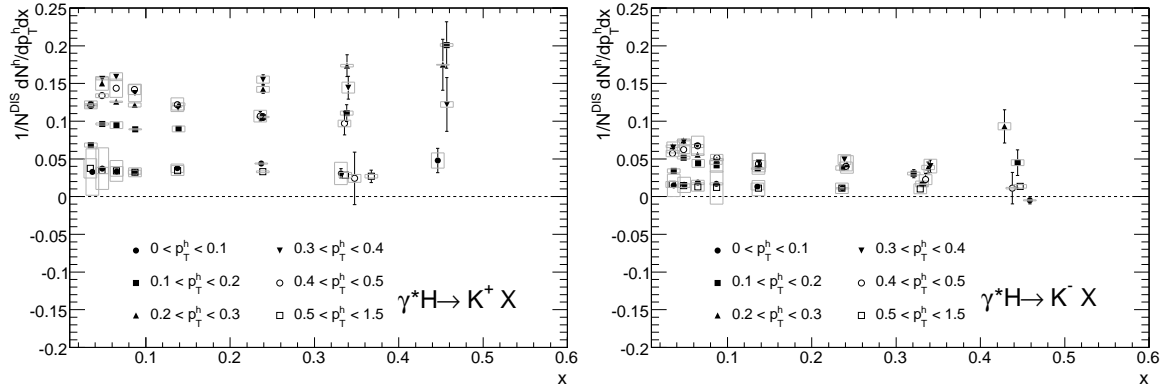
Figure 4.20: The charged kaon multiplicities extracted from all of the data included in this analysis on the hydrogen target. The black lines represent the statistical error and the grey boxes are the systematic error.
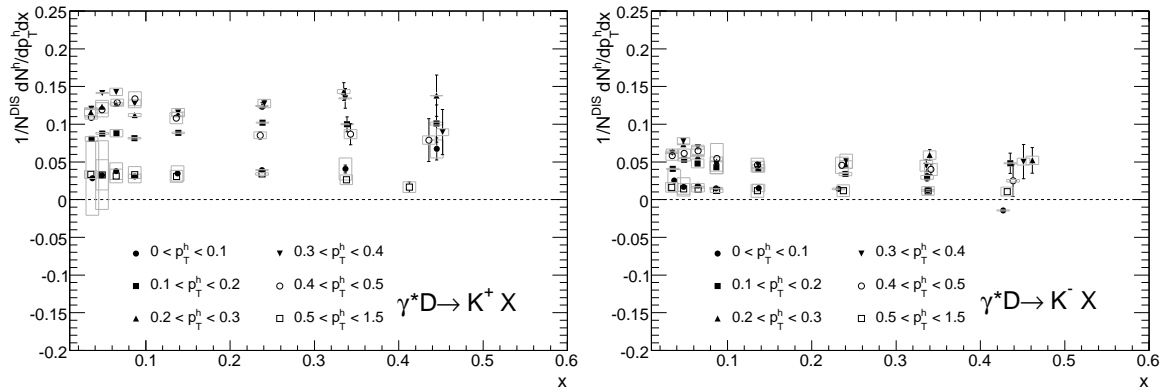
Figure 4.21: The charged kaon multiplicities extracted from all of the data included in this analysis on the deuterium target. The black lines represent the statistical error and the grey boxes are the systematic error.
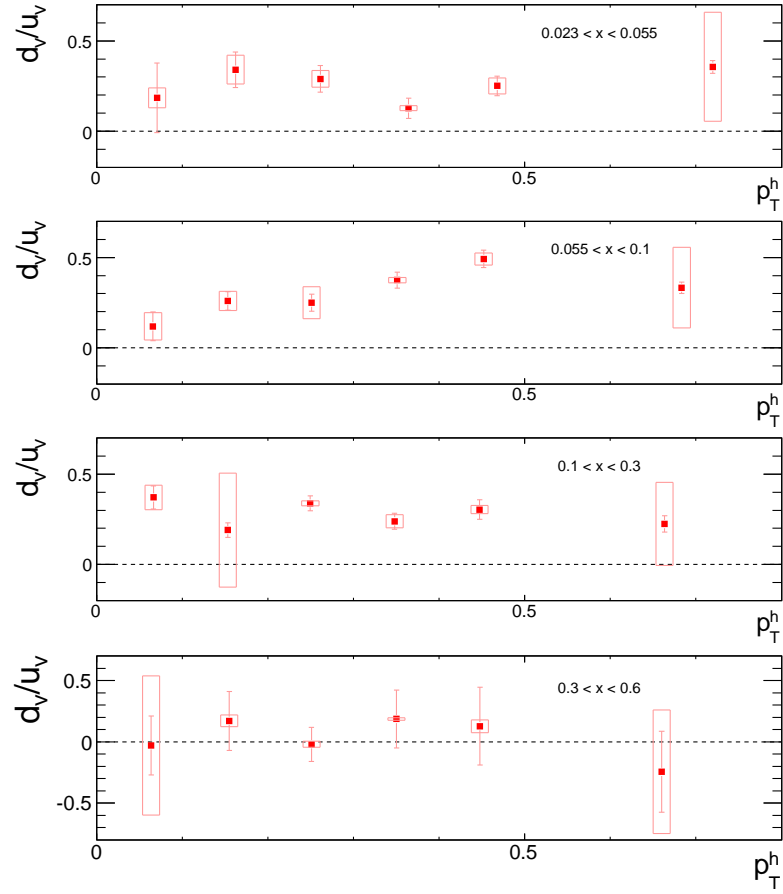
Figure 4.22: The valence quark ratio as a function of hadron transverse momentum for four x ranges.
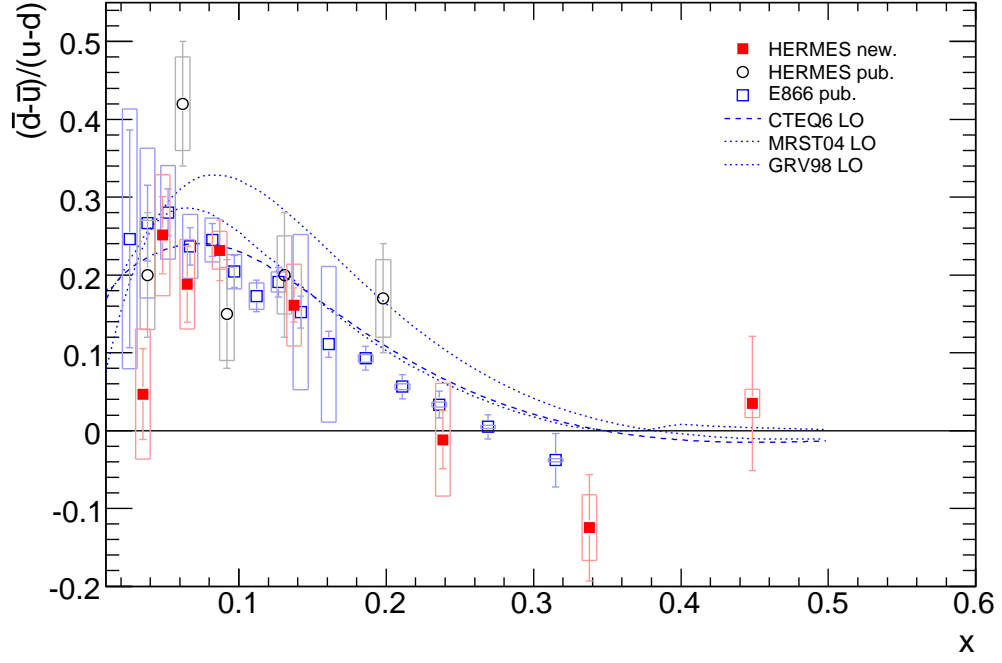
Figure 4.23: The extracted values compared to the previously released result and to parameterizations by CTEQ and MRST.

error that comes from the choice of fragmentation function and while we want to evaluate this honestly we also do not want to overestimate it and reduce the impact of the result. Therefore, we have assigned a systematic error as the absolute difference between the results when using the fDSS and Kretzer [4] parameterizations which give $J(z) = 1.49$ and $J(z) = 1.68$ respectively. This systematic error is found to be negligible compared to the other systematic errors from RICH unfolding and finite smearing matrix statistics.

Chapter 5

Conclusions

5.1 PDF extracted quantities

5.1.1 Valence Moment

If we integrate the valence ratio over the measured x range 0.023–0.6 we find the moment ratio (Eq. 2.21) $d_v/u_v = 0.34 \pm 0.08$ (stat.) ± 0.13 (sys.). For reference we have also calculated the moment of the CTEQ6LO distribution over the same x range. The value is $d_v/u_v = 0.47$. Within two σ of the total error these two quantities are equivalent. For both the parameterization and the data a large fraction of the integral must come from the unmeasured x range. It is clear however from Fig. 4.14 that there is a systematic deviation of the data points on the order of 2σ from the parameterizations. One possible explanation for this could be that the CTEQ6L parameterizations do not include data from a kinematic range that corresponds to that covered by the HERMES experiment. Figure 5.1 shows the inputs used in the parameterization and explicitly points out the $Q^2 > 4$ requirement for the inclusion of data. One can see that a significant fraction of the HERMES data samples a different kinematic regime from the data used in the fit.

Another possibility is that the formalism assumed for this extraction breaks down at low x especially. One interesting test is to ask how much breaking in the factorization symmetries can cause such a deviation.

5.1.2 Factorization Breaking

The favored and dis-favored fragmentation function symmetries are the result of implying charge conjugation symmetry and iso-spin rotation as discussed in Section 2.1.6. In this
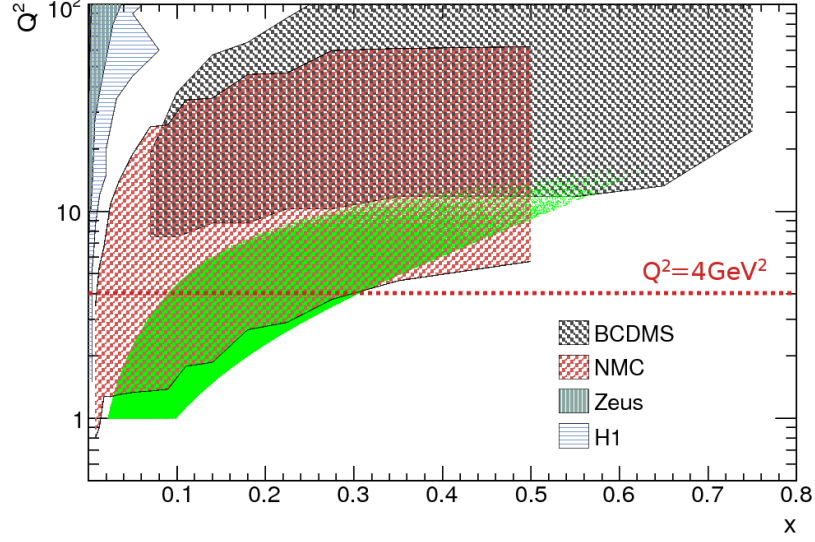
Figure 5.1: The range of kinematic data used by the CTEQ collaboration for PDF fitting, superimposed in green is the kinematic coverage of the HERMES experiment. The red dashed line represents the Q^2 cutoff CTEQ requires.

approach we assume the following definition for the favored (dis-favored) fragmentation functions

$$D_1(z, Q^2) \equiv D_u^{\pi^+}(z, Q^2) = D_{\bar{u}}^{\pi^-}(z, Q^2) \tag{5.1}$$

$$D_2(z, Q^2) \equiv D_{\bar{u}}^{\pi^+}(z, Q^2) = D_u^{\pi^-}(z, Q^2)$$

holds for the u quark sector. We can then re-define the remaining light quark fragmentation functions in terms of $D_1(z, Q^2)$, $D_2(z, Q^2)$ and symmetry breaking terms Δ_q^h (here q refers to the struck quark flavor and h the detected hadron type). For instance, the dis-favored d quark to positive pion transition can be written as:

$$D_d^{\pi^+}(z, Q^2) = D_2(z, Q^2) + \Delta_d^{\pi^+}(z, Q^2) \tag{5.2}$$

The mechanism responsible for the possible symmetry breaking in DIS may be related to the environment in which the string breaks occur. Therefore, we believe that the symmetry breaking terms may be target dependent. If this is the case they will require a target index
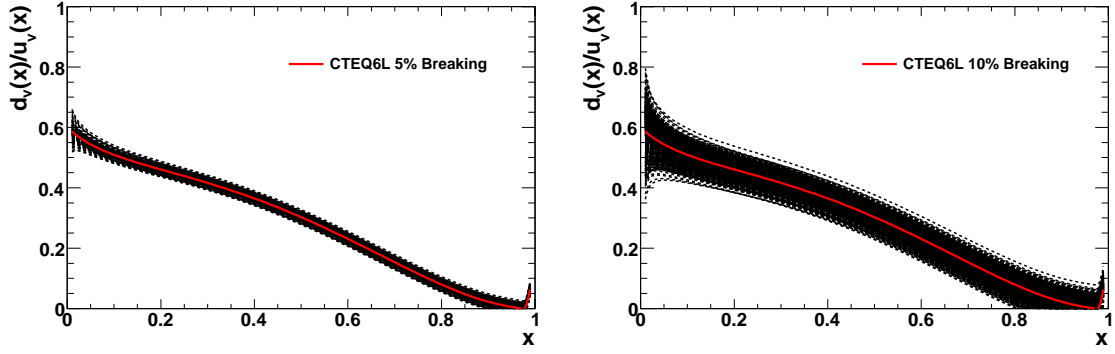
Figure 5.2: The symmetry breaking effects on the naive extraction of the valence quark asymmetry in the proton.

(t) as well and can be written $\Delta_{q,t}^h$, where we have dropped the explicit Q^2 dependence. Including this symmetry violation in the simple expression for the valence ratio in terms of r^π demonstrates the contamination symmetry breaking terms. This effect is manifest in the fact that r^π is no longer a simple expression containing the valence ration but has the independent quark and anti-quark distributions folded in through the symmetry breaking. If this symmetry violation pion difference target ratio is used in place of the naive extraction the result may vary. Here the symmetry breaking parameters f are defined as:

$$f_q^t \equiv (\Delta_{q,t}^{\pi^+} - \Delta_{q,t}^{\pi^-})/(D_1 - D_2) \tag{5.3}$$

The variations were made around the central distribution given by the CTEQ6LO [85]. Each parameter was thrown randomly according to a Gaussian with a mean of zero and a width set to the maximum symmetry breaking of that run. The pion ratio was then calculated and the valence ratio extracted. The resulting envelopes (Fig. 5.2) predict the range in variation that is possible when the symmetry breaking parameters are allowed to vary from 5 to 30% of the favored (dis-favored) fragmentation function difference.

In order to test this theory it is instructive to calculate the same quantity using the fragmentation functions from the HERMES MC. The HERMES MC fragmentation functions for u and d quarks are plotted in Fig 5.3. We see some small variation in the favored and dis-favored fragmentation function from u and d quarks which we can quantify in this
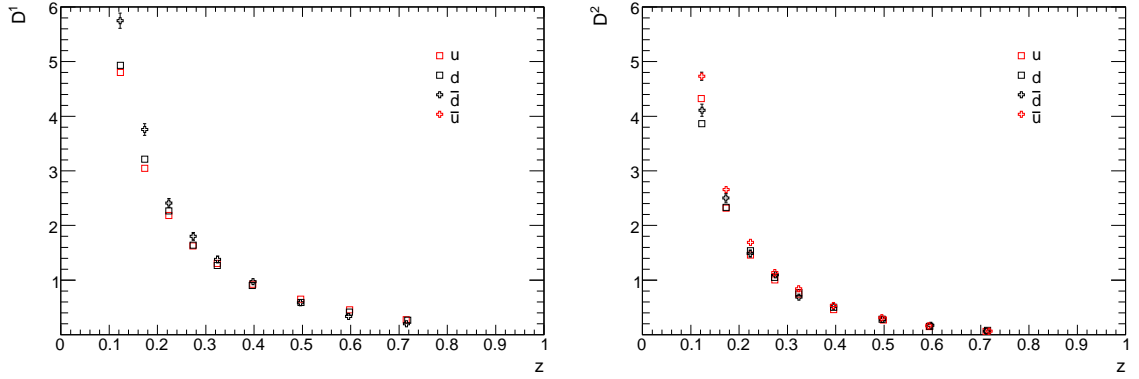
Figure 5.3: The favored (left) and dis-favored fragmentation functions from the HERMES MC.

toy model.

If we calculate the symmetry breaking parameter for the d quark shown in the figure we find a value of $f_d = 0.65\%$, which seems far too low to cause the deviation we see. However if we perform the same exercise for $\bar{d}$ we find that the symmetry breaking is on the order of $f_{\bar{d}} = 3\%$ which according to the tests can result in a large systematic deviation from the central value as shown in the 5% panel (upper right) of Fig. 5.2. In our test we assumed that the symmetry held implicitly for the $\bar{u}$ quark however, from the MC simulation we calculate that $f_{\bar{u}}$ could be as high as 2.5%. Despite the simplicity of this test and the fact that the MC FF are merely a phenomenological model it does present one possible explanation for the systematic deviation seen in the extracted valence ratio.

5.1.3 Light sea asymmetry moment

In order to calculate the moment that correspond to the Gottfried Sum Rule we must employ a model for the valence difference $u - d$. If we use the CTEQ6LO distribution to calculate this moment over the measured x range (0.023-6) we find $S_G = \bar{d} - \bar{u} = 0.051 \pm 0.014(\text{stat.}) \pm 0.012$ (sys.). This quantity can again be compared to the value that can be computed from the CTEQ6LO light anti-quark distributions alone. In that case we find $S_G = 0.084$. Again note that the extracted quantity is compatible within errors with the parameterization. In this case, as above, we need to be careful with our interpretation

because the remainder of the x range is unmeasured and for this moment the CTEQ6LO valence PDFs were required to extract the moment.

5.1.4 Summary

We have presented the analysis of the HERMES SIDIS data set for the years 2000 through 2007. This data set is the largest of its kind in the world and represents the efforts of countless individuals to ensure its quality. From this data set we have extracted the hadron multiplicities for charged pions, kaons and protons separated using the dual radiator ring imaging Cerenkov detector that is part of the HERMES spectrometer. These high precision multiplicities which have been corrected for backgrounds, the spectrometer acceptance and QED radiative effects (Born level), will be valuable contributions to the world's understanding of QCD and nucleon structure in a number of ways. First they will help to constrain fragmentation function parameterizations and models that attempt to phenomenologically reproduce measured quantities. The SIDIS data will have a large impact in this arena due to its ability to distinguish between quark flavors, which makes symmetry assumptions for the fragmentation functions unnecessary. This is essential for future experiments, such as PBSM searches at the LHC will require well known inputs for PDFs and FFs in order to discern small statistical deviations from expected results. The kaon multiplicities are of particular interest because they may help to constrain the strange sea asymmetry that has been reported by the NuTeV experiment [86]. This PDF extraction is currently limited by the applicability of the fragmentation symmetries in the kaon sector.

In addition to measuring the multiplicities we have tried to extract information about the unpolarized parton distribution functions inside the nucleon. These quantities are extracted using the QCD improved parton model using a technique termed flavor tagging. For the valence quark ratio extraction we find a systematic deviation from the world fits for which we cannot, at the moment, state a clear reason. The moment calculated in the measured x range of this quantity is compatible with the moment of parameterizations calculated over the same range. One possibility is that the formalism we have used breaks down to some degree and the quantity we are trying to extract is not purely the ratio of valence quark

structure. We have performed a simple MC to see what effects relaxing the fragmentation symmetry assumptions may have on the final result. This study showed that one could achieve a discrepancy on the order of what we extracted from the data if the symmetry is broken. This study was motivated by the idea that a parton fragmenting in the SIDIS environment may be different from that of electron positron colliders which could have an effect on these symmetries.

An extraction of the light sea asymmetry was also performed using the measured multiplicities. This result agrees well with parameterizations and the measurement conducted at the Drell-Yan experiment E866. Additionally, the moment calculated in the measured x range agrees with the previous measurement within $< 1\sigma$ of the errors. It is unfortunate that the corrections applied to the data cause the error inflation discussed in the text, but the extracted data points $x < 0.1$ still have better precision than the Drell-Yan experiment and are the most precise SIDIS extraction to date. Another drawback to this analysis is that it requires the fragmentation moment as an input; for this the fDSS parameterization was chosen. This choice is motivated by comparing the FFs to the output of a Monte Carlo simulation that has been tuned to reproduce the data within the acceptance.

The technique of flavor tagging hadrons to extract information about nuclear structure is an excellent idea. As we produce larger data sets which allow more precise determination of these algebraic quantities we may find that many of the assumptions used in the QCD-improved parton model break down. This will make it necessary to use more applicable frameworks in the future to extract such quantities.

Appendix

A   Other Physics Contributions

In addition to sitting shifts on the HERMES experiment from 2001 until the HERA shut-down in 2007, I contributed to the experiment and the University of Illinois Nuclear Physics group in a number of ways. While performing studies using the PEPSI [87] Monte Carlo code to determine the systematic errors inherent in the Δq purity extraction method [88], I discovered a bug in the Iso-Spin rotation section of the code. I fixed this bug and the patch was committed to the HERMES Monte Carlo (HMC). In the following year, the HMC code was given to the COMPASS experiment with the patch included.

During my graduate school tenure I had the great fortune of being a part of the University of Illinois (UIUC) Nuclear Physics Laboratory (NPL). Having such a large group of excellent experimental physicists necessitates substantial local computing resources. In 2003, I was asked to take over the administration and development of the local computing farm ($\sim$20 nodes), which was established and previously maintained by Fred Gray. This farm was used for data analysis and simulation related to the BNL Muon g-2, PSI MuCap, PSI MuLan, JLab RCS, KEK Belle and Daya-Bay neutrino experiments. I jumped at this opportunity to improve my technical computer skills and knowledge as well as the opportunity to learn from colleagues working on experiments much different than my own. During the following four years I was involved in solving and assisting to solve many unique computing problems that arose. These spanned the gammut from helping colleagues install and compile physics simulation and analysis packages such as GEANT4, GARFIELD, LHC++ and ROOT to much more mundane tasks such as replacing failed hardware. I benefitted greatly from this opportunity and would like to thank the UIUC principal investigators Dave Hertzog and Doug Beck for giving me this position and their support during my tenure. I would also like to thank my replacement Dave Webber, a graduate student working on the MuLan experiment who took over as the system guru when I departed Illinois.

Finally, I was also lucky enough to spend one summer working with Matthias Grosse-Perdekamp on a portion of the PHENIX RPC upgrade project which is spearheaded at UIUC NPL. I assisted the PHENIX group in setting up the top and bottom trigger scintil-lators for the RPC test stand. This included acquiring the necessary parts, light checking

and cosmic testing the setup. In addition, I worked on a software implementation of the proposed relative luminosity telescope (RLT) in the PHENIX Monte Carlo framework PISA. This was a valuable experience and gave me some of my only hands-on experience with experimental nuclear physics apparatus. I am still involved in this project today and have performed tests on the timing resolution of the small prototype chambers at the University of Colorado in addition to developing the embedded software that will be used for setting thresholds on the front end electronics. It is a very exciting time for this project due to the delivery of the first full-size prototype and first version of the front-end readout electronics.

B Data Tables

B.1 Valence ratio

xbin	$< x >$	$d_v(x)/u_v(x)$	$\pm\sigma_{stat.}$	$\pm\sigma_{sys.}$
0	0.035	0.298	0.0707	0.0892
1	0.0482	0.313	0.05	0.0822
2	0.0651	0.419	0.0464	0.064
3	0.0871	0.315	0.0411	0.0347
4	0.137	0.311	0.0255	0.0425
5	0.238	0.34	0.0501	0.0734
6	0.338	0.286	0.11	0.0764
7	0.448	0	0.191	0.254

Table 1: Valence quark ratio extracted from HERMES charged pion multiplicities. For this extraction the positivity limit has been enforced

B.2 Light sea asymmetry

xbin	$< x >$	$(\bar{d} - \bar{u})/(u - d)$	$\pm\sigma_{stat.}$	$\pm\sigma_{sys.}$
0	0.035	0.0469	0.0581	0.0834
1	0.0482	0.251	0.0493	0.0775
2	0.0651	0.188	0.0486	0.0576
3	0.0871	0.232	0.039	0.0243
4	0.137	0.161	0.0219	0.0523
5	0.238	-0.0118	0.0371	0.0724
6	0.338	-0.125	0.0684	0.0423
7	0.448	0.0349	0.0864	0.0184

Table 2: Light sea asymmetry extracted from HERMES charged pion multiplicities. The lines represent the statistical error and the boxes are the systematic.

B.3 Multiplicities

xbin	zbin	$<x>$	$<z>$	$<Q^2>$	$m_p^{\pi^+}$	$\pm\sigma_{stat.}$	$\pm\sigma_{sys.}$
1	1	0.0357	0.264	1.31	2.08	0.0121	0.0129
1	2	0.0353	0.365	1.28	1.08	0.00932	0.0196
1	3	0.0349	0.462	1.25	0.619	0.00793	0.00947
1	4	0.0345	0.556	1.22	0.336	0.00691	0.00413
1	5	0.0343	0.648	1.19	0.213	0.00702	0.00221
1	6	0.0353	0.741	1.14	0.118	0.00756	0.00121
2	1	0.0488	0.253	1.55	1.93	0.0106	0.0417
2	2	0.0484	0.351	1.49	1.03	0.00772	0.0126
2	3	0.0481	0.451	1.45	0.555	0.00603	0.00204
2	4	0.048	0.55	1.43	0.342	0.00531	0.00137
2	5	0.048	0.65	1.38	0.216	0.0047	0.00348
2	6	0.048	0.747	1.32	0.118	0.0039	0.00258
3	1	0.0654	0.251	1.88	1.85	0.01	0.0175
3	2	0.0653	0.35	1.78	0.991	0.00701	0.0136
3	3	0.065	0.448	1.73	0.554	0.00537	0.006
3	4	0.0649	0.549	1.7	0.318	0.00433	0.00668
3	5	0.0649	0.649	1.64	0.181	0.00385	0.00783
3	6	0.0648	0.747	1.55	0.126	0.00329	0.00232
4	1	0.0872	0.25	2.4	1.8	0.0105	0.016
4	2	0.0871	0.348	2.19	0.954	0.00702	0.01
4	3	0.087	0.448	2.11	0.539	0.00535	0.00462
4	4	0.087	0.548	2.06	0.319	0.00452	0.0013
4	5	0.087	0.649	2.03	0.234	0.00425	0.00249
4	6	0.087	0.747	1.91	0.15	0.00374	0.00335
5	1	0.137	0.25	3.55	1.77	0.00736	0.00202
5	2	0.138	0.347	3.19	0.96	0.00481	0.00425
5	3	0.138	0.446	3.1	0.535	0.00363	0.00364
5	4	0.138	0.548	3.05	0.321	0.00307	0.00205
5	5	0.137	0.647	2.99	0.214	0.00289	0.000757
5	6	0.137	0.747	2.91	0.142	0.00247	0.00382
6	1	0.239	0.25	5.7	1.88	0.0169	0.0282
6	2	0.238	0.346	5.22	1.02	0.0105	0.0111
6	3	0.238	0.446	5.2	0.523	0.00749	0.00146
6	4	0.239	0.547	5.18	0.285	0.00593	0.00381
6	5	0.238	0.647	5.19	0.206	0.00555	0.000233
6	6	0.238	0.747	5.21	0.115	0.00451	0.00263
7	1	0.339	0.251	7.51	2.01	0.0377	0.0352
7	2	0.337	0.347	7.28	1.03	0.0234	0.0248
7	3	0.337	0.446	7.32	0.504	0.0165	0.00557
7	4	0.338	0.548	7.42	0.295	0.0132	0.00546
7	5	0.339	0.646	7.33	0.196	0.0112	0.00404
7	6	0.336	0.743	7.37	0.104	0.00925	0.00377
8	1	0.449	0.245	9.99	2.39	0.085	0.0251
8	2	0.447	0.347	9.7	1.07	0.0507	0.0126
8	3	0.45	0.446	9.96	0.543	0.0357	0.00363
8	4	0.442	0.546	9.69	0.226	0.0265	0.00249
8	5	0.457	0.646	10	0.141	0.0216	0.00325
8	6	0.447	0.746	10.2	0.107	0.0194	0.000785

Table 3: CSB, VMD, radiative and acceptance corrected $m_p^{\pi^+}$ multiplicity results binned in z and x from the all years production.

xbin	zbin	$< x >$	$< z >$	$< Q^2 >$	$m_p^{\pi^-}$	$\pm\sigma_{stat.}$	$\pm\sigma_{sys.}$
1	1	0.0361	0.266	1.33	1.72	0.011	0.0417
1	2	0.0351	0.362	1.27	0.861	0.0084	0.0126
1	3	0.0349	0.463	1.25	0.443	0.00685	0.00204
1	4	0.0344	0.557	1.22	0.263	0.00595	0.00137
1	5	0.0346	0.654	1.2	0.148	0.00562	0.00348
1	6	0.0352	0.741	1.14	0.0755	0.00575	0.00258
2	1	0.049	0.253	1.56	1.56	0.00962	0.0175
2	2	0.0484	0.352	1.49	0.799	0.0069	0.0136
2	3	0.0482	0.452	1.45	0.395	0.00518	0.006
2	4	0.048	0.553	1.42	0.231	0.00447	0.00668
2	5	0.048	0.649	1.38	0.129	0.00386	0.00783
2	6	0.0479	0.746	1.32	0.0695	0.0033	0.00232
3	1	0.0654	0.25	1.9	1.5	0.00889	0.016
3	2	0.0653	0.349	1.79	0.742	0.0061	0.01
3	3	0.0651	0.45	1.72	0.388	0.00459	0.00462
3	4	0.0649	0.549	1.68	0.221	0.0036	0.0013
3	5	0.0647	0.647	1.63	0.118	0.00315	0.00249
3	6	0.0649	0.748	1.55	0.0779	0.00281	0.00335
4	1	0.0871	0.249	2.41	1.38	0.00918	0.00202
4	2	0.0871	0.347	2.18	0.688	0.00593	0.00425
4	3	0.087	0.447	2.1	0.382	0.00456	0.00364
4	4	0.0871	0.547	2.02	0.209	0.00371	0.00205
4	5	0.0869	0.648	1.97	0.132	0.00337	0.000757
4	6	0.0869	0.746	1.88	0.0777	0.00304	0.00382
5	1	0.137	0.249	3.57	1.32	0.00631	0.0282
5	2	0.137	0.347	3.19	0.647	0.0039	0.0111
5	3	0.137	0.446	3.04	0.346	0.00296	0.00146
5	4	0.137	0.547	2.99	0.196	0.00238	0.00381
5	5	0.136	0.647	2.9	0.122	0.00222	0.000233
5	6	0.135	0.747	2.83	0.0689	0.0018	0.00263
6	1	0.238	0.249	5.69	1.36	0.0142	0.0352
6	2	0.239	0.346	5.23	0.638	0.00827	0.0248
6	3	0.238	0.445	5.08	0.317	0.00576	0.00557
6	4	0.237	0.545	5.02	0.178	0.00461	0.00546
6	5	0.237	0.646	5.09	0.109	0.00384	0.00404
6	6	0.237	0.746	4.98	0.0471	0.0029	0.00377
7	1	0.339	0.249	7.62	1.47	0.0312	0.0251
7	2	0.338	0.346	7.17	0.651	0.0182	0.0126
7	3	0.339	0.445	7.17	0.348	0.013	0.00363
7	4	0.338	0.548	7.21	0.155	0.00921	0.00249
7	5	0.336	0.648	7.38	0.0893	0.00706	0.00325
7	6	0.334	0.748	7.05	0.0296	0.00578	0.000785
8	1	0.446	0.247	9.83	1.65	0.0675	0.0219
8	2	0.443	0.343	9.55	0.601	0.0375	0.00679
8	3	0.443	0.442	9.68	0.297	0.0272	0.0053
8	4	0.446	0.545	9.73	0.147	0.0183	0.00188
8	5	0.447	0.639	9.57	0.0817	0.015	0.00211
8	6	0.46	0.749	7.5	-0.0487	0.00498	0.000803

Table 4: CSB, VMD, radiative and acceptance corrected $m_p^{\pi^-}$ multiplicity results binned in z and x from the all years production.

xbin	zbin	$<x>$	$<z>$	$<Q^2>$	$m_d^{\pi^+}$	$\pm\sigma_{stat.}$	$\pm\sigma_{sys.}$
1	1	0.0357	0.263	1.31	1.88	0.00929	0.00764
1	2	0.0351	0.362	1.27	0.985	0.00722	0.0177
1	3	0.0346	0.459	1.24	0.569	0.00626	0.0122
1	4	0.0345	0.556	1.22	0.331	0.00565	0.00632
1	5	0.0345	0.648	1.2	0.19	0.00585	0.00148
1	6	0.0352	0.746	1.14	0.11	0.00638	0.00148
2	1	0.0488	0.253	1.55	1.83	0.00849	0.037
2	2	0.0484	0.352	1.49	0.946	0.00617	0.00688
2	3	0.0482	0.452	1.45	0.535	0.00496	0.00277
2	4	0.0479	0.55	1.41	0.304	0.00418	0.00248
2	5	0.048	0.649	1.39	0.193	0.00381	0.00264
2	6	0.0479	0.746	1.32	0.111	0.00335	0.00268
3	1	0.0654	0.25	1.89	1.77	0.00807	0.0143
3	2	0.0652	0.349	1.79	0.929	0.00567	0.0131
3	3	0.0651	0.449	1.74	0.515	0.00445	0.00549
3	4	0.0648	0.549	1.7	0.299	0.00367	0.00304
3	5	0.0648	0.648	1.64	0.187	0.00327	0.00428
3	6	0.0647	0.746	1.54	0.128	0.00297	0.00283
4	1	0.0871	0.25	2.4	1.66	0.00845	0.00957
4	2	0.0871	0.348	2.18	0.894	0.00574	0.00627
4	3	0.087	0.447	2.11	0.523	0.00447	0.00336
4	4	0.087	0.548	2.07	0.308	0.00365	0.00127
4	5	0.0869	0.648	2.01	0.229	0.00355	0.00206
4	6	0.0868	0.747	1.89	0.122	0.00293	0.00358
5	1	0.137	0.25	3.55	1.67	0.00607	0.00428
5	2	0.137	0.347	3.19	0.899	0.00396	0.00899
5	3	0.137	0.447	3.1	0.495	0.003	0.00286
5	4	0.137	0.547	3.03	0.301	0.00255	0.000578
5	5	0.137	0.647	2.99	0.203	0.00236	0.000354
5	6	0.136	0.748	2.88	0.121	0.00189	0.0013
6	1	0.239	0.25	5.69	1.77	0.0145	0.0181
6	2	0.238	0.347	5.25	0.941	0.00893	0.00913
6	3	0.238	0.446	5.21	0.504	0.00639	0.00576
6	4	0.238	0.547	5.17	0.269	0.00502	0.00403
6	5	0.237	0.647	5.16	0.19	0.00458	0.00274
6	6	0.237	0.747	5.1	0.116	0.00381	0.0009
7	1	0.338	0.25	7.55	1.94	0.0341	0.0355
7	2	0.338	0.345	7.28	0.963	0.0202	0.0227
7	3	0.338	0.447	7.27	0.447	0.014	0.00541
7	4	0.337	0.546	7.33	0.31	0.0118	0.00354
7	5	0.335	0.647	7.37	0.178	0.01	0.00475
7	6	0.338	0.749	7.55	0.0776	0.00739	0.00182
8	1	0.449	0.249	9.87	2.04	0.0753	0.0271
8	2	0.442	0.349	9.6	0.941	0.044	0.0123
8	3	0.449	0.445	9.94	0.52	0.0334	0.00351
8	4	0.447	0.546	10	0.215	0.0238	0.0025
8	5	0.455	0.654	10.3	0.143	0.02	0.00263
8	6	0.449	0.757	9.88	0.0764	0.0149	0.00316

Table 5: CSB, VMD, radiative and acceptance corrected $m_d^{\pi^+}$ multiplicity results binned in z and x from the all years production.

xbin	zbin	$<x>$	$<z>$	$<Q^2>$	$m_d^{\pi^-}$	$\pm\sigma_{stat.}$	$\pm\sigma_{sys.}$
1	1	0.0357	0.263	1.31	1.71	0.009	0.037
1	2	0.0351	0.362	1.27	0.845	0.00668	0.00688
1	3	0.0348	0.461	1.25	0.473	0.00573	0.00277
1	4	0.0344	0.558	1.22	0.274	0.00517	0.00248
1	5	0.0343	0.651	1.2	0.155	0.00521	0.00264
1	6	0.0352	0.744	1.14	0.0962	0.00657	0.00268
2	1	0.0488	0.253	1.55	1.63	0.00797	0.0143
2	2	0.0484	0.352	1.49	0.828	0.00584	0.0131
2	3	0.0481	0.451	1.45	0.429	0.00446	0.00549
2	4	0.0479	0.551	1.41	0.256	0.00386	0.00304
2	5	0.0478	0.649	1.37	0.145	0.00348	0.00428
2	6	0.0478	0.746	1.31	0.073	0.00307	0.00283
3	1	0.0654	0.251	1.89	1.52	0.00731	0.00957
3	2	0.0652	0.349	1.79	0.788	0.00525	0.00627
3	3	0.065	0.449	1.72	0.433	0.0041	0.00336
3	4	0.0651	0.549	1.68	0.247	0.00331	0.00127
3	5	0.0648	0.648	1.63	0.139	0.00294	0.00206
3	6	0.0648	0.747	1.54	0.0858	0.00269	0.00358
4	1	0.0871	0.25	2.4	1.48	0.00789	0.00428
4	2	0.087	0.348	2.18	0.736	0.00515	0.00899
4	3	0.087	0.447	2.09	0.394	0.00388	0.00286
4	4	0.0871	0.548	2.04	0.24	0.0033	0.000578
4	5	0.087	0.649	1.98	0.146	0.00301	0.000354
4	6	0.0868	0.747	1.89	0.0957	0.0029	0.0013
5	1	0.136	0.249	3.54	1.43	0.00558	0.0181
5	2	0.137	0.347	3.17	0.715	0.00346	0.00913
5	3	0.137	0.446	3.03	0.376	0.00256	0.00576
5	4	0.137	0.546	2.97	0.219	0.0021	0.00403
5	5	0.136	0.647	2.91	0.138	0.00193	0.00274
5	6	0.135	0.747	2.81	0.0822	0.00166	0.0009
6	1	0.239	0.249	5.7	1.44	0.0128	0.0355
6	2	0.238	0.346	5.19	0.718	0.0077	0.0227
6	3	0.238	0.446	5.16	0.376	0.00556	0.00541
6	4	0.237	0.547	5.09	0.194	0.00414	0.00354
6	5	0.238	0.645	5.02	0.114	0.00364	0.00475
6	6	0.237	0.747	5.01	0.0664	0.00274	0.00182
7	1	0.339	0.251	7.53	1.59	0.0295	0.0271
7	2	0.338	0.346	7.21	0.726	0.0174	0.0123
7	3	0.338	0.445	7.2	0.334	0.012	0.00351
7	4	0.337	0.545	7.2	0.208	0.00919	0.0025
7	5	0.338	0.647	7.14	0.105	0.00696	0.00263
7	6	0.336	0.747	7.48	0.0598	0.0059	0.00316
8	1	0.448	0.248	9.82	1.77	0.0644	0.0193
8	2	0.45	0.348	9.9	0.815	0.0397	0.00876
8	3	0.452	0.447	10.1	0.374	0.0264	0.00182
8	4	0.444	0.544	9.99	0.195	0.0196	0.00291
8	5	0.454	0.66	9.91	0.0852	0.0149	0.00192
8	6	0.448	0.745	9.91	0.0474	0.0121	0.000364

Table 6: CSB, VMD, radiative and acceptance corrected $m_d^{\pi^-}$ multiplicity results binned in z and x from the all years production.

xbin	zbin	$<x>$	$<z>$	$<Q^2>$	$m_p^{K^+}$	$\pm\sigma_{stat.}$	$\pm\sigma_{sys.}$
1	1	0.0348	0.258	1.27	0.281	0.00617	0.0175
1	2	0.0344	0.355	1.25	0.21	0.00478	0.0136
1	3	0.0342	0.453	1.24	0.153	0.0048	0.006
1	4	0.0339	0.558	1.23	0.147	0.0051	0.00668
1	5	0.0347	0.655	1.2	0.075	0.00403	0.00783
1	6	0.0362	0.739	1.13	0.0428	0.00367	0.00232
2	1	0.0484	0.25	1.49	0.372	0.00664	0.016
2	2	0.0483	0.352	1.48	0.212	0.00421	0.01
2	3	0.0479	0.448	1.46	0.143	0.00347	0.00462
2	4	0.0479	0.551	1.46	0.105	0.00311	0.0013
2	5	0.0478	0.647	1.42	0.0704	0.00281	0.00249
2	6	0.0477	0.745	1.34	0.0413	0.00222	0.00335
3	1	0.0653	0.251	1.84	0.367	0.00642	0.00202
3	2	0.0653	0.349	1.78	0.212	0.00392	0.00425
3	3	0.0649	0.449	1.75	0.145	0.00301	0.00364
3	4	0.0649	0.549	1.78	0.0964	0.00255	0.00205
3	5	0.0644	0.645	1.71	0.0639	0.00224	0.000757
3	6	0.0659	0.75	1.6	0.0389	0.00189	0.00382
4	1	0.0871	0.252	2.37	0.314	0.00638	0.0282
4	2	0.0871	0.349	2.2	0.207	0.00397	0.0111
4	3	0.087	0.449	2.16	0.119	0.00286	0.00146
4	4	0.087	0.547	2.18	0.0975	0.00249	0.00381
4	5	0.0871	0.647	2.14	0.061	0.00233	0.000233
4	6	0.0865	0.747	2	0.0431	0.0019	0.00263
5	1	0.138	0.25	3.57	0.302	0.00453	0.0352
5	2	0.138	0.349	3.26	0.204	0.00266	0.0248
5	3	0.138	0.448	3.18	0.138	0.00209	0.00557
5	4	0.138	0.546	3.18	0.0836	0.00173	0.00546
5	5	0.139	0.647	3.21	0.0675	0.00171	0.00404
5	6	0.14	0.746	3.17	0.0344	0.00128	0.00377
6	1	0.238	0.252	5.77	0.351	0.0117	0.0251
6	2	0.239	0.347	5.36	0.243	0.00671	0.0126
6	3	0.238	0.447	5.34	0.135	0.00446	0.00363
6	4	0.238	0.547	5.33	0.102	0.00387	0.00249
6	5	0.24	0.649	5.4	0.0638	0.00335	0.00325
6	6	0.237	0.744	5.26	0.0316	0.00253	0.000785
7	1	0.339	0.257	7.67	0.358	0.0316	0.0219
7	2	0.339	0.347	7.41	0.283	0.0166	0.00679
7	3	0.339	0.449	7.58	0.128	0.00952	0.0053
7	4	0.336	0.545	7.19	0.0872	0.00796	0.00188
7	5	0.34	0.64	7.81	0.0618	0.00725	0.00211
7	6	0.335	0.745	7.82	0.0303	0.0057	0.000803
8	1	0.44	0.256	9.76	0.404	0.0871	0.0227
8	2	0.45	0.349	10.2	0.227	0.0336	0.00965
8	3	0.465	0.445	9.91	0.191	0.0224	0.0048
8	4	0.443	0.55	9.79	0.0999	0.0188	0.002
8	5	0.443	0.634	9.59	0.0346	0.0141	0.00181
8	6	0.459	0.745	10.8	-0.022	0.00689	0.00149

Table 7: CSB, VMD, radiative and acceptance corrected $m_p^{K^+}$ multiplicity results binned in z and x from the all years production.

xbin	zbin	$<x>$	$<z>$	$<Q^2>$	$m_p^{K^-}$	$\pm\sigma_{stat.}$	$\pm\sigma_{sys.}$
1	1	0.0351	0.256	1.29	0.168	0.00479	0.016
1	2	0.0352	0.363	1.28	0.101	0.00306	0.01
1	3	0.0344	0.455	1.24	0.0659	0.00311	0.00462
1	4	0.0342	0.552	1.21	0.0434	0.00258	0.0013
1	5	0.0334	0.629	1.13	0.0202	0.00261	0.00249
1	6	0.0309	0.741	1.11	-0.00465	0.00179	0.00335
2	1	0.0483	0.248	1.49	0.229	0.00521	0.00202
2	2	0.0482	0.351	1.51	0.0866	0.00258	0.00425
2	3	0.0474	0.448	1.44	0.055	0.00214	0.00364
2	4	0.0478	0.542	1.46	0.0394	0.0019	0.00205
2	5	0.0487	0.655	1.43	0.0167	0.00127	0.000757
2	6	0.0481	0.735	1.21	0.00613	0.00118	0.00382
3	1	0.0648	0.25	1.83	0.209	0.0048	0.0282
3	2	0.065	0.348	1.8	0.0995	0.00263	0.0111
3	3	0.0645	0.445	1.76	0.054	0.00187	0.00146
3	4	0.0645	0.554	1.74	0.0296	0.00141	0.00381
3	5	0.0649	0.643	1.71	0.015	0.00113	0.000233
3	6	0.0645	0.745	1.51	-0.000937	0.000804	0.00263
4	1	0.087	0.248	2.42	0.175	0.00486	0.0352
4	2	0.0871	0.346	2.18	0.0916	0.00269	0.0248
4	3	0.0872	0.451	2.21	0.0463	0.00181	0.00557
4	4	0.0873	0.545	2.17	0.032	0.00146	0.00546
4	5	0.0857	0.643	2.06	0.0152	0.00113	0.00404
4	6	0.0866	0.743	1.88	-0.00443	0.000875	0.00377
5	1	0.137	0.249	3.57	0.181	0.00353	0.0251
5	2	0.137	0.348	3.22	0.0768	0.00167	0.0126
5	3	0.137	0.445	3.14	0.0444	0.00117	0.00363
5	4	0.136	0.545	3.14	0.0192	0.000784	0.00249
5	5	0.137	0.645	3.19	0.0114	0.000682	0.00325
5	6	0.13	0.739	2.64	-0.000926	0.000493	0.000785
6	1	0.238	0.249	5.76	0.18	0.00868	0.0219
6	2	0.238	0.348	5.25	0.0888	0.00384	0.00679
6	3	0.236	0.445	5.25	0.0397	0.00224	0.0053
6	4	0.24	0.543	5.25	0.0209	0.00164	0.00188
6	5	0.24	0.639	5.2	0.00767	0.00129	0.00211
6	6	0.22	0.734	3.48	-0.00202	0.000911	0.000803
7	1	0.35	0.261	9.12	0.183	0.0204	0.0227
7	2	0.334	0.343	7.19	0.073	0.00821	0.00965
7	3	0.343	0.441	7.26	0.0392	0.00489	0.0048
7	4	0.338	0.545	7.16	0.0168	0.00331	0.002
7	5	0.334	0.632	7.47	-0.00257	0.00164	0.00181
7	6	0.326	0.759	6.07	-0.00544	0.000517	0.00149
8	1	0.449	0.246	10.1	0.325	0.0558	0.0126
8	2	0.462	0.345	10.7	0.138	0.0209	0.00846
8	3	0.441	0.445	9.16	-0.00287	0.00799	0.00266
8	4	0.447	0.547	11	0.0205	0.00859	0.00195
8	5	0.448	0.636	9.79	-0.00253	0.00117	0.00129
8	6	0.466	0.748	7.95	-0.00658	0.000628	0.000781

Table 8: CSB, VMD, radiative and acceptance corrected $m_p^{K^-}$ multiplicity results binned in z and x from the all years production.

xbin	zbin	$<x>$	$<z>$	$<Q^2>$	$m_d^{K^+}$	$\pm\sigma_{stat.}$	$\pm\sigma_{sys.}$
1	1	0.0357	0.263	1.31	0.262	0.00486	0.0143
1	2	0.0348	0.361	1.27	0.19	0.00363	0.0131
1	3	0.0346	0.462	1.25	0.143	0.00368	0.00549
1	4	0.034	0.555	1.23	0.127	0.0038	0.00304
1	5	0.0344	0.648	1.19	0.0667	0.003	0.00428
1	6	0.0359	0.741	1.14	0.0466	0.0038	0.00283
2	1	0.0486	0.251	1.49	0.329	0.00512	0.00957
2	2	0.0481	0.35	1.49	0.193	0.00331	0.00627
2	3	0.0481	0.453	1.47	0.125	0.00268	0.00336
2	4	0.0482	0.55	1.48	0.101	0.00253	0.00127
2	5	0.0475	0.645	1.4	0.0643	0.00224	0.00206
2	6	0.0479	0.744	1.33	0.0378	0.00178	0.00358
3	1	0.0654	0.252	1.83	0.334	0.00507	0.00428
3	2	0.0651	0.348	1.78	0.203	0.00313	0.00899
3	3	0.0652	0.45	1.78	0.127	0.00231	0.00286
3	4	0.065	0.549	1.76	0.0918	0.00207	0.000578
3	5	0.0648	0.646	1.73	0.0577	0.00181	0.000354
3	6	0.0652	0.748	1.64	0.0407	0.00161	0.0013
4	1	0.0868	0.251	2.35	0.301	0.00518	0.0181
4	2	0.087	0.348	2.18	0.182	0.00319	0.00913
4	3	0.087	0.447	2.15	0.12	0.00238	0.00576
4	4	0.0868	0.549	2.17	0.0933	0.00222	0.00403
4	5	0.0869	0.647	2.12	0.0658	0.00203	0.00274
4	6	0.0867	0.746	2.01	0.0315	0.00148	0.0009
5	1	0.137	0.251	3.55	0.296	0.00379	0.0355
5	2	0.138	0.348	3.24	0.191	0.00224	0.0227
5	3	0.137	0.447	3.17	0.128	0.00173	0.00541
5	4	0.138	0.547	3.18	0.0839	0.00149	0.00354
5	5	0.138	0.647	3.19	0.055	0.00131	0.00475
5	6	0.138	0.747	3.1	0.028	0.000941	0.00182
6	1	0.238	0.253	5.76	0.332	0.0103	0.0271
6	2	0.239	0.348	5.31	0.208	0.00552	0.0123
6	3	0.237	0.449	5.27	0.135	0.00387	0.00351
6	4	0.239	0.546	5.43	0.0935	0.00334	0.0025
6	5	0.237	0.645	5.31	0.0553	0.00269	0.00263
6	6	0.238	0.745	5.36	0.0308	0.00199	0.00316
7	1	0.335	0.258	7.72	0.32	0.0253	0.0193
7	2	0.338	0.35	7.43	0.228	0.0134	0.00876
7	3	0.338	0.446	7.27	0.149	0.00859	0.00182
7	4	0.338	0.548	7.53	0.0925	0.00715	0.00291
7	5	0.338	0.649	7.6	0.0539	0.00544	0.00192
7	6	0.333	0.743	7.66	-0.00647	0.00356	0.000364
8	1	0.382	0.337	12.2	0.255	0.0615	0.0138
8	2	0.45	0.351	10.7	0.266	0.0285	0.00766
8	3	0.445	0.446	9.77	0.147	0.0209	0.00567
8	4	0.446	0.546	10	0.0167	0.0116	0.00333
8	5	0.414	0.623	6.76	-0.00912	0.00967	0.002
8	6	0.453	0.748	9.79	0.0052	0.00768	0.000857

Table 9: CSB, VMD, radiative and acceptance corrected $m_d^{K^+}$ multiplicity results binned in z and x from the all years production.

xbin	zbin	$<x>$	$<z>$	$<Q^2>$	$m_d^{K^-}$	$\pm\sigma_{stat.}$	$\pm\sigma_{sys.}$
1	1	0.0344	0.254	1.26	0.169	0.00385	0.00957
1	2	0.0344	0.357	1.26	0.103	0.00262	0.00627
1	3	0.0343	0.456	1.23	0.0679	0.00242	0.00336
1	4	0.0342	0.55	1.22	0.0534	0.0025	0.00127
1	5	0.0351	0.648	1.19	0.0132	0.00164	0.00206
1	6	0.0335	0.763	1.37	0.00109	0.00267	0.00358
2	1	0.0483	0.248	1.49	0.215	0.00406	0.00428
2	2	0.048	0.35	1.49	0.095	0.00228	0.00899
2	3	0.0479	0.449	1.48	0.0609	0.0019	0.00286
2	4	0.0476	0.551	1.44	0.0401	0.00154	0.000578
2	5	0.0479	0.643	1.42	0.0216	0.00137	0.000354
2	6	0.0495	0.731	1.28	0.00564	0.00105	0.0013
3	1	0.0652	0.249	1.86	0.214	0.00407	0.0181
3	2	0.0652	0.35	1.79	0.101	0.00222	0.00913
3	3	0.0649	0.449	1.79	0.0543	0.00154	0.00576
3	4	0.0642	0.546	1.76	0.0331	0.00128	0.00403
3	5	0.064	0.644	1.7	0.0179	0.00111	0.00274
3	6	0.065	0.738	1.51	-0.00212	0.000862	0.0009
4	1	0.0873	0.25	2.38	0.176	0.00404	0.0355
4	2	0.0872	0.349	2.21	0.0851	0.00218	0.0227
4	3	0.087	0.448	2.16	0.0483	0.00144	0.00541
4	4	0.0869	0.547	2.12	0.0287	0.00128	0.00354
4	5	0.0863	0.642	2.12	0.0171	0.00106	0.00475
4	6	0.0873	0.742	2.01	-0.000229	0.000785	0.00182
5	1	0.136	0.25	3.53	0.175	0.00289	0.0271
5	2	0.137	0.347	3.23	0.0843	0.00151	0.0123
5	3	0.136	0.445	3.12	0.0428	0.000943	0.00351
5	4	0.136	0.546	3.12	0.0235	0.000773	0.0025
5	5	0.137	0.644	3.02	0.0129	0.000619	0.00263
5	6	0.129	0.741	2.83	-0.00202	0.000441	0.00316
6	1	0.24	0.25	5.83	0.193	0.00779	0.0193
6	2	0.237	0.347	5.18	0.0934	0.00335	0.00876
6	3	0.236	0.442	5.08	0.0427	0.00205	0.00182
6	4	0.239	0.541	5.18	0.0165	0.00127	0.00291
6	5	0.242	0.642	5.61	0.00897	0.0012	0.00192
6	6	0.232	0.748	4.75	-0.00104	0.000739	0.000364
7	1	0.346	0.249	7.67	0.209	0.0195	0.0138
7	2	0.34	0.347	7.51	0.0952	0.00841	0.00766
7	3	0.331	0.443	7.17	0.0389	0.0044	0.00567
7	4	0.333	0.542	6.96	0.0126	0.00293	0.00333
7	5	0.336	0.634	7.22	0.00043	0.00158	0.002
7	6	0.325	0.741	6.93	-0.00452	0.0011	0.000857
8	1	0.442	0.251	9.94	0.24	0.0416	0.00972
8	2	0.443	0.345	9.87	0.102	0.0193	0.00846
8	3	0.437	0.446	9.8	-0.00882	0.00759	0.00656
8	4	0.435	0.538	9.48	-0.0177	0.00298	0.000889
8	5	0.451	0.657	9.35	-0.00678	0.000604	0.00171
8	6	0.455	0.749	9.99	-0.00352	0.000297	0.000575

Table 10: CSB, VMD, radiative and acceptance corrected $m_d^{K^-}$ multiplicity results binned in z and x from the all years production.

xbin	zbin	$<x>$	$<z>$	$<Q^2>$	m_p^p	$\pm\sigma_{stat.}$	$\pm\sigma_{sys.}$
1	1	0.0356	0.266	1.31	0.269	0.00673	0.00202
1	2	0.0345	0.358	1.24	0.235	0.00467	0.00425
1	3	0.0343	0.453	1.21	0.159	0.00468	0.00364
1	4	0.0343	0.549	1.2	0.0848	0.00402	0.00205
1	5	0.0343	0.644	1.21	0.0286	0.00242	0.000757
1	6	0.0341	0.738	1.17	0.0141	0.00232	0.00382
2	1	0.0492	0.256	1.52	0.244	0.009	0.0282
2	2	0.0487	0.355	1.5	0.213	0.00472	0.0111
2	3	0.0479	0.45	1.44	0.141	0.00364	0.00146
2	4	0.0485	0.55	1.41	0.0843	0.00284	0.00381
2	5	0.0483	0.65	1.38	0.0415	0.00194	0.000233
2	6	0.0485	0.738	1.35	0.00931	0.00143	0.00263
3	1	0.0652	0.254	1.78	0.363	0.0136	0.0352
3	2	0.0652	0.35	1.72	0.273	0.00615	0.0248
3	3	0.0651	0.447	1.7	0.175	0.00379	0.00557
3	4	0.0649	0.546	1.65	0.0974	0.0027	0.00546
3	5	0.0654	0.646	1.6	0.0414	0.00172	0.00404
3	6	0.0639	0.739	1.47	0.0116	0.0011	0.00377
4	1	0.0869	0.255	2.23	0.644	0.0232	0.0251
4	2	0.0868	0.348	2.01	0.404	0.0104	0.0126
4	3	0.0875	0.447	2	0.225	0.00529	0.00363
4	4	0.0878	0.547	1.99	0.101	0.00329	0.00249
4	5	0.0869	0.645	1.89	0.0498	0.00227	0.00325
4	6	0.0876	0.742	1.78	0.0134	0.00123	0.000785
5	1	0.139	0.252	3.37	0.739	0.0174	0.0219
5	2	0.14	0.35	2.92	0.514	0.00842	0.00679
5	3	0.139	0.445	2.84	0.266	0.00442	0.0053
5	4	0.14	0.545	2.87	0.141	0.00287	0.00188
5	5	0.139	0.643	2.87	0.0604	0.00171	0.00211
5	6	0.137	0.744	2.62	0.0161	0.000863	0.000803
6	1	0.243	0.252	5.43	0.831	0.03	0.0227
6	2	0.24	0.348	4.67	0.501	0.0143	0.00965
6	3	0.24	0.445	4.8	0.265	0.00832	0.0048
6	4	0.239	0.545	5.04	0.139	0.00522	0.002
6	5	0.239	0.642	5	0.0562	0.00328	0.00181
6	6	0.237	0.743	4.78	0.0184	0.00158	0.00149
7	1	0.342	0.253	7.41	0.992	0.0523	0.0126
7	2	0.341	0.345	6.5	0.523	0.0276	0.00846
7	3	0.337	0.443	6.66	0.221	0.0151	0.00266
7	4	0.338	0.545	7.5	0.143	0.0107	0.00195
7	5	0.338	0.646	7	0.0665	0.00682	0.00129
7	6	0.318	0.734	7.61	0.0193	0.00356	0.000781
8	1	0.452	0.25	9.79	1.08	0.0853	0.0103
8	2	0.452	0.34	9.27	0.427	0.0452	0.00648
8	3	0.445	0.444	9.59	0.153	0.0214	0.00737
8	4	0.46	0.539	9.98	0.11	0.0167	0.00493
8	5	0.44	0.646	9.74	0.0569	0.0132	0.000451
8	6	0.441	0.738	10.2	-0.00235	0.0067	0.00155

Table 11: CSB, VMD, radiative and acceptance corrected m_p^p multiplicity results binned in z and x from the all years production.

xbin	zbin	$<x>$	$<z>$	$<Q^2>$	$m_p^{\bar{p}}$	$\pm\sigma_{stat.}$	$\pm\sigma_{sys.}$
1	1	0.0337	0.262	1.28	0.0656	0.00385	0.0282
1	2	0.0336	0.347	1.22	0.0631	0.00271	0.0111
1	3	0.0337	0.442	1.21	0.0393	0.00264	0.00146
1	4	0.0367	0.583	1.35	0.00881	0.00213	0.00381
1	5	0.0468	0.9	1.65	0.00349	0.000994	0.000233
1	6	0.0367	0.748	1.2	0.000215	0.000872	0.00263
2	1	0.0484	0.256	1.74	0.0436	0.00445	0.0352
2	2	0.0485	0.352	1.59	0.0401	0.00212	0.0248
2	3	0.0496	0.46	1.58	0.022	0.00145	0.00557
2	4	0.0476	0.558	1.35	0.00828	0.0012	0.00546
2	5	0.0482	0.636	1.44	0.00209	0.000793	0.00404
2	6	0.0493	0.749	1.5	-0.0015	0.000608	0.00377
3	1	0.0653	0.252	2.06	0.0352	0.00405	0.0251
3	2	0.0646	0.347	1.99	0.0303	0.0021	0.0126
3	3	0.0642	0.447	1.85	0.0142	0.00106	0.00363
3	4	0.0624	0.52	1.73	0.00681	0.000778	0.00249
3	5	0.0707	0.647	1.87	0.00194	0.000491	0.00325
3	6	0.0687	0.725	1.78	7.93e-05	0.000331	0.000785
4	1	0.0856	0.254	2.57	0.0406	0.0043	0.0219
4	2	0.0868	0.343	2.63	0.0259	0.00208	0.00679
4	3	0.0866	0.44	2.39	0.0105	0.00101	0.0053
4	4	0.0838	0.542	2.2	0.00299	0.000662	0.00188
4	5	0.0746	0.635	0.444	0.0027	0.000581	0.00211
4	6	0.0867	0.706	1.99	-0.000641	0.000247	0.000803
5	1	0.139	0.255	3.83	0.0404	0.00311	0.0227
5	2	0.14	0.346	3.66	0.0215	0.00134	0.00965
5	3	0.131	0.439	3.39	0.00996	0.000752	0.0048
5	4	0.136	0.541	3.61	0.0043	0.000502	0.002
5	5	0.142	0.641	3.26	0.000636	0.000306	0.00181
5	6	0.205	0.745	4.22	1.3e-05	0.000134	0.00149
6	1	0.244	0.238	6	0.0594	0.00834	0.0126
6	2	0.243	0.335	5.56	0.0287	0.00374	0.00846
6	3	0.242	0.441	5.96	0.0135	0.00166	0.00266
6	4	0.252	0.495	8.5	0.00175	0.000903	0.00195
6	5	0.352	0.603	3.92	0.00141	0.000522	0.00129
6	6	0.238	0.751	5.28	-0.000187	7.54e-05	0.000781
7	1	0.339	0.241	7.66	0.0804	0.0205	0.0103
7	2	0.365	0.322	7.8	0.0271	0.00864	0.00648
7	3	0.193	0.256	-6.92	0.0095	0.00385	0.00737
7	4	0.32	0.563	7.88	-0.00413	0.000946	0.00493
7	5	0.359	0.653	9.08	1.76e-05	0.000221	0.000451
7	6	0.338	0.762	7.95	-0.000618	0.000283	0.00155
8	1	0.385	0.347	2.37	0.0971	0.0446	0.0287
8	2	0.469	0.37	14.2	-0.011	0.01	0.0194
8	3	0.43	0.441	10.2	-0.0111	0.00389	0.00658
8	4	0.439	0.542	10.6	-0.00177	0.000593	0.00282
8	5	0.451	0.642	10.2	0.000436	0.000225	0.0047
8	6	0.457	0.735	8.56	-0.00034	2.62e-05	0.000268

Table 12: CSB, VMD, radiative and acceptance corrected $m_p^{\bar{p}}$ multiplicity results binned in z and x from the all years production.

xbin	zbin	$<x>$	$<z>$	$<Q^2>$	m_d^p	$\pm\sigma_{stat.}$	$\pm\sigma_{sys.}$
1	1	0.0355	0.266	1.3	0.25	0.00531	0.00428
1	2	0.0351	0.361	1.26	0.22	0.00378	0.00899
1	3	0.0345	0.45	1.22	0.136	0.00346	0.00286
1	4	0.0345	0.55	1.18	0.0758	0.00341	0.000578
1	5	0.0339	0.645	1.21	0.0296	0.00204	0.000354
1	6	0.0398	0.784	1.05	0.00935	0.00154	0.0013
2	1	0.0491	0.255	1.53	0.259	0.00697	0.0181
2	2	0.0486	0.354	1.48	0.218	0.00384	0.00913
2	3	0.0482	0.449	1.43	0.136	0.00274	0.00576
2	4	0.0479	0.546	1.37	0.0804	0.00224	0.00403
2	5	0.0482	0.641	1.37	0.0351	0.00156	0.00274
2	6	0.0477	0.739	1.32	0.00803	0.000896	0.0009
3	1	0.0656	0.254	1.79	0.393	0.0111	0.0355
3	2	0.0651	0.349	1.71	0.252	0.00498	0.0227
3	3	0.0651	0.448	1.72	0.152	0.00288	0.00541
3	4	0.0649	0.545	1.63	0.0798	0.00206	0.00354
3	5	0.0654	0.649	1.59	0.0386	0.00133	0.00475
3	6	0.0652	0.739	1.51	0.0145	0.000937	0.00182
4	1	0.0876	0.255	2.3	0.635	0.0198	0.0271
4	2	0.0873	0.35	2.05	0.431	0.0085	0.0123
4	3	0.0874	0.447	2.01	0.206	0.00443	0.00351
4	4	0.0876	0.546	1.99	0.0958	0.00282	0.0025
4	5	0.0868	0.644	1.89	0.0483	0.00188	0.00263
4	6	0.0873	0.741	1.74	0.0167	0.00112	0.00316
5	1	0.14	0.253	3.42	0.786	0.0146	0.0193
5	2	0.14	0.349	2.95	0.541	0.00703	0.00876
5	3	0.139	0.446	2.87	0.253	0.00357	0.00182
5	4	0.139	0.545	2.89	0.128	0.0022	0.00291
5	5	0.138	0.645	2.82	0.056	0.00137	0.00192
5	6	0.138	0.742	2.65	0.0168	0.000741	0.000364
6	1	0.243	0.25	5.54	0.873	0.0265	0.0138
6	2	0.24	0.348	4.77	0.481	0.0123	0.00766
6	3	0.238	0.445	4.78	0.247	0.00679	0.00567
6	4	0.238	0.545	4.92	0.152	0.00494	0.00333
6	5	0.239	0.644	4.94	0.0506	0.0027	0.002
6	6	0.241	0.743	4.81	0.0164	0.00135	0.000857
7	1	0.343	0.254	7.36	0.83	0.0443	0.00972
7	2	0.34	0.343	6.58	0.507	0.0239	0.00846
7	3	0.341	0.445	6.97	0.267	0.0134	0.00656
7	4	0.339	0.547	7.2	0.131	0.00873	0.000889
7	5	0.34	0.644	7.66	0.0482	0.00536	0.00171
7	6	0.336	0.744	6.69	0.0255	0.00343	0.000575
8	1	0.454	0.25	9.62	1.17	0.0806	0.0189
8	2	0.451	0.342	9.29	0.459	0.0411	0.00842
8	3	0.457	0.445	9.94	0.168	0.0232	0.00116
8	4	0.449	0.543	9.54	0.129	0.0178	0.000257
8	5	0.448	0.649	9.85	0.0408	0.0107	0.000469
8	6	0.455	0.751	10.3	-0.0143	0.00486	0.000791

Table 13: CSB, VMD, radiative and acceptance corrected m_d^p multiplicity results binned in z and x from the all years production.

xbin	zbin	$<x>$	$<z>$	$<Q^2>$	$m_d^{\bar{p}}$	$\pm\sigma_{stat.}$	$\pm\sigma_{sys.}$
1	1	0.0337	0.263	1.29	0.0707	0.00306	0.0181
1	2	0.0335	0.35	1.22	0.0572	0.00209	0.00913
1	3	0.0346	0.451	1.25	0.0287	0.00195	0.00576
1	4	0.0333	0.531	1.15	0.0128	0.00152	0.00403
1	5	0.0341	0.645	1.17	0.00442	0.000977	0.00274
1	6	0.0365	0.736	1.14	6.76e-05	0.000272	0.0009
2	1	0.048	0.253	1.66	0.043	0.0035	0.0355
2	2	0.0478	0.348	1.55	0.0423	0.00167	0.0227
2	3	0.0478	0.447	1.52	0.0255	0.00146	0.00541
2	4	0.047	0.54	1.41	0.00929	0.000964	0.00354
2	5	0.0467	0.639	1.41	0.00439	0.00066	0.00475
2	6	0.0408	0.722	1.39	0.000373	0.000387	0.00182
3	1	0.064	0.257	2.08	0.0404	0.00363	0.0271
3	2	0.064	0.344	1.98	0.029	0.00153	0.0123
3	3	0.065	0.448	1.9	0.0159	0.00101	0.00351
3	4	0.0649	0.547	1.86	0.00776	0.000786	0.0025
3	5	0.0683	0.643	1.67	0.00232	0.000533	0.00263
3	6	0.058	0.732	1.4	-0.000337	0.000384	0.00316
4	1	0.0859	0.257	2.66	0.0343	0.0033	0.0193
4	2	0.0869	0.346	2.44	0.0267	0.00171	0.00876
4	3	0.0864	0.445	2.46	0.0115	0.000872	0.00182
4	4	0.0856	0.543	2.35	0.0058	0.000662	0.00291
4	5	0.0899	0.671	2.4	0.00141	0.000467	0.00192
4	6	0.0917	0.752	2.27	-0.000567	0.000282	0.000364
5	1	0.137	0.253	3.91	0.0394	0.00252	0.0138
5	2	0.135	0.346	3.53	0.0257	0.00124	0.00766
5	3	0.136	0.441	3.54	0.00945	0.00059	0.00567
5	4	0.135	0.54	3.39	0.00692	0.000472	0.00333
5	5	0.132	0.635	3.38	0.00151	0.000315	0.002
5	6	0.145	0.741	3.27	-0.000164	0.000127	0.000857
6	1	0.236	0.251	6.12	0.0594	0.00757	0.00972
6	2	0.216	0.35	7.02	0.0176	0.00304	0.00846
6	3	0.239	0.448	7.34	0.0107	0.00145	0.00656
6	4	0.256	0.541	7.05	0.0039	0.000823	0.000889
6	5	0.255	0.65	5.66	-0.000165	0.000498	0.00171
6	6	0.233	0.742	5.71	-0.000459	0.000245	0.000575
7	1	0.362	0.239	11.9	0.0622	0.0156	0.0189
7	2	0.368	0.108	4.44	0.0219	0.00719	0.00842
7	3	0.341	0.449	8	0.00575	0.00264	0.00116
7	4	0.343	0.521	8.29	-0.00262	0.000853	0.000257
7	5	0.335	0.643	7.85	-0.000461	0.000489	0.000469
7	6	0.38	1.05	99.3	-0.000121	0.000109	0.000791
8	1	0.484	0.246	10.9	-0.00934	0.0314	0.0253
8	2	0.258	0.327	-3.33	-0.0123	0.00717	0.019
8	3	0.439	0.429	9.93	-0.001	0.00126	0.00945
8	4	0.426	0.547	10.1	-0.000405	0.000739	0.00501
8	5	0.446	0.655	9.93	-0.00237	0.000107	0.00442
8	6	0.498	0.806	13.5	-6.52e-05	9.24e-05	0.000363

Table 14: CSB, VMD, radiative and acceptance corrected $m_d^{\bar{p}}$ multiplicity results binned in z and x from the all years production.

C   Fragmentation Studies

This appendix provides the results from fragmentation studies performed using the HERMES LUND string model based Monte Carlo generator. These studies are an attempt to quantify the validity of the fragmentation symmetries that are assumed in this analysis. Here we show that the symmetries are broken in the HERMES MC between valence quarks as well as sea quarks at the 5-20% level. Kinematic scans in invariant mass (W^2) and Bjorken-x also reveal symmetry violations of a similar magnitude. Finally, we demonstrate that the universality of the symmetries is violated by comparing favored fragmentation functions from Deuterium and Hydrogen targets.
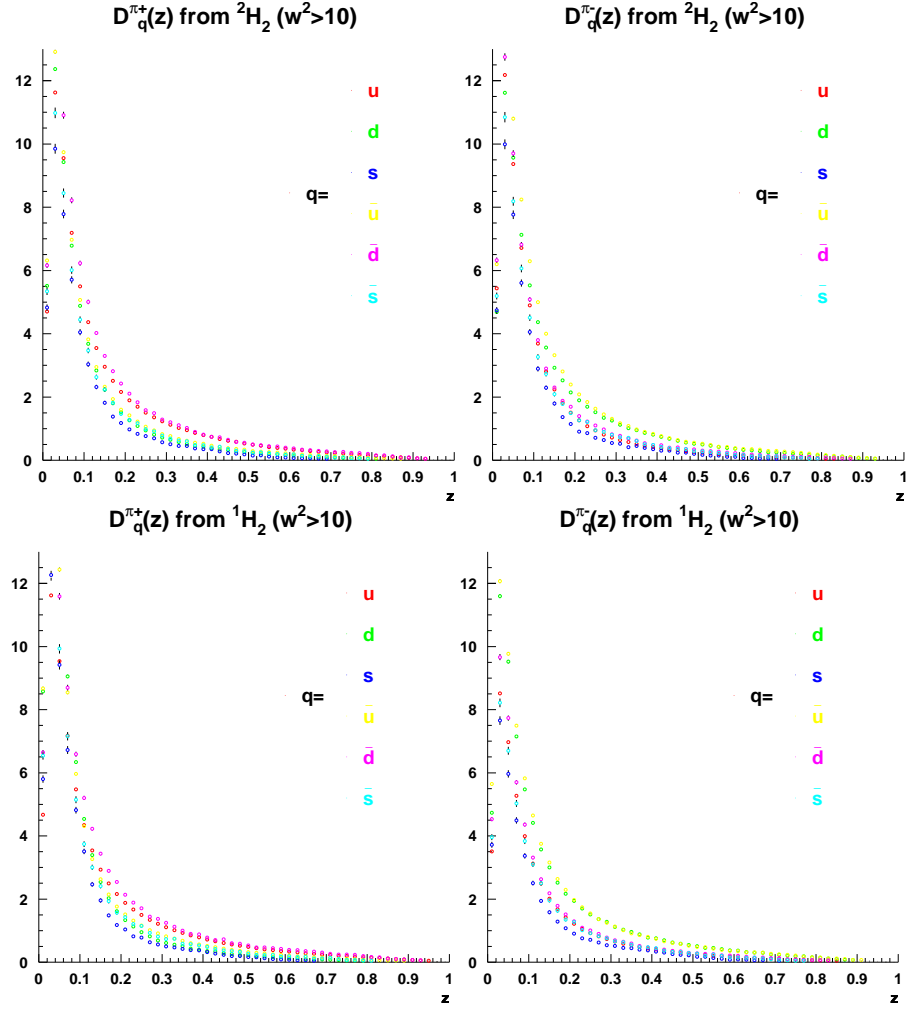
Figure 4: Charged pion fragmentation functions for a Deuterium target (top) and a Hydrogen target (bottom) extracted from the HERMES MC generator for quarks and anti-quarks.
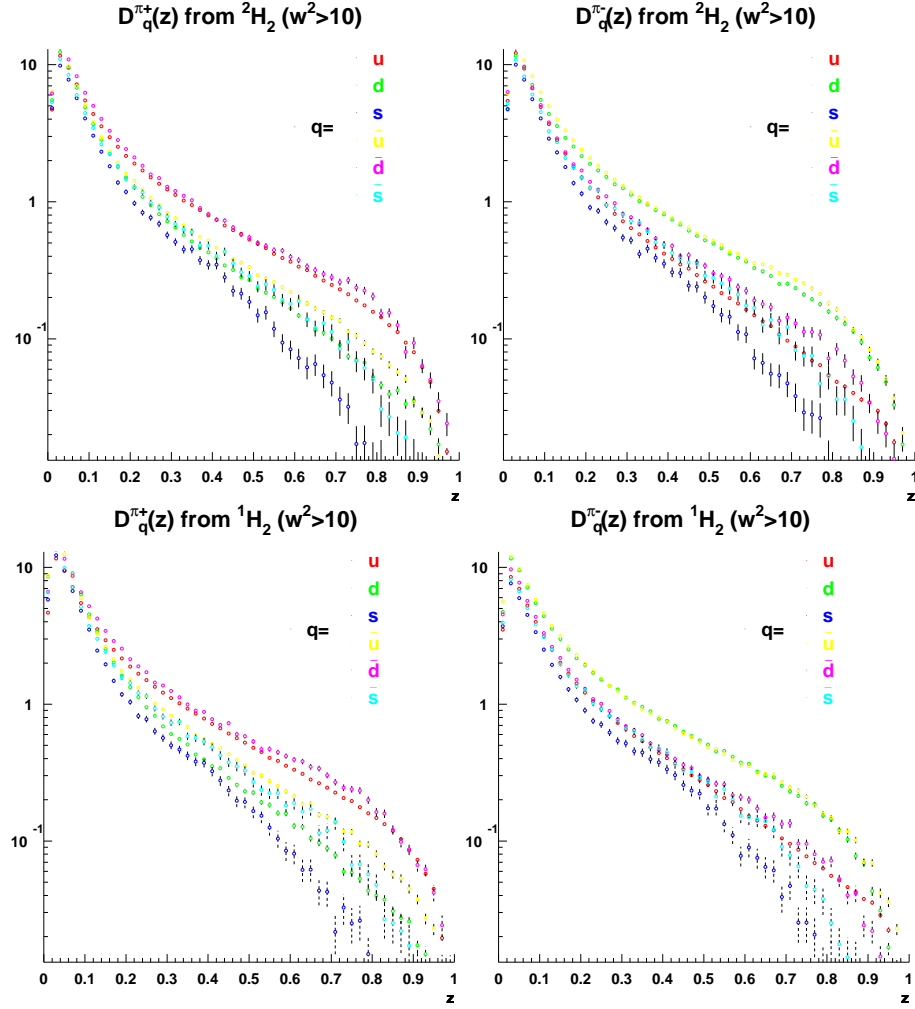
Figure 5: Charged pion fragmentation functions plotted with an logarithmic ordinate axis for a Deuterium target (top) and a Hydrogen target (bottom) extracted from the HERMES MC generator for quarks and anti-quarks.
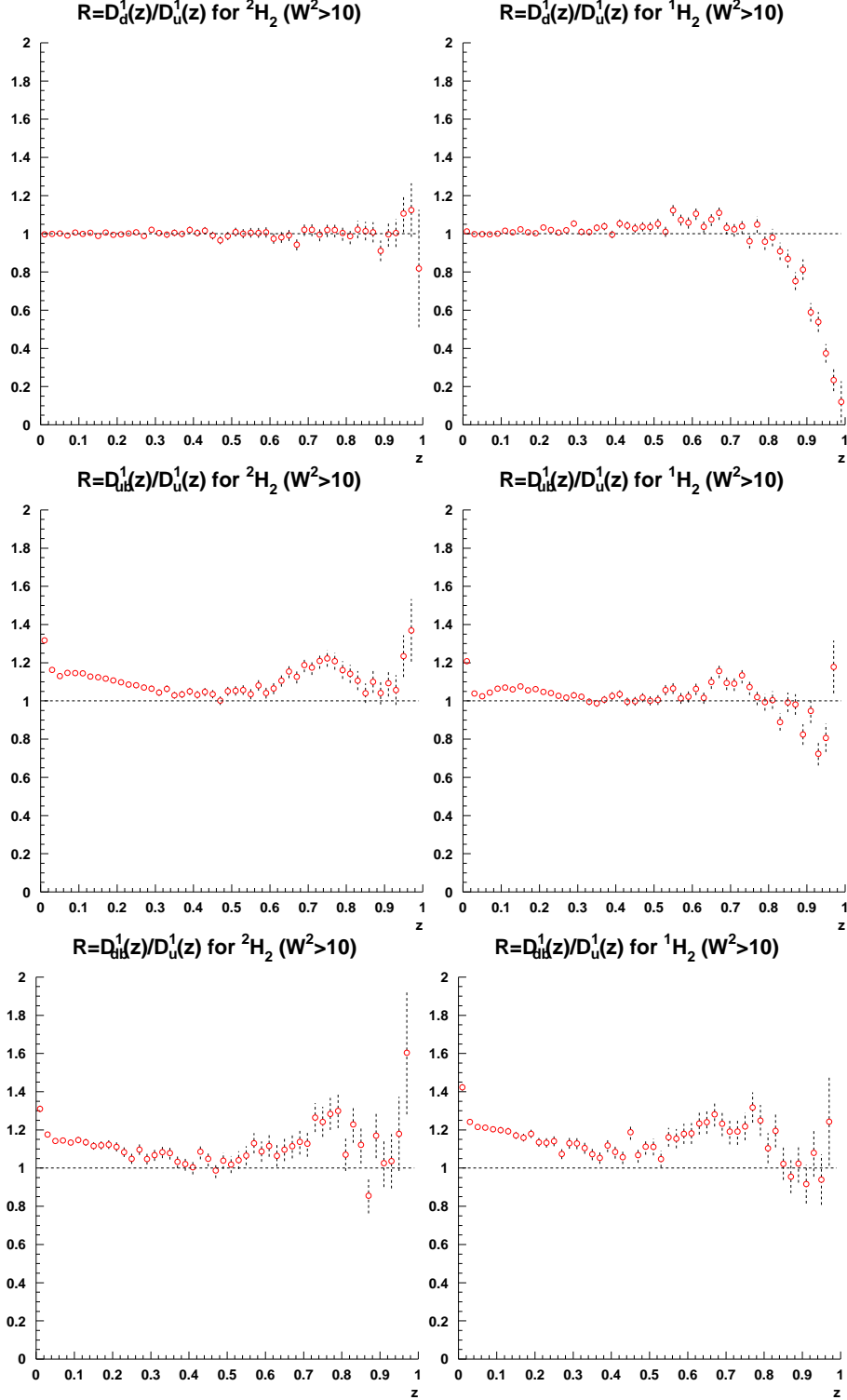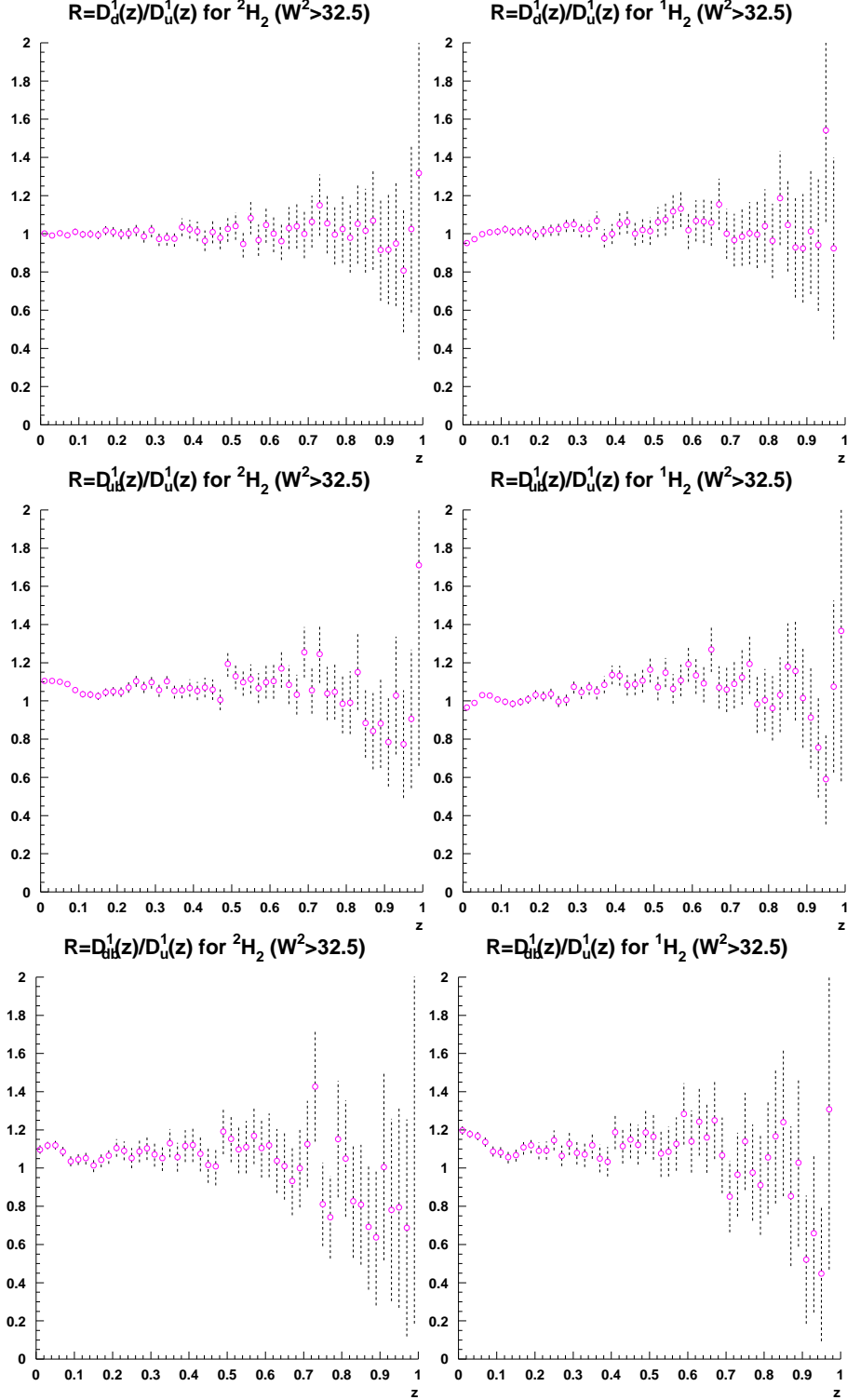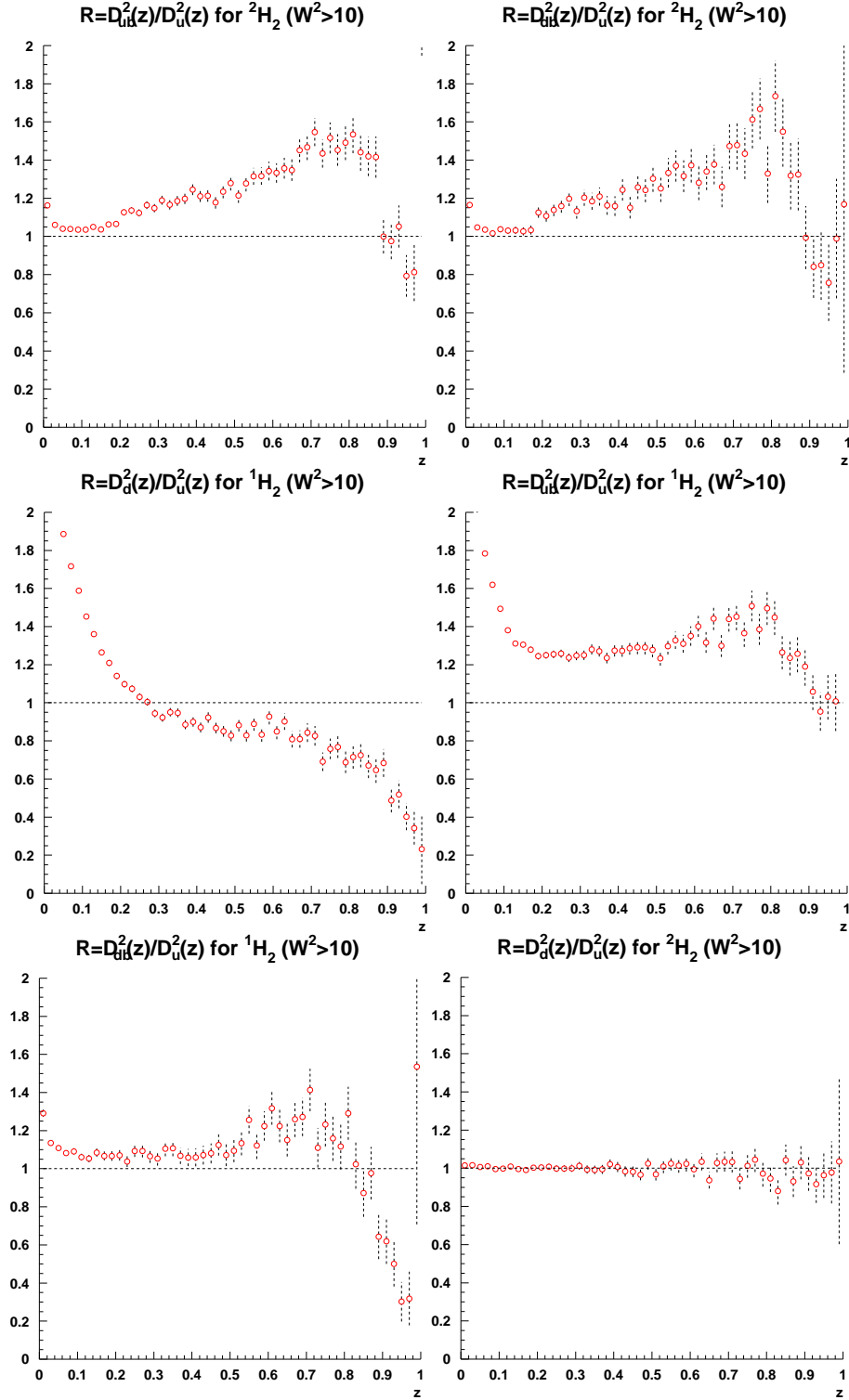
Figure 6: Ratios of charged pion favored fragmentation functions for a Deuterium target (left column) and Hydrogen target (right column) for light quarks with $W^2 > 10$.
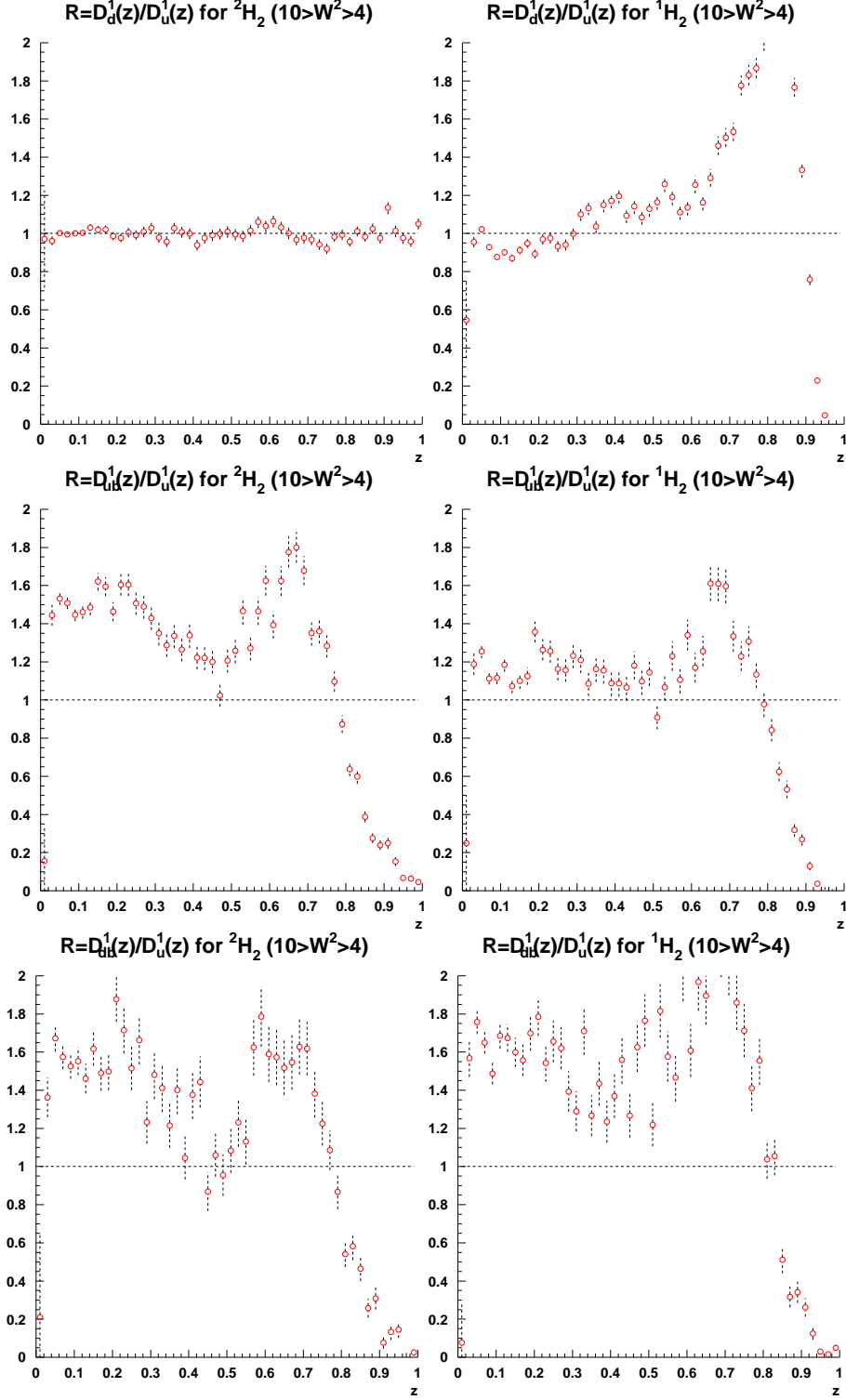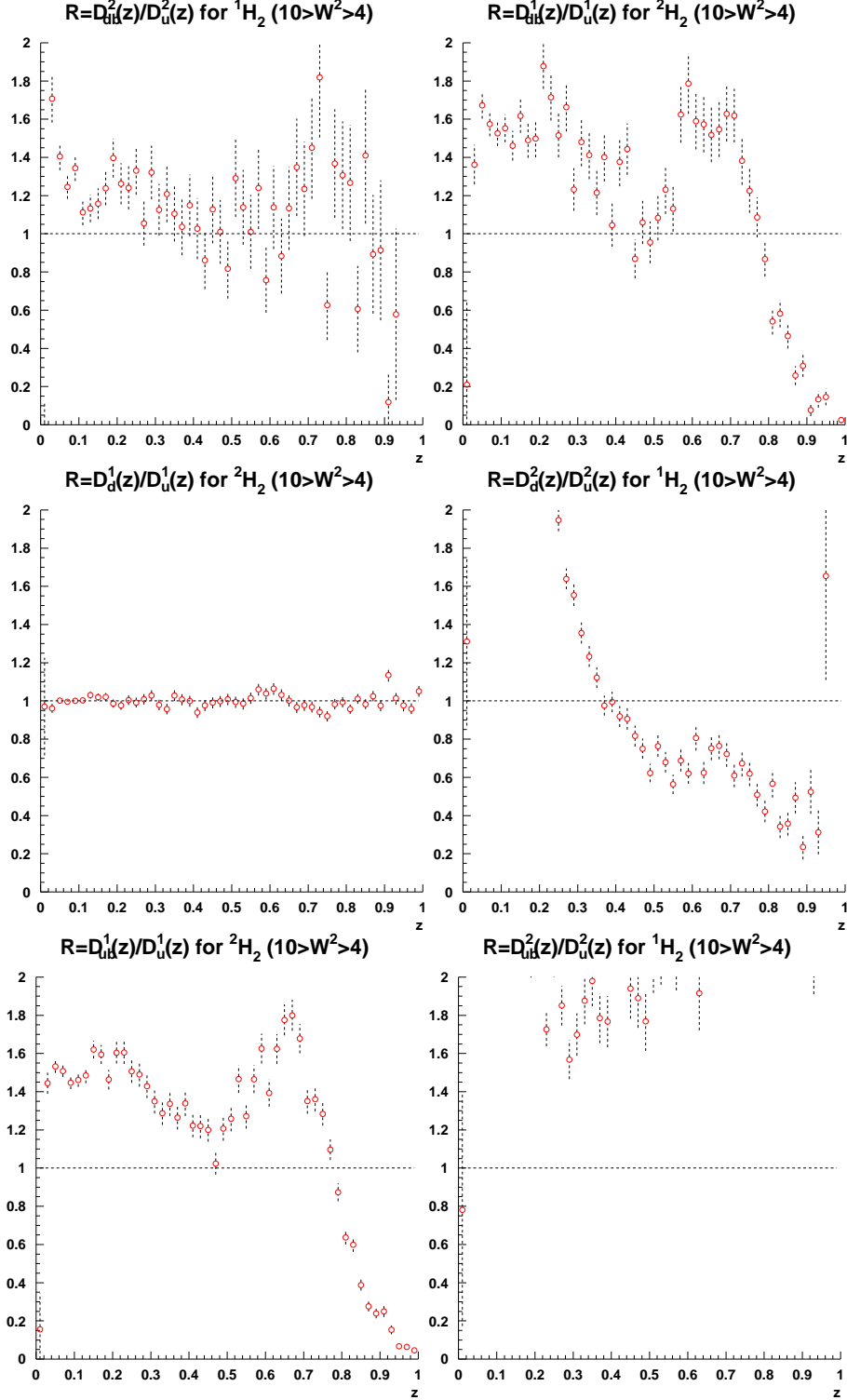
Figure 7: Ratios of charged pion favored fragmentation functions for a Deuterium target (left column) and Hydrogen target (right column) for light quarks with $10 > W^2 > 4$.

113
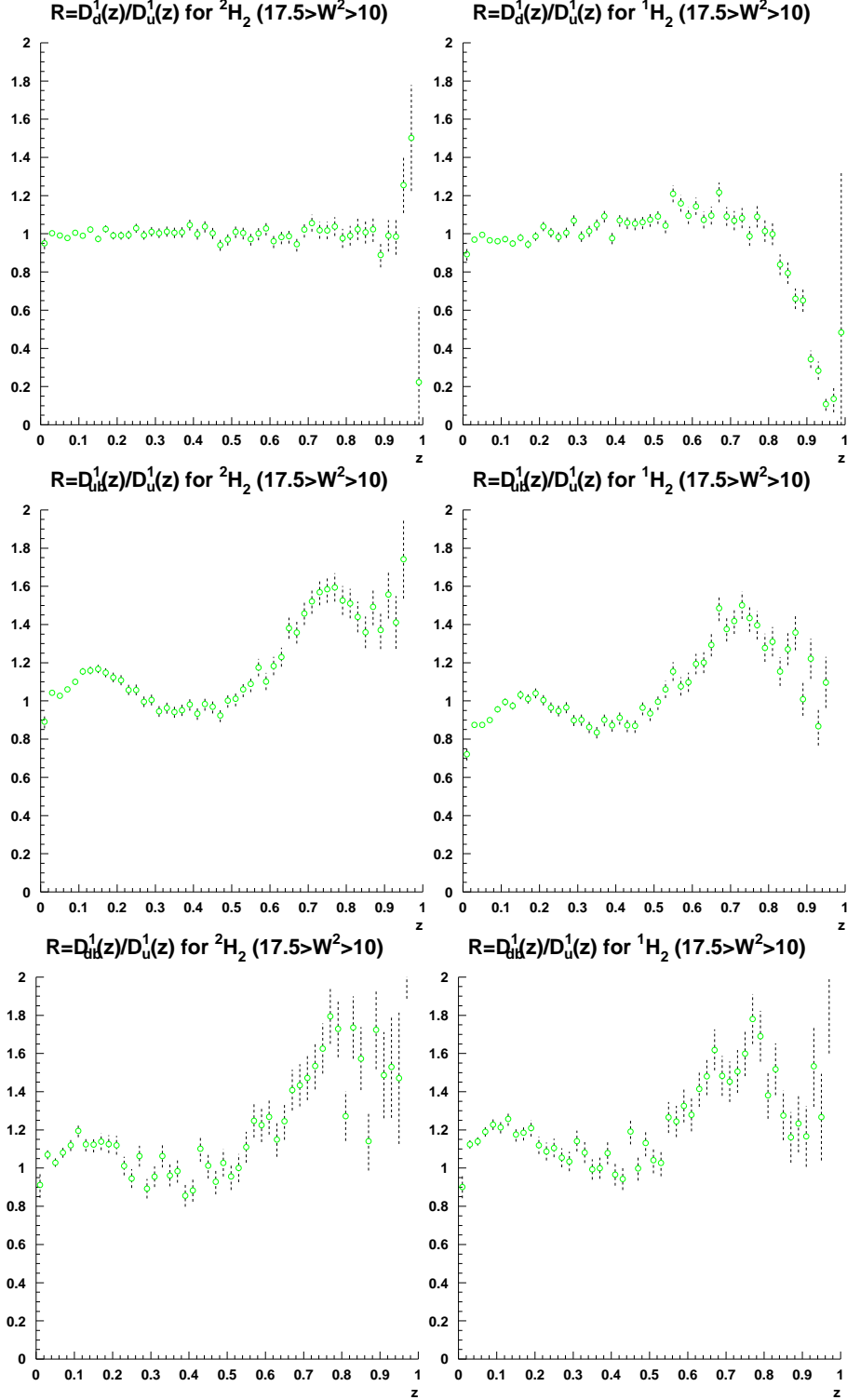
Figure 8: Ratios of charged pion favored fragmentation functions for a Deuterium target (left column) and Hydrogen target (right column) for light quarks with $17.5 > W^2 > 10$.
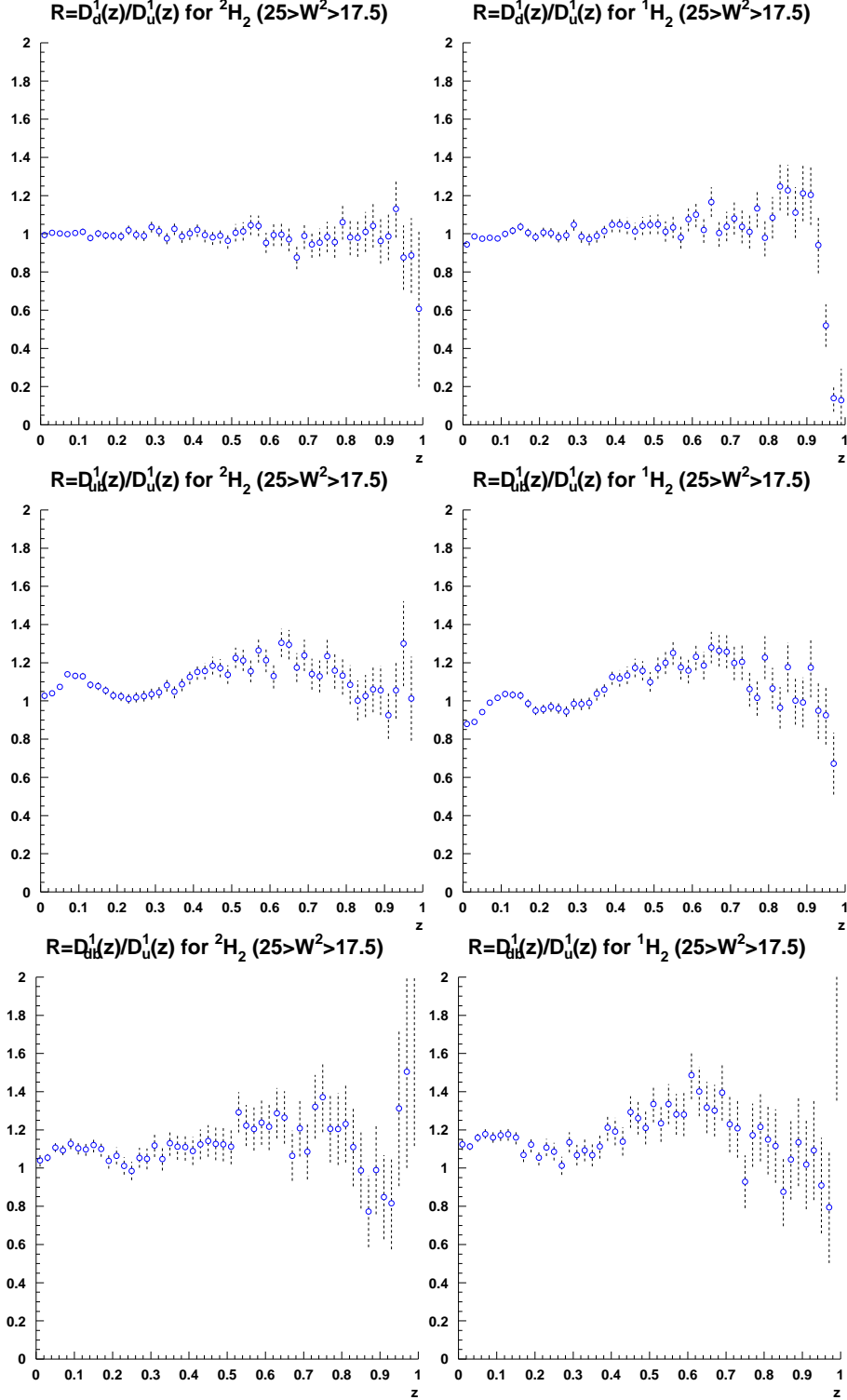
Figure 9: Ratios of charged pion favored fragmentation functions for a Deuterium target (left column) and Hydrogen target (right column) for light quarks with $25 > W^2 > 17.5$.
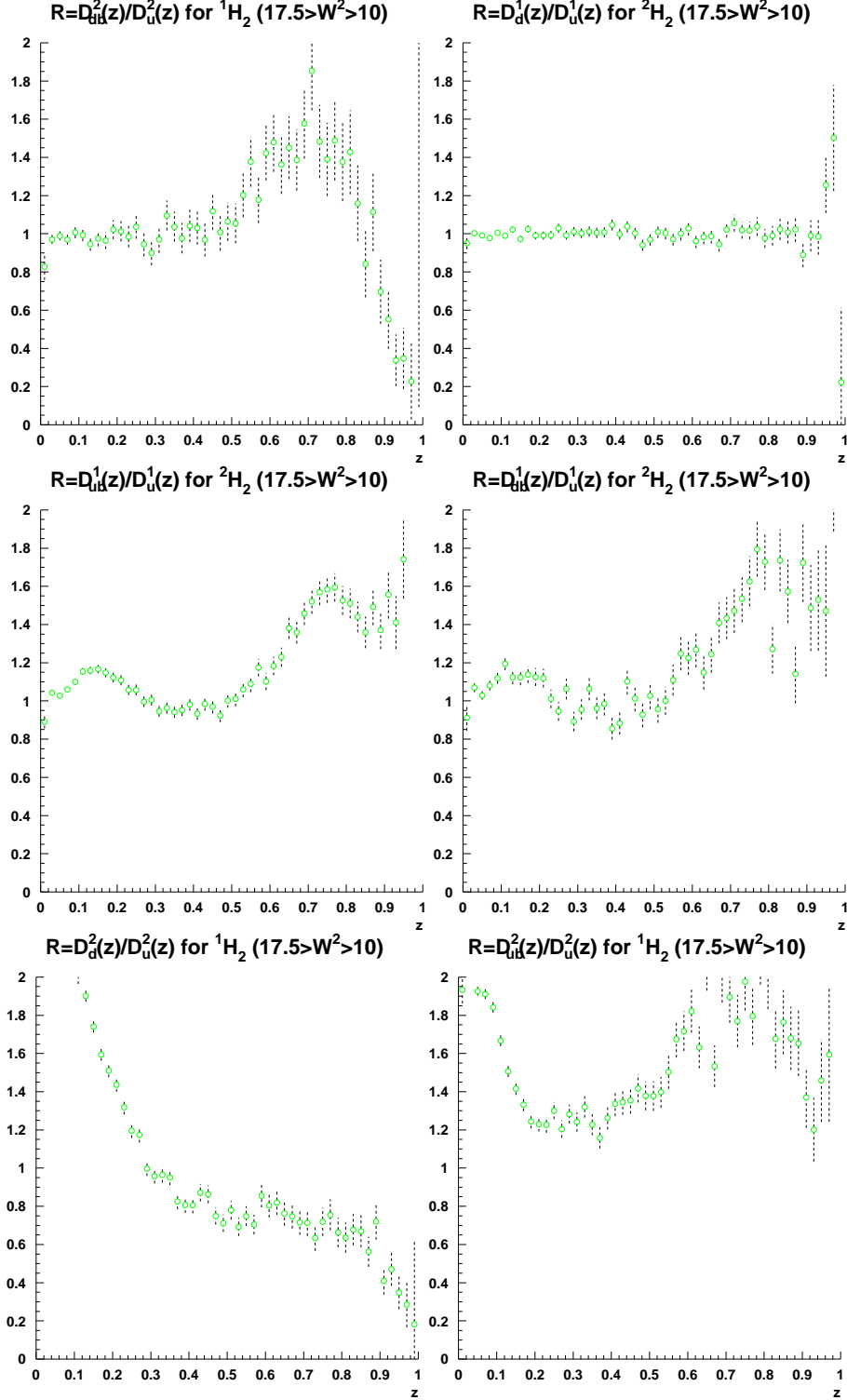
115
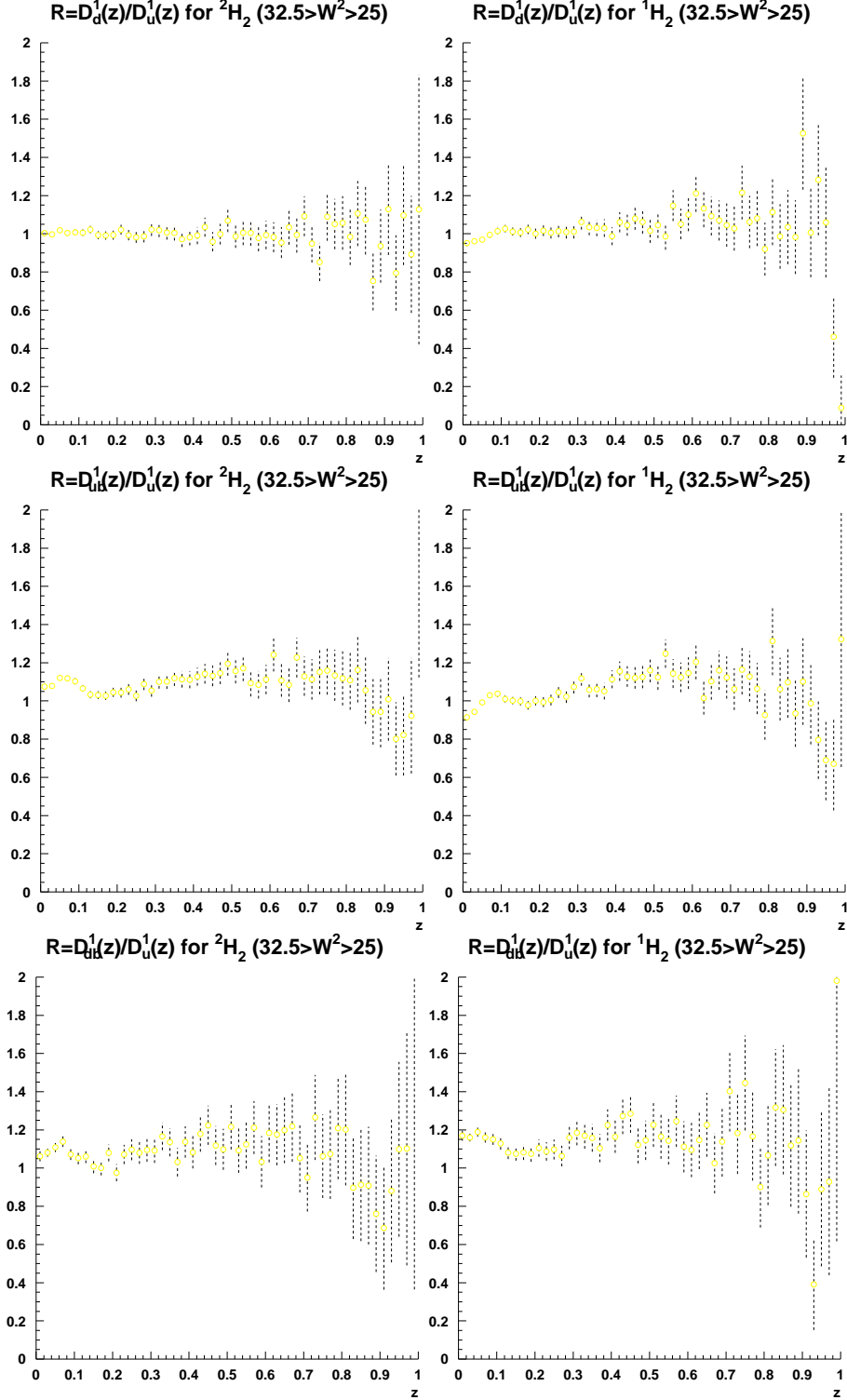
Figure 10: Ratios of charged pion favored fragmentation functions for a Deuterium target (left column) and Hydrogen target (right column) for light quarks with $32.5 > W^2 > 25$.

116

Figure 11: Ratios of charged pion favored fragmentation functions for a Deuterium target (left column) and Hydrogen target (right column) for light quarks with $W^2 > 32.5$.
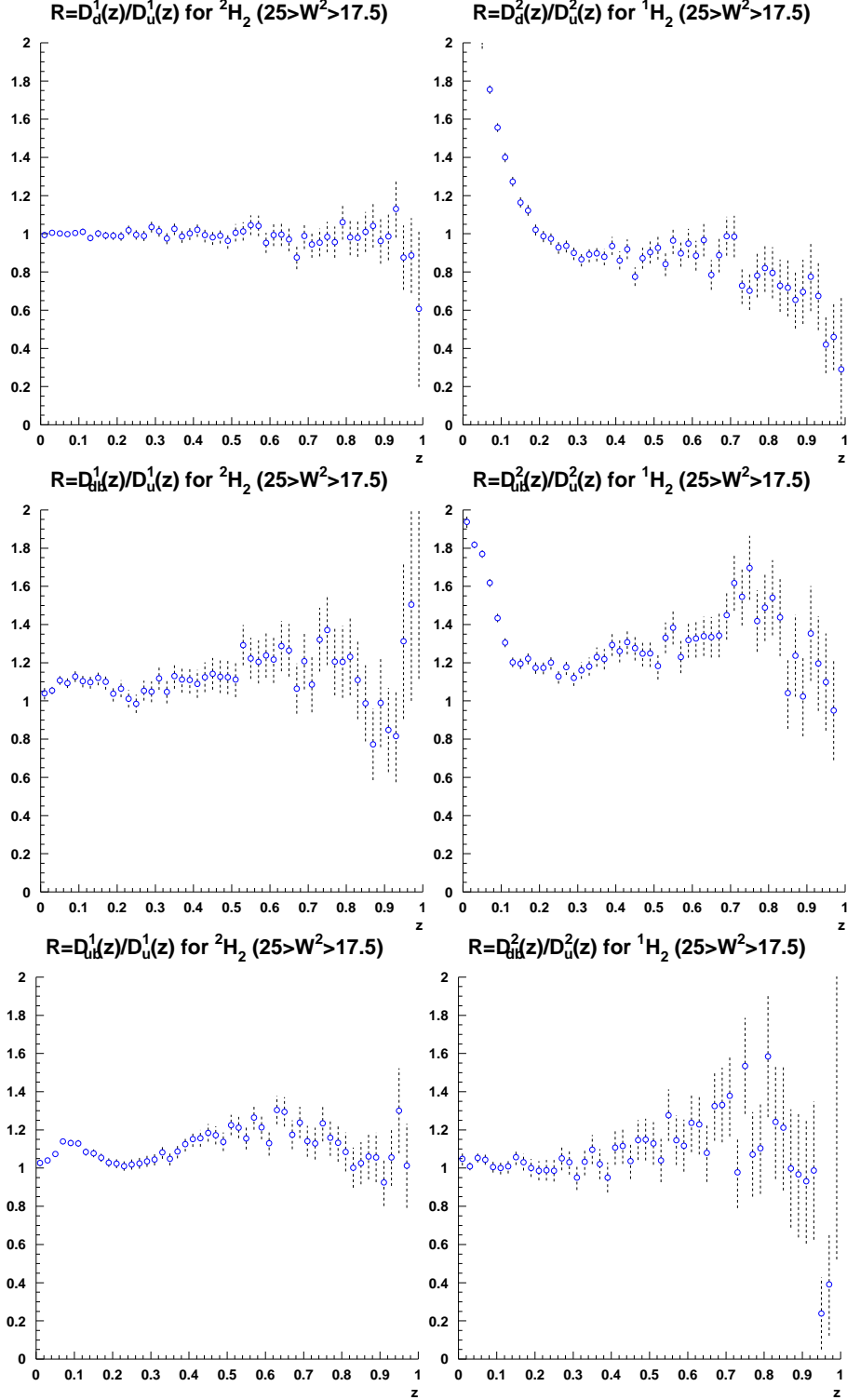
Figure 12: Ratios of charged pion favored fragmentation functions for a Deuterium target (left column) and Hydrogen target (right column) for light quarks with $25 > W^2 > 17.5$.
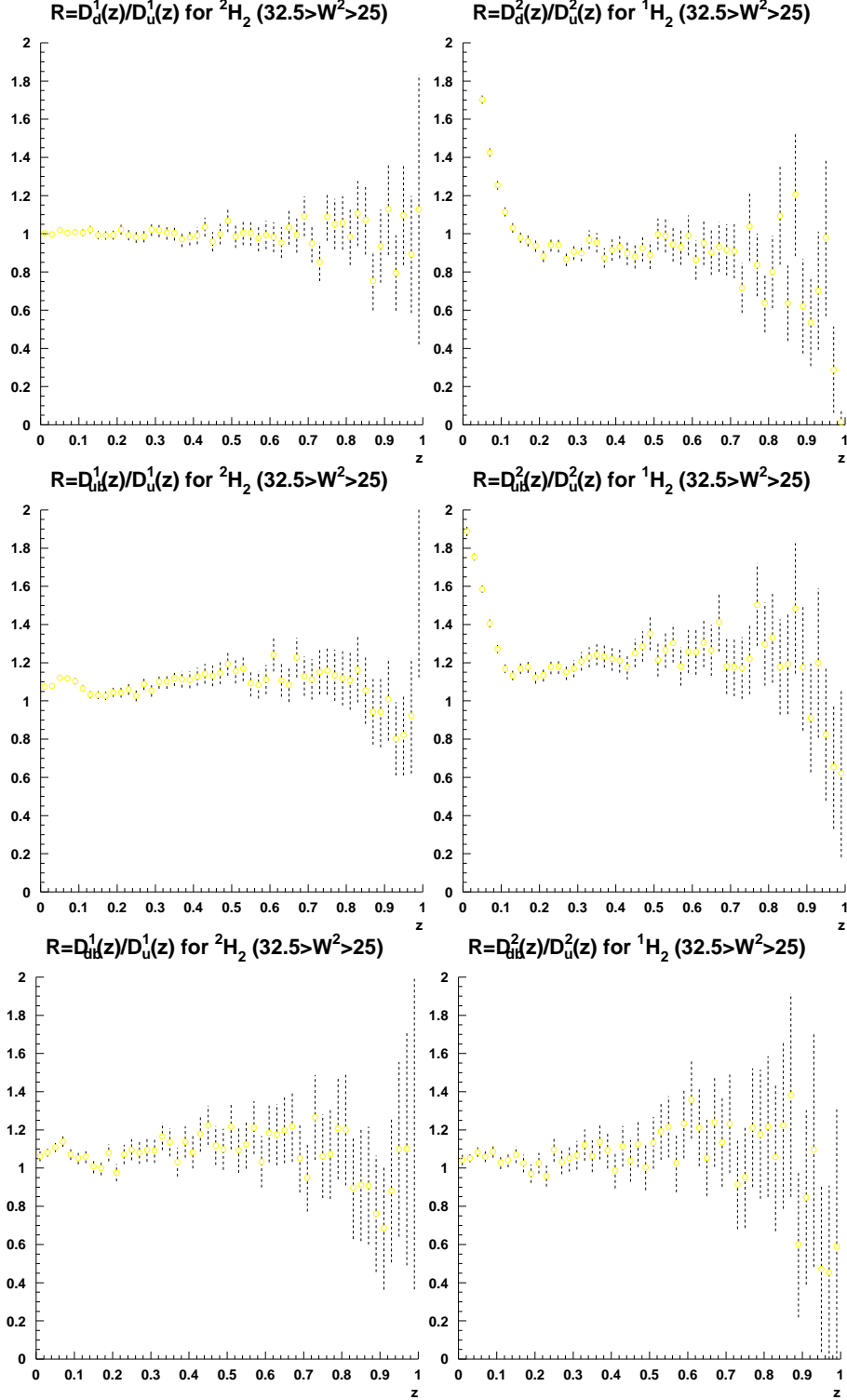
Figure 13: Ratios of charged pion dis-favored fragmentation functions for a Deuterium target (left column) and Hydrogen target (right column) for light quarks with $W^2 > 10$.

Figure 14: Ratios of charged pion dis-favored fragmentation functions for a Deuterium target (left column) and Hydrogen target (right column) for light quarks with $10 > W^2 > 4$.

Figure 15: Ratios of charged pion dis-favored fragmentation functions for a Deuterium target (left column) and Hydrogen target (right column) for light quarks with $25 > W^2 > 17.5$.

121

Figure 16: Ratios of charged pion dis-favored fragmentation functions for a Deuterium target (left column) and Hydrogen target (right column) for light quarks with $32.5 > W^2 > 25$.
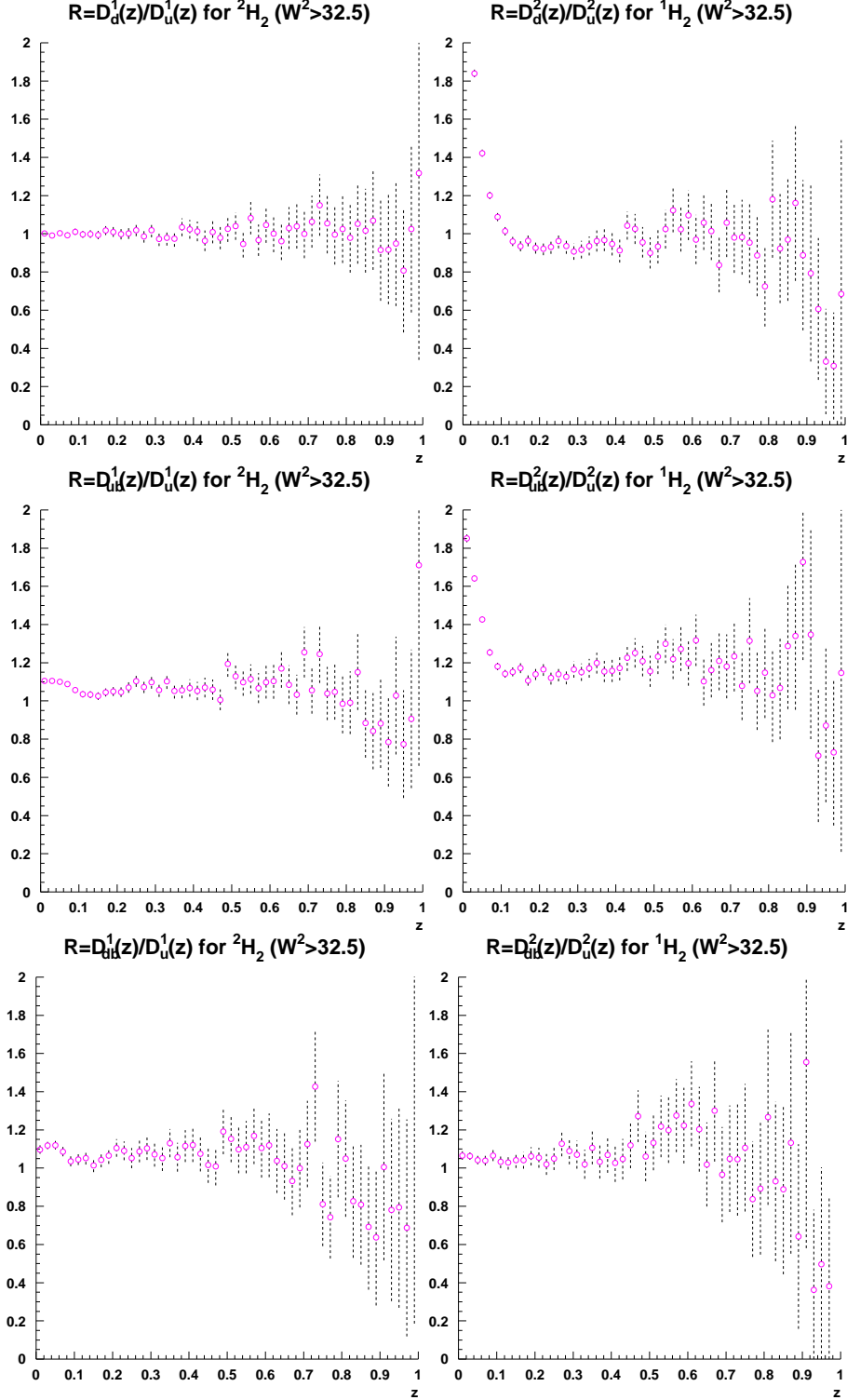
122

Figure 17: Ratios of charged pion dis-favored fragmentation functions for a Deuterium target (left column) and Hydrogen target (right column) for light quarks with $W^2 > 32.5$.
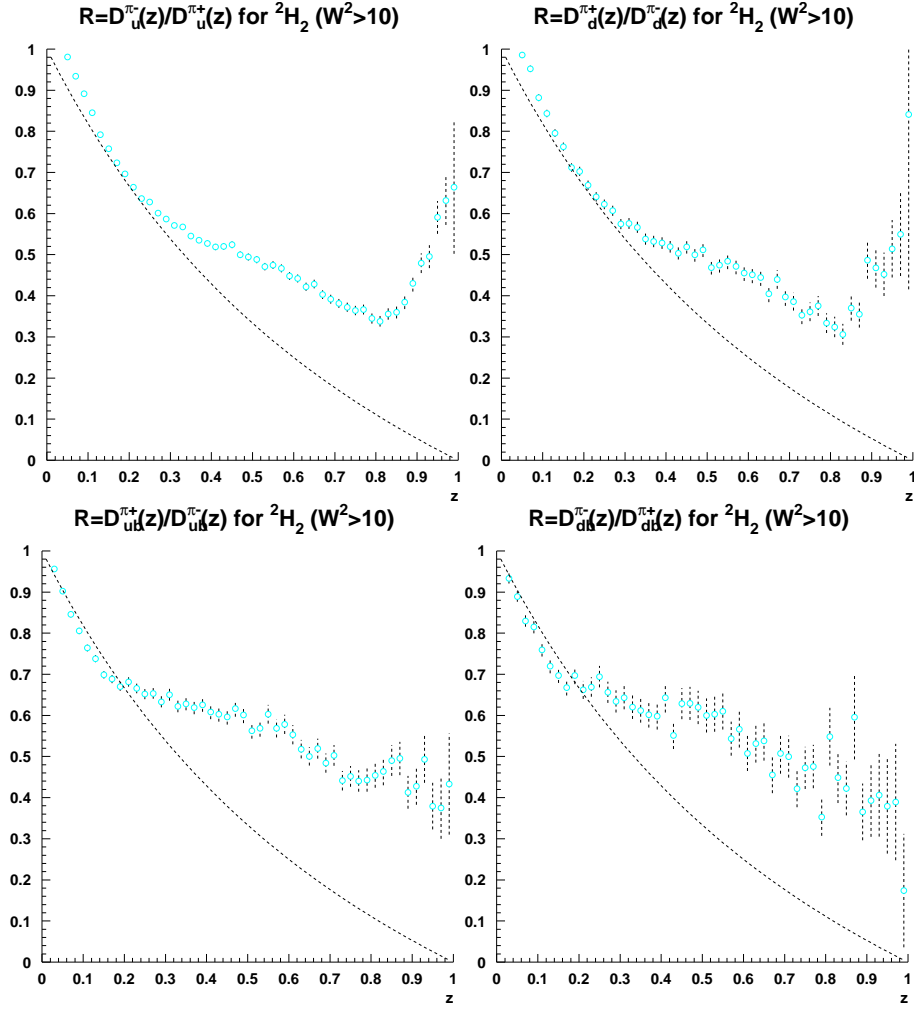
Figure 18: Ratios of favored to dis-favored fragmentation functions from a Deuterium target compared to the ansatz $(1-z)/(1+z)$ (dashed line) with $W^2 > 10$.
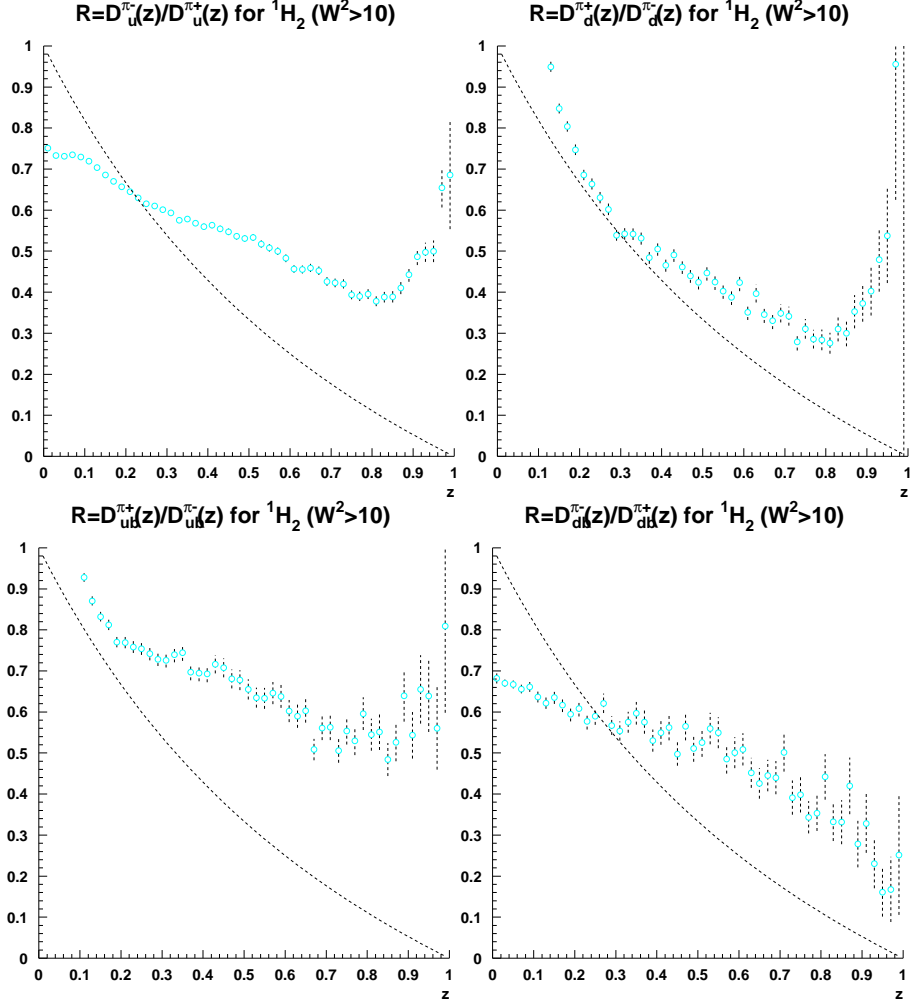
Figure 19: Ratios of favored to dis-favored fragmentation functions from a Hydrogen target compared to the ansatz $(1-z)/(1+z)$ (dashed line) with $W^2 > 10$.
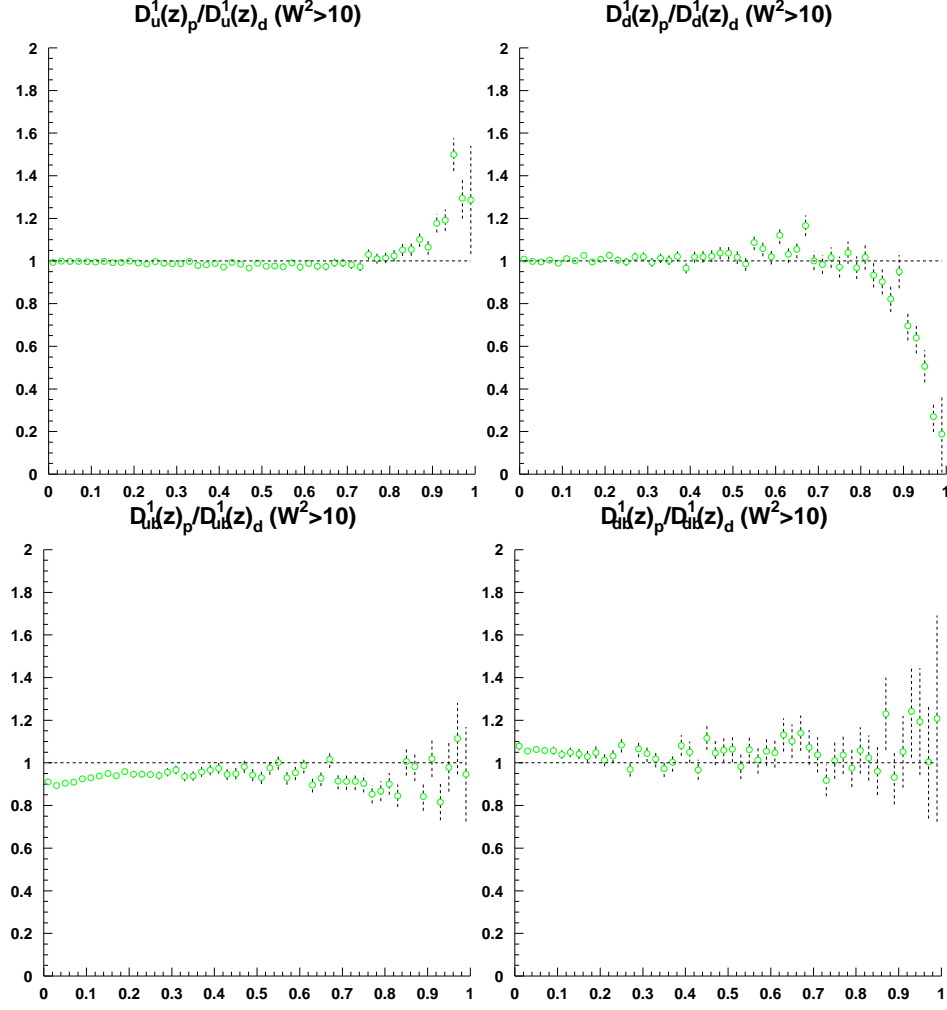
Figure 20: Ratios of the favored fragmentation functions for light quarks from a Hydrogen target to that of a Deuterium target with $W^2 > 10$.
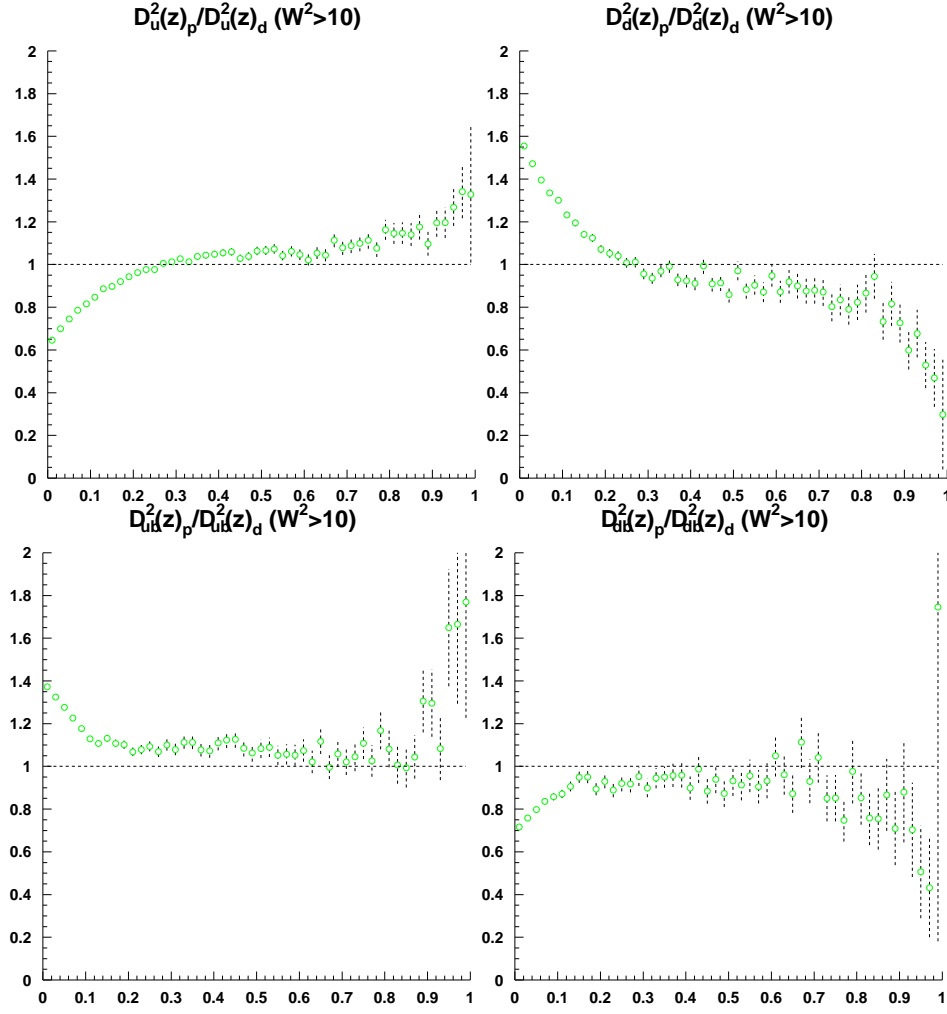
Figure 21: Ratios of the dis-favored fragmentation functions for light quarks from a Hydrogen target to that of a Deuterium target with $W^2 > 10$.
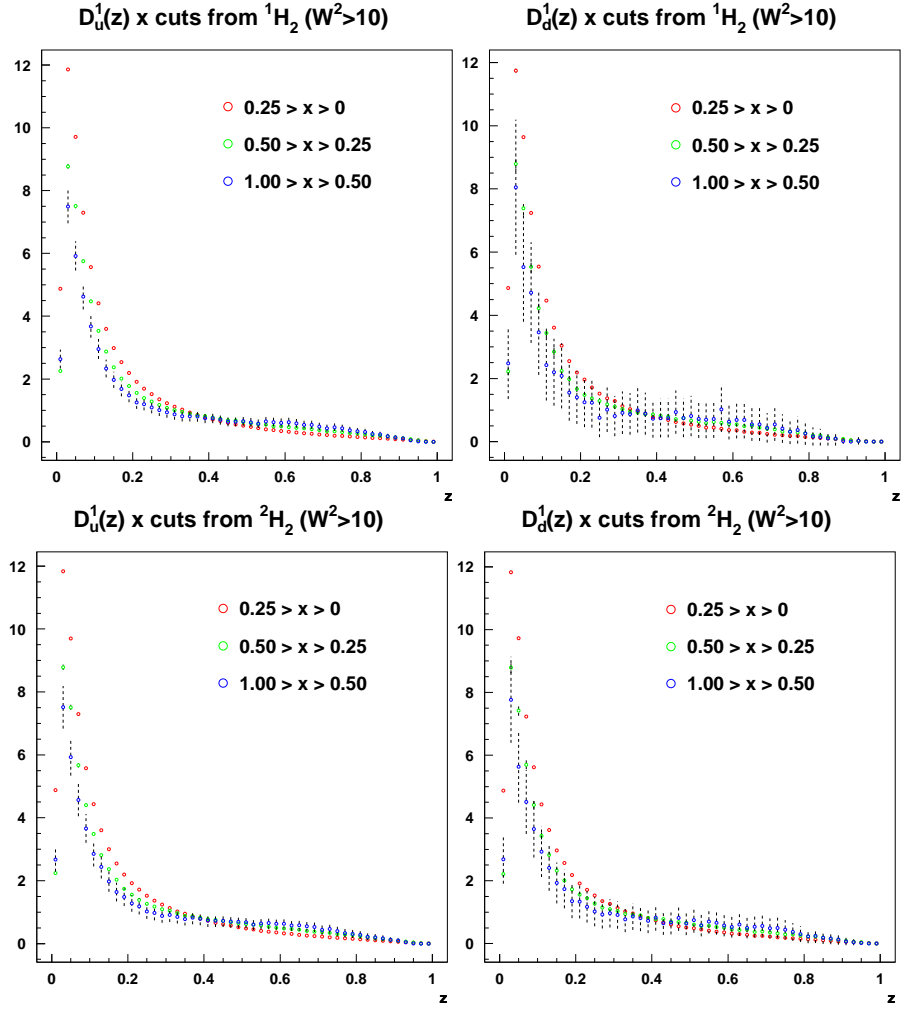
Figure 22: x dependence of favored fragmentation functions from a Hydrogen target (top) and Deuterium target (bottom) for valence quarks with $W^2 > 10$.
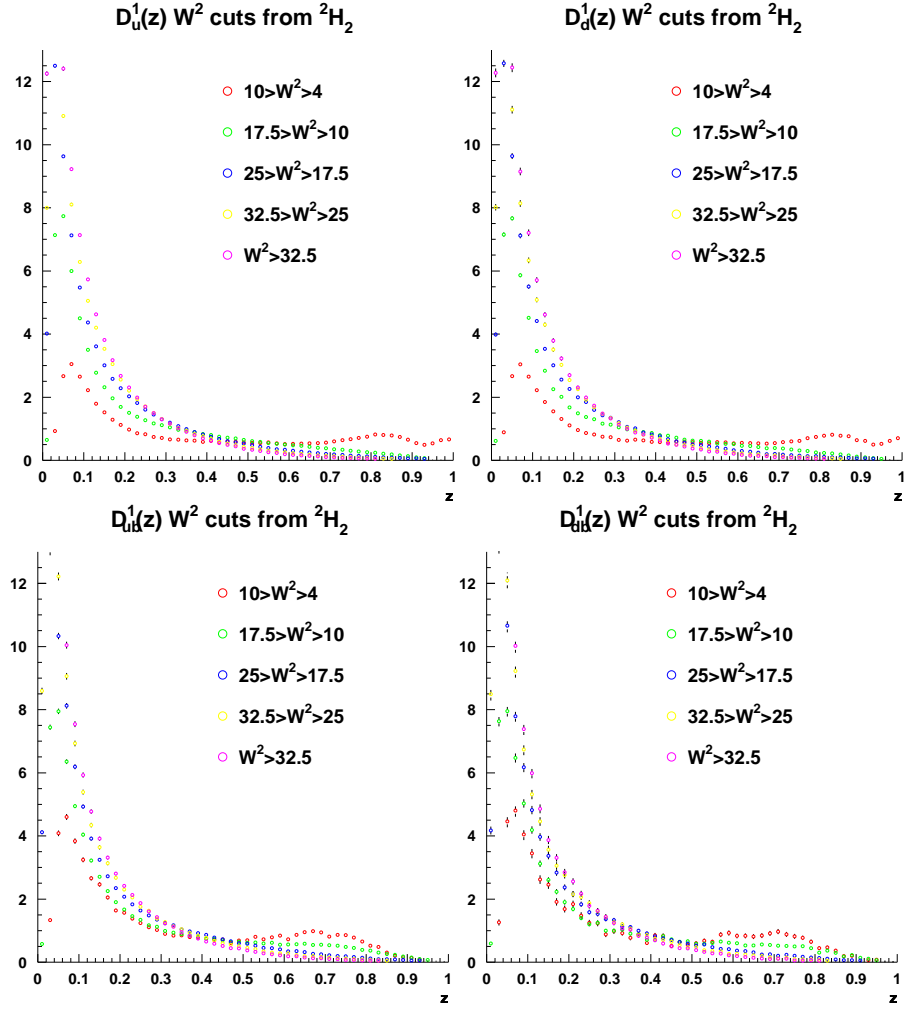
Figure 23: W^2 dependence of favored fragmentation functions for light quarks from a Deuterium target.
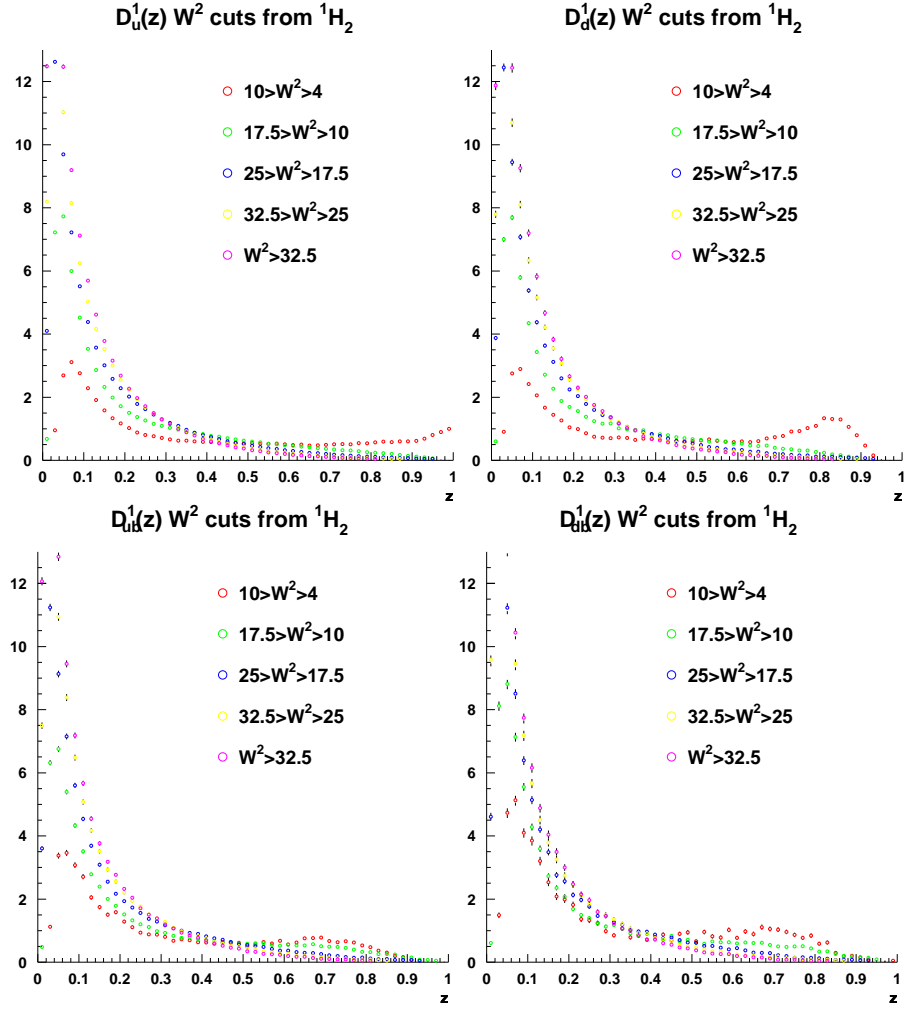
Figure 24: W^2 dependence of favored fragmentation functions for light quarks from a Hydrogen target.
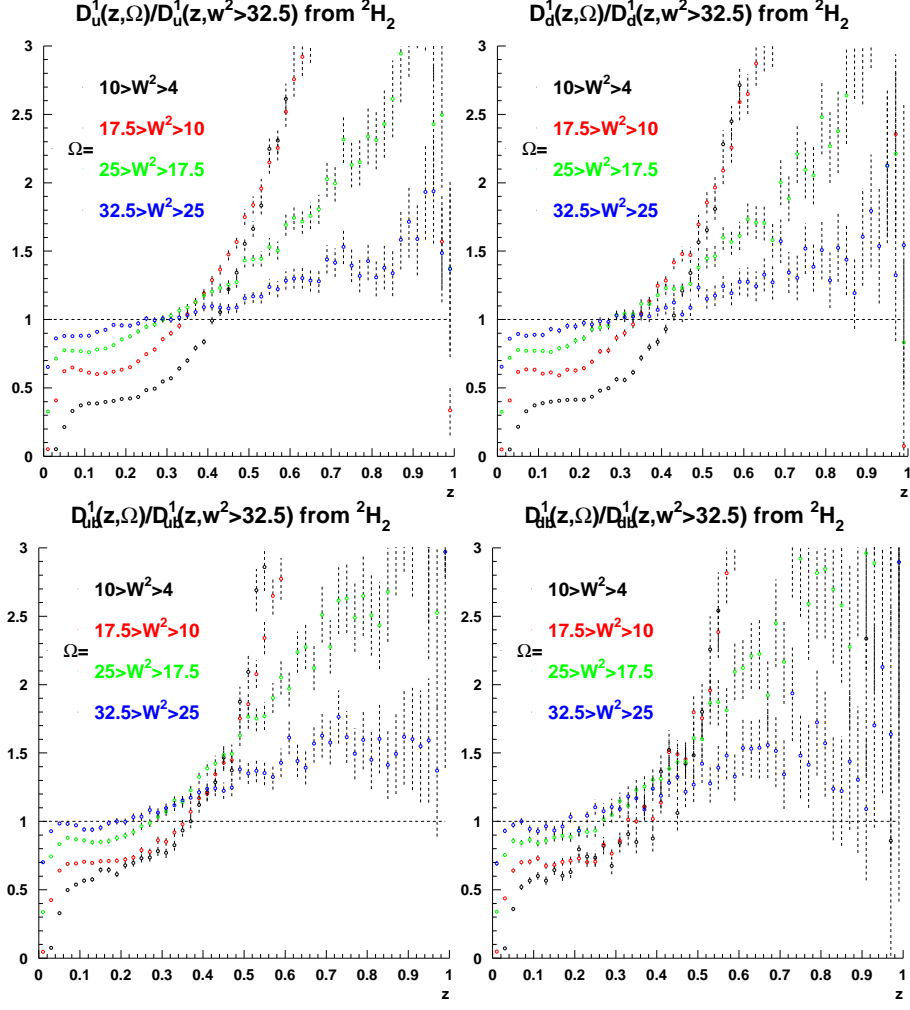
Figure 25: Ratio of favored fragmentation functions for light quarks from a Deuterium target in different W^2 regimes.
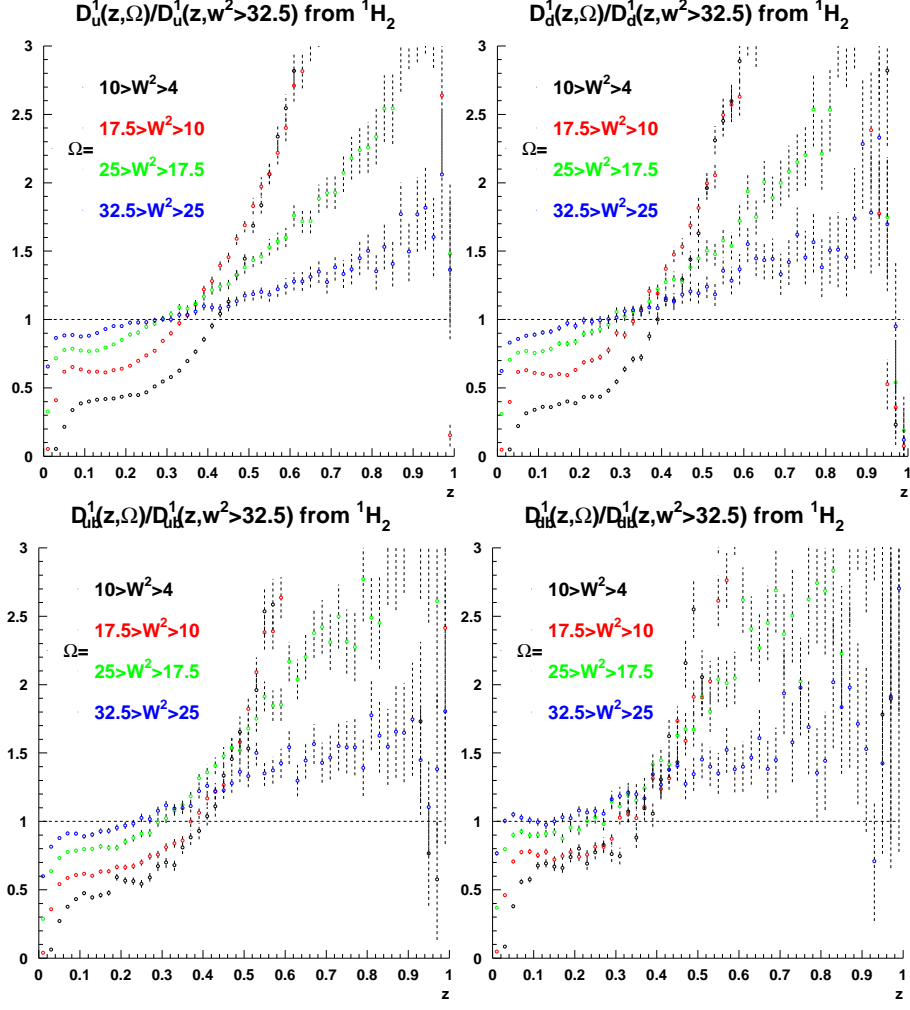
Figure 26: Ratio of favored fragmentation functions for light quarks from a Hydrogen target in different W^2 regimes.

References

[1] S. Eidelman et al., Physics Letters B **592**, 1+ (2004).

[2] A. D. Martin, W. J. Stirling, R. S. Thorne, and G. Watt, Phys. Lett. **B652**, 292 (2007).

[3] B. A. Kniehl, G. Kramer, and B. Potter, Nucl. Phys. **B582**, 514 (2000).

[4] S. Kretzer, Phys. Rev. **D62**, 054001 (2000).

[5] D. de Florian, R. Sassot, and M. Stratmann, Phys. Rev. **D75**, 114010 (2007).

[6] K. Ackerstaff et al., Phys. Rev. Lett. **81**, 5519 (1998).

[7] R. S. Towell et al., Phys. Rev. **D64**, 052002 (2001).

[8] J. Pumplin et al., JHEP **07**, 012 (2002).

[9] M. Gluck, E. Reya, and A. Vogt, Eur. Phys. J. **C5**, 461 (1998).

[10] L. I. Ponomarev, The Quantum Dice, CRC Press, New York, 1993.

[11] D. Teresi, Lost Discoveries: The Ancient Roots of Modern Science, Simon & Schuster, New York, 2003.

[12] M. Gordin, A Well-Ordered Thing: Dmitrii Mendeleev and the Shadow of the Periodic Table, Basic Books, New York, 2004.

[13] D. J. Griffiths, Introduction to Elementary Particle Physics, John Wiley and Sons, New York, 1987.

[14] C. S. Bogdon Povh, Klaus Rith and F. Zetsche, Particles and Nuclei, Springer, New York, 1999.

[15] J. Cork, Radioactivity and Nuclear Physics, D. Van Nostrand Company, New Jersey, 1957.

[16] J. D. Bjorken, Phys. Rev. **179**, 1547 (1969).

[17] G. T. Garvey and J.-C. Peng, Prog. Part. Nucl. Phys. **47**, 203 (2001).

[18] M. Breidenbach et al., Phys. Rev. Lett. **23**, 935 (1969).

[19] R. P. Feynman, Photon-Hadron Interactions, Benjamin, New York, 1972.

[20] E. G. John F. Donoghue and B. R. Holstein, <u>Dyamics of the standard Model</u>, Cambridge University Press, New York, 1992.

[21] P. Schmueser, Nucl. Instrum. Meth. **A235**, 201 (1985).

[22] R. N. Mohapatra and A. Y. Smirnov, Ann. Rev. Nucl. Part. Sci. **56**, 569 (2006).

[23] R. P. Feynman, Phys. Rev. **84**, 108 (1951).

[24] D. Chakraborty, J. Konigsberg, and D. L. Rainwater, Ann. Rev. Nucl. Part. Sci. **53**, 301 (2003).

[25] S. Leone, Electroweak and Top Physics at the Tevatron and Indirect Higgs Limits, in <u>Proceedings of 15th International Conference on Supersymmetry and the Unification of Fundamental Interactions (SUSY07)</u>, 2007.

[26] Y. Sumino, Phys. Lett. **B571**, 173 (2003).

[27] M. Kaku, <u>Quantum Field Theory A Modern Introduction</u>, Oxford Unversity Press, New York, 1993.

[28] F. Halzen and A. D. Martin, <u>Quarks and Leptons: An Introductory Course in Modern Particle Physics</u>, John Wiley and Sons, New York, 1984.

[29] P. A. M. Dirac, Proc. Roy. Soc. Lond. **A114**, 243 (1927).

[30] E. Fermi, Prog. Theor. Phys. **5**, 570 (1950).

[31] J. Callan, Curtis G. and D. J. Gross, Phys. Rev. Lett. **22**, 156 (1969).

[32] G. Altarelli and G. Parisi, Nucl. Phys. **B126**, 298 (1977).

[33] S. Albino, B. A. Kniehl, and G. Kramer, Nucl. Phys. **B725**, 181 (2005).

[34] S. Albino, B. A. Kniehl, G. Kramer, and C. Sandoval, Phys. Rev. **D75**, 034018 (2007).

[35] R. J. Fries, B. Muller, C. Nonaka, and S. A. Bass, Phys. Rev. **C68**, 044902 (2003).

[36] D. Amati and G. Veneziano, Phys. Lett. **B83**, 87 (1979).

[37] G. I. B. Andersson, G. Gustafson and T. Sjostrand, Physics Reports **97**, 31 (1983).

[38] T. Sjostrand, Comput. Phys. Commun. **82**, 74 (1994).

[39] A. Baldit et al., Phys. Lett. **B332**, 244 (1994).

[40] X.-d. Ji, J.-p. Ma, and F. Yuan, Phys. Rev. **D71**, 034005 (2005).

[41] P.-y. Chen, A. Idilbi, and X.-d. Ji, Nucl. Phys. **B763**, 183 (2007).

[42] P. Amaudruz et al., Nucl. Phys. **B371**, 3 (1992).

[43] S. Kumano, Phys. Rept. **303**, 183 (1998).

[44] M. Gluck and E. Reya, Mod. Phys. Lett. **A15**, 883 (2000).

[45] B.-Q. Ma, Phys. Lett. **B274**, 111 (1992).

[46] F. Huang, R.-G. Xu, and B.-Q. Ma, Phys. Lett. **B602**, 67 (2004).

[47] M. Wakamatsu, Phys. Rev. **D67**, 034005 (2003).

[48] Y. Ding, R.-G. Xu, and B.-Q. Ma, Phys. Rev. **D71**, 094014 (2005).

[49] W. Schroers et al., Nucl. Phys. Proc. Suppl. **106**, 1082 (2002).

[50] F. Farchioni, C. Gebert, I. Montvay, and W. Schroers, Nucl. Phys. Proc. Suppl. **106**, 215 (2002).

[51] C. T. H. Davies et al., Phys. Rev. Lett. **92**, 022001 (2004).

[52] K. Ackerstaff et al., Nucl. Instrum. Meth. **A417**, 230 (1998).

[53] A. A. Sokolov and I. M. Ternov, Phys. Dokl. **8**, 1203 (1964).

[54] J. Wendland, Polarized Parton Distributions Measured at the HERMES Experiment, PhD thesis, Simon Fraser University, 1999, DESY-HERMES-99-016.

[55] D. P. Barber et al., Phys. Lett. **B343**, 436 (1995).

[56] J. Buon and K. Steffen, Nucl. Instr. Meth. **A245**, 248 (1986).

[57] H. Grote and I. McLaren, Epio, CERN Program Library entry I101.

[58] S. Fisher and P. Palazzi, Adamo – entityrelationship programming system, 1993, CERN Program Library entry I101.

[59] W. Wander, Rekonstruktion hochenergetischer Streuereignisse im HERMES, PhD thesis, FriedrichAlexanderUniversitat ErlangenNurnberg, 1996.

[60] W. Wander et al., Prepared for International Conference on Computing in High- energy Physics (CHEP 95), Rio de Janeiro, Brazil, 18-22 Sep 1995.

[61] M. Funk, A Measurement of the Polarised Parton Densities of the Nucleon in DeepInelastic Scattering at HERMES, PhD thesis, Universitat Hamburg, 1998.

[62] A. Airapetian et al., Nucl. Instrum. Meth. **A540**, 68 (2005).

[63] A. Golendukhin, Prepared for 12th International Symposium on High-energy Spin Physics (SPIN 96), Amsterdam, Netherlands, 10-14 Sep 1996.

[64] E. Steffens, The HERMES polarized H and D gas target: 10 years of operation, volume 915, pages 955–960, 2007.

[65] K. Halbach, Nucl. Instr. Meth. **169**, 1 (1980).

[66] M. Beckmann, Extraction of Polarised Quark Distributions of the Nucleon from Deep Onelastic Scattering at the HERMES Experiment, PhD thesis, Freiburg University, 2000.

[67] H. T. Group, Unpolarized gas feed system - (ugfs) shift crew - operations manual, http://www-hermes.desy.de/expguide/UGFS-manual2006.ps.gz, 2006.

[68] M. Dell'Orso and L. Ristori, Nucl. Instrum. Meth. **A287**, 436 (1990).

[69] M. Dell'Orso and L. Ristori, In *Trieste 1988, Proceedings, The impact of digital microelectronics and microprocessors on particle physics* 239-246.

[70] J. Wendland, Particle identification for hermes run i, DESY-HERMES-01-067, 2001.

[71] G. Roeper, Messung der Feldverteilung des HERMES-Spektrometer-Magneten, PhD thesis, Institut fuer Experimentalphysik der Universitaet Hamburg, 1995.

[72] D. M. Thiessen, The Gas System for the HERMES Transition Radiation Detector, PhD thesis, Simon Fraser University, 1996, DESY-HERMES-96-028.

[73] H. Avakian et al., Nucl. Instrum. Meth. **A417**, 69 (1998).

[74] W. R. Leo, Techniques for Nuclear and Particle Physics, Springer-Verlag, Berlin Heidelberg, 1987.

[75] J. D. Jackson, Classical Electrodynamics, John Wiley and Sons, Inc., New York, 1962.

[76] N. Akopov et al., Nucl. Instrum. Meth. **A479**, 511 (2002).

[77] R. Kaiser, Likelihood analysis for the rich irt method, DESY-HERMES-00-026, 2000.

[78] D. Schepper and R. Kaiser, Particle identification with the hermes rich detector: Description of the different approaches, DESY-HERMES-98-008, 1998.

[79] W. Augustyniak et al., Tmc - vertex reconstruction in the presence of the hermes transverse target magnet, DESY-HERMES-07-008, 2007.

[80] T. Sjostrand, S. Mrenna, and P. Skands, JHEP **05**, 026 (2006).

[81] G. Ingelman, A. Edin, and J. Rathsman, Comput. Phys. Commun. **101**, 108 (1997).

[82] A. Hillenbrand, Measurement and Simulation of the Fragmentation Process at HERMES, PhD thesis, FRIEDRICH-ALEXANDER-Universitaet Erlangen, 2005, DESY-HERMES-05-036.

[83] I. Akushevich, H. Bottcher, and D. Ryckbosch, (1998).

[84] A. Miller, Applying radiative corrections to ratios of cross sections for deeply inelastic scattering, 2002.

[85] J. Pumplin, A. Belyaev, J. Huston, D. Stump, and W. K. Tung, JHEP **02**, 032 (2006).

[86] D. Mason, Prepared for 14th International Workshop on Deep Inelastic Scattering (DIS 2006), Tsukuba, Japan, 20-24 Apr 2006.

[87] L. Mankiewicz, A. Schafer, and M. Veltri, Comput. Phys. Commun. **71**, 305 (1992).

[88] A. Airapetian et al., Phys. Rev. **D71**, 012003 (2005).

Curriculum Vitae

Loren Alexander Linden Levy
Born December 02, 1978, Omaha, NE

Personal Information

Address:	135 Marshall Place Longmont, CO 80501-5646
Tel.:	(303) 332-2768
E-Mail:	alex@lindenlevy.com

Professional Information

Address:	390 UCB University of Colorado Boulder, CO 80309-0390
Tel.:	(303) 735-6146
E-Mail:	lindenle@colorado.edu

Education

2007 — Ph.D. Physics to be completed Dec. 2007 **University of Illinois Urbana-Champaign**

Thesis: *Unpolarized Nucleon Structure from the HERMES experiment*
Advisor: Naomi C. R. Makins

2002 — M.S. Physics **University of Illinois Urbana-Champaign**

2001 — B.S. Physics *summa cum laude* **Oregon State University**

Thesis: *The influence of the crystal potential on the de Has-van Alphen effect*
Advisor: Allen L. Wasserman

Current Positions

July 2007-Present Research Associate **University of Colorado Boulder**

Working on extracting the J/ψ suppression factor (R_{AA}) and elliptic flow coefficient (v_2) from run 7 high statistics Au+Au 200GeV data set. Performing performance studies for the resistive plate counter (RPC) forward upgrade at PHENIX. Additional day to day work with graduate students concerning individual research projects in hadron-jet correlations as well as studies that attempt to quantify the degrees of freedom in the quark gluon plasma (QGP).

Supervisor: James L. Nagle

July 2007-Present Member **PHENIX Collaboration**

Assisting with run 7 data reconstruction chain at CCIN2P3. Preforming DAQ data control modules checkout for the start of run 8 data taking at RHIC. Will sit shifts during run 8.

2001-Present   Member **HERMES Collaboration**

Responsibilities include taking shifts (prior to HERA shutdown) to monitor the performance and quality of data recorded by the HERMES spectrometer as well as debugging and correcting the polarized portion of the HERMES monte-carlo simulation code.

Work Experience

2001-July 2007   Graduate Research Assistant **University of Illinois Urbana-Champaign**

Performed an LO parton model extraction of the valence parton structure and light sea asymmetry within the nucleon from all available HERMES data. Contributed significantly to systematic studies of the polarized parton distribution errors arising from the purity method.

2003-July 2007   Linux Administrator **University of Illinois Urbana-Champaign Nuclear Physics Laboratory**

Responsibilities include CVS administration, LAMP web development and administration in addition to daily Linux user support. Experienced with MYSQL, Perl, C, C++, svn, bash, php and UNIX working environments.

PI: David Hertzog.

Fall 2001-Spring 2002   Graduate Teaching Assistant **University of Illinois Urbana-Champaign**

Responsible for four introductory level physics discussion sections. Material covered included Electro-Magnetism, Analog Electronics, and Geometric Optics (UIUC - PHYCS112).

Fall 2000-Spring 2001   Teaching Assistant **Oregon State University**

Responsible for six (three per quarter) introductory level physics discussion sections. Material covered included Newtonian Mechanics, Lagrangian Mechanics (OSU - PH211 winter quarter) and Electro-Magnetism with Geometric Optics (OSU - PH212 spring quarter).

Fall 2000-Spring 2001   Athletic Department, Head Math and Physics Tutor, **Oregon State University**

Organized math labs and coordinated private tutoring sessions. Tutored a wide range of college level mathematics, engineering and physics. Responsibilities included student attendance tracking, recruiting and training new tutors. Re-

sponsibilities increased to encompass interviewing and hiring new tutors.

Selected Publications

Conference Proceedings

L. A. Linden Levy, Isoscalar Extraction of Delta-s in the Nucleon at HERMES from Semi-Inclusive DIS, in *FUNDAMENTAL INTERACTIONS Proceedings of the 21st Lake Louise Winter Institute*, edited by A. Astbury and R. Moore, February 2006, http://www.worldscibooks.com/physics/6296.html.

L. A. Linden-Levy and D. M. Webber, Eschew the Queue: Administering a Small but Flexible Linux Cluster, in *Proceedings of NSF Cluster Computing Infrastructure Experience Workshop*, Department of Computer Science UIUC, 2005, http://www.cs.uiuc.edu/events/expwork-2005/proceedings.php.

L. A. Linden-Levy, Flavor decomposition of the nucleon's spin at HERMES, in *Frascati 2004, DAPHNE 2004*, pages 433–438, 2004, DESY-HERMES-04-45.

HERMES Publications

A. Airapetian et al., Precise determination of the spin structure function g1 of the proton, deuteron, and neutron, Phys. Rev. **D75**, 012007 (2007).

A. Airapetian et al., Single-spin asymmetries in semi-inclusive deep-inelastic scattering on a transversely polarized hydrogen target, Phys. Rev. Lett. **94**, 012002 (2005).

A. Airapetian et al., Quark helicity distributions in the nucleon for up, down, and strange quarks from semi-inclusive deep-inelastic scattering, Phys. Rev. **D71**, 012003 (2005).

Honors and Awards

Spring 2008   Recipient of **UIUC Physics Felix T. Adler Fellowship**

Spring 2002   Recipient of **UIUC Physics Excellence in Teaching Award**

Fall 2001   Recipient of **UIUC Physics Excellence in Teaching Award**

June 2000   Inducted to $\Sigma\Pi\Sigma$, **National Physics Honor Society**

May 2000   Recipient of **OSU College of Science Paul Copson Memorial Scholarship**

June 1998   Recipient of **COCC Scholastic Achievement Award**

May 3, 2008